

**CONTROL AND MANIPULATION OF SINGLE ATOMS
FOR INTERFACING WITH LIGHT**

by

CHOW CHANG HOONG

(M.Sc., National University of Singapore)

**A THESIS SUBMITTED FOR THE DEGREE OF
DOCTOR OF PHILOSOPHY**

**CENTRE FOR QUANTUM TECHNOLOGIES
NATIONAL UNIVERSITY OF SINGAPORE**

2023

Thesis advisor:

Professor Christian Kurtsiefer

Examiners:

Associate Professor Dzmitry Matsukevich

Assistant Professor Steven Touzard

Professor Philipp Treutlein, University of Basel

Declaration

I hereby declare that this thesis is my original work and it has been written by me in its entirety. I have duly acknowledged all the sources of information which have been used in the thesis.

This thesis has also not been submitted for any degree in any university previously.



Chow Chang Hoong

23 December 2023

Acknowledgments

I find that embarking on a Ph.D. journey is much like setting out on an epic adventure into a realm filled with challenges, quests, and formidable monsters to finally achieve the ultimate triumph. Particularly, I am truly grateful to a roster of individuals, by no means exhaustive, who have played an instrumental role in supporting me throughout this expedition.

First, I would like to express my deepest gratitude to my supervisor, Christian for his invaluable guidance, the freedom he granted me to explore diverse topics, and his support during pivotal moments of my research journey. His openness to new ideas and his no-nonsense approach to deconstructing complex physics problems have been a deep well of inspiration for me.

I am deeply thankful to Boon Long, not just a shareholder of the fruit of this thesis but also a knowledgeable collaborator and a trusted lab partner. His rigor keeps me grounded when I venture into uncharted territories, and his encouragement and support have been essential in achieving many significant milestones. I vividly recall those days during the first two years of graduate school when we would work until midnight, after the bus service had stopped. During our walk back to the hostel, we then discussed (mostly impractical) experiment ideas. Those days were really fun!

I also would like to thank my mentors, Wilson and Matthias (Steiner), who are also the predecessors of this experiment, for equipping me with the necessary skill sets in experimental optics. Their construction of the main part of the experimental setup and their provision of data processing tools have been extremely helpful and remain highly relevant.

Heartfelt appreciation to my fellow lab mates, including Xi Jie, Adrian, Lijiong, Vindhiya, Wai Marn, Kian Ming, and Zifang, with whom I have had the pleasure of working throughout this journey. I have learned a great deal from each of you, and I hope I have been an easy colleague to work with.

Cheers to all the friendly people co-living in 01-04, including Chi Huan, Janet, Ting You, Kelly, Neville, Florentin, Wen Xin/Winston, Eva, Philip, and Kenneth, for the camaraderie, countless coffees, and free buffet invitations. I also would like to thank all the workshop staff for their incredible support whenever I encountered

challenges while trying to troubleshoot something in the workshop.

Special thanks to Brenda, Victor, Mathias (Seidler), Alessandro, Jianwei, Hou Shun, Yicheng, Peng Kian, Jaesuk, Yifan, Ilija, Justin, Darren, and Thormund for generously sharing their expertise and providing assistance in the research. To all remaining members of the Quantum Optics group, your presence and engaging discussions have been invaluable in enriching our pool of physics ideas.

Last but not least, I would like to extend my appreciation to my family and friends for their unwavering support throughout my journey in pursuing and completing this project. Thanks to Jia Yi for her dedication in comprehending my work and sharing moments of joy.

To the reader, I hope this piece of writing is not too dull, and proves to be helpful in some manner!

Contents

Acknowledgments	i
Abstract	vi
List of Figures	vii
List of Tables	xi
1 Introduction	1
2 Experimental Setup and Techniques	9
2.1 Lenses in vacuum	9
2.2 Magneto-optical trap	10
2.3 Far-off resonant optical dipole trap	11
2.3.1 Theory	13
2.3.2 Implementation	16
2.3.3 Loading an atom into dipole trap	21
2.3.4 Atom lifetime	21
2.3.5 Dipole trap as a harmonic trap	22
2.4 Polarization gradient cooling	24
2.4.1 Temperature characterization	25
2.5 Ground state manipulation	27
2.5.1 Hyperfine state detection	27
2.5.2 State initialization by optical pumping	28
2.6 Transmission measurement	31
2.6.1 Absorption imaging of single atom	33

3	Resonance fluorescence	36
3.1	Theoretical background	36
3.2	Dressed-state representation	39
3.3	On-resonant excitation	41
3.3.1	Experimental implementation	41
3.3.2	Atom loss due to heating	43
3.3.3	Discussion	45
3.4	Off-resonant excitation	48
3.4.1	Correlation between two sideband photons	48
3.4.2	Correlation with single-sided filtering	54
3.5	Summary	55
4	Ground state coherence	56
4.1	Motivation	56
4.2	Rabi flopping	58
4.2.1	Implementation	60
4.3	Ramsey experiment	62
4.3.1	Implementation	62
4.3.2	Dephasing mechanisms	63
4.4	Spin echo	69
4.5	Dynamical decoupling	72
4.5.1	Periodic sequence	73
4.5.2	Uhrig sequence	79
4.5.3	Carr–Purcell sequence	82
4.5.4	Carr–Purcell–Meiboom–Gill sequence	83
4.6	Summary	84
5	Fano spectrum and cooling	85
5.1	Fano spectrum	85
5.1.1	Theoretical description	86
5.1.2	Implementation	88
5.2	EIT cooling	93
5.2.1	Theoretical model	93

5.2.2	Implementation	95
5.3	Summary	101
6	Array of two single atoms	102
6.1	From one to few atoms	102
6.1.1	Wavefront modulation	103
6.1.2	Implementation	104
6.1.3	Triggering of a pair of single atoms	107
6.1.4	Problems with small atomic spacing	109
6.2	Towards two-atom entanglement	113
6.2.1	Preliminary coalescence measurement	116
6.3	Summary	118
7	Conclusion and Outlook	120
	Bibliography	123
	Publications during Ph.D. Study	143

Abstract

Thesis title: Control and Manipulation of Single Atoms for Interfacing with Light

The realization of efficient coupling between light and atoms is indispensable for the construction of a distributed quantum network. To achieve this objective, we investigate a free-space atom-light interface based on a high numerical aperture lens. In our experimental setup, we employ a pair of aspheric lenses (NA=0.75) to tightly focus light onto optically trapped single ^{87}Rb atoms. The same aspheric lenses also facilitate efficient collection of atomic fluorescence, useful for exploring concepts in quantum optics.

Motivated by these capabilities, we first study the interaction between a coherent field and a two-level system in the saturation regime. The emergence of a Mollow triplet, which is a signature of optical nonlinearity, is observed in the single-atom fluorescence spectra for different power levels measured with an optical cavity. When the atom is illuminated with off-resonant light, further analysis through intensity correlation measurements $g^{(2)}$ also confirms a preferential temporal ordering between the emission of single photons originating from opposite fluorescence sidebands. Moreover, this thesis presents a series of experimental techniques aimed at preserving qubit coherence, minimizing atomic thermal motion, and scaling up the number of qubits. Here, quantum bits are encoded in the magnetically sensitive Zeeman states in atomic ground state hyperfine levels. Applying a Carr-Purcell-Meiboom-Gill dynamical decoupling sequence successfully extends the T_2 coherence time of a superposition state to about 7 ms from an initial inhomogeneous dephasing time of less than 100 μs . Additionally, a Fano resonance is observed in the excitation spectra of a single ^{87}Rb atom using a pump-probe configuration. We then demonstrate the cooling of atomic motion to less than 6 μK by exploiting the Fano interference effect. Finally, we show deterministic loading of single atoms into a pair of holographic dipole traps spaced approximately 3 μm apart. Subsequently, a two-photon interference measurement is performed with the cooling fluorescence emitted by two separated single atoms to illustrate the phenomenon of photon coalescence. The tools developed in this thesis pave the way for the implementation of practical quantum information protocols using a free-space atom-light quantum interface.

List of Figures

2.1	Schematic of the aspheric lens used in this work.	10
2.2	Imaging the focal plane of the high NA lens onto a camera placed along the optical axis.	12
2.3	Light shift of the $5S_{1/2} F = 2, m_F = 0\rangle$ ground state and the $5P_{3/2} F' = 3, m'_F = 0\rangle$ excited state as a function of dipole beam wavelength.	15
2.4	Optical setup for probing light-atom interaction in free space.	17
2.5	Cooling fluorescence of single atoms and its histogram.	18
2.6	Chromatic axial shift due to chromatic aberration in the aspheric lens as a function of wavelengths.	18
2.7	Flowchart illustrating a standard experimental sequence.	20
2.8	Lifetime of the atom in the optical dipole trap.	22
2.9	Parametric heating of a single atom to determine the trap frequencies.	24
2.10	Experimental sequence for “release-and-recapture” technique to characterize atomic temperature.	25
2.11	Release-and-recapture measurement to deduce atomic temperature.	26
2.12	Fluorescence histogram for the state detection process.	27
2.13	Optical pumping to prepare single atoms in the maximal Zeeman state.	29
2.14	Optical pumping measurements to confirm successful state preparation.	30
2.15	Experimental sequence for measuring transmission.	32
2.16	Transmission spectroscopy of a single atom for a weak coherent laser.	32
2.17	Absorption images of a single atom.	34
3.1	Calculated scattering rates and spectral densities of atomic fluorescence for various saturation parameters s	37
3.2	Dressed-state picture for an atom interacting with an intense driving field.	40

3.3	Optical setup for collecting atomic fluorescence from a single atom in free space.	41
3.4	Experimental sequence for probing the Mollow triplet.	42
3.5	Saturation curve of the atomic scatterings and transmission spectrum of the filter cavity.	42
3.6	Trapping profiles for different atomic levels and the associated survival probabilities.	45
3.7	Normalized resonance atomic emission spectra at different excitation intensities.	46
3.8	Second-order correlation function of the single atom at different excitation intensities.	49
3.9	Optical setup for collecting atomic fluorescence from a single atom in free space for $g^{(2)}$ measurements.	50
3.10	Normalized cross-correlation between photons from two opposite Mollow sidebands.	51
3.11	Two possible multiphoton scattering processes to explain the asymmetrical temporal correlation.	52
3.12	Dressed-state picture for an atom coupling to an off-resonant driving field.	53
3.13	Normalized cross-correlation between a photon projected to a Mollow sideband and an unfiltered photon.	54
4.1	Scheme to create atom-photon and photon-photon entanglement by driving the two-level system repetitively.	57
4.2	Schematic diagram for the generation of a microwave signal to drive the hyperfine transition.	59
4.3	Schematic for probing the coherence of the Zeeman qubit states.	60
4.4	Experimental sequence for driving a microwave transition between two ground state Zeeman levels.	61
4.5	Rabi oscillation measured between two Zeeman sublevels.	61
4.6	Experimental sequence for probing the coherence of the superposition state $ +\rangle = (\uparrow\rangle + i \downarrow\rangle)/\sqrt{2}$ using a Ramsey measurement.	63
4.7	Ramsey measurement between the two Zeeman sublevels.	64
4.8	Emergence of elliptical polarizations near the focus due to tight focusing.	68

4.9	Experimental sequence for probing the coherence of the superposition state $ +\rangle = (\uparrow\rangle + i \downarrow\rangle)/\sqrt{2}$ in a spin echo measurement.	70
4.10	Spin echo measurements for the atom prepared in the basis of stretched states or in the basis of clock states.	71
4.11	Schematic representation of the PDD and UDD sequences and the associated filter functions.	74
4.12	Coherence evolution under PDD for three and five π pulses.	75
4.13	Coherence time T_2 as a function of the number of π pulses.	76
4.14	Noise spectroscopy with DD adapted from atomic magnetometry.	78
4.15	Coherence evolution under UDD for three and five π pulses.	80
4.16	Optimization scheme with five π pulses for a fixed free evolution time.	81
4.17	Schematic representation of the CP and CPMG sequences, followed by the coherence time measurement.	83
5.1	A three-level Λ system interacting with a pair of coupling and probe fields.	86
5.2	Energy levels in ^{87}Rb and optical setup used for observing the Fano scattering profile.	88
5.3	Experimental sequence for measuring the Fano scattering profile.	90
5.4	Single photon scatterings recorded in the Fano spectroscopy.	91
5.5	Linear increase in the Fano linewidths as a function of probe intensities.	92
5.6	EIT cooling transition in a three-level Λ system.	94
5.7	Energy levels in ^{87}Rb and experimental configuration for the EIT cooling process.	95
5.8	Experimental sequence for performing EIT cooling on a single ^{87}Rb atom.	96
5.9	Atomic temperature after EIT cooling at various detunings.	98
5.10	Atomic temperature as a function of coupling light intensity and cooling duration.	99
6.1	Phase patterns employed on the spatial light modulator.	104
6.2	Optical setup for interfacing a pair of single atoms with light.	105
6.3	Distance between the pair of single atoms as a function of wavefront modulation period.	106
6.4	Two-dimensional fluorescence histogram to discriminate the two atoms.	108

6.5	Probability of detecting a single atom in either dipole trap after illumination with a resonant probe beam.	110
6.6	Calculated intensity profile around the focus for the SLM modulated FORT beam.	112
6.7	Scheme to generate two-atom entanglement by a single photon detection.	114
6.8	Optical setup to measure intensity correlation of single photon interference from two single atoms.	115
6.9	Experimental sequence for measuring the intensity correlation of single photon interference from two single atoms.	115
6.10	Second-order correlation function for the single photon interference from two single atoms.	117

List of Tables

1.1	State of the art of atom-light coupling in free space.	6
2.1	Coefficients for scalar, vector, and tensor decomposition of the AC Stark shift for a dipole light of 851 nm.	16

Chapter 1

Introduction

Regarded as one of the cornerstones of modern physics, quantum mechanics offers some of the most precise predictions about the microscopic behavior of nature. Although insights gained from quantum physics have contributed to the invention of many modern technologies, including lasers, semiconductor electronics, and magnetic resonance imaging [1], it was initially uncertain that one could possibly manipulate individual quantum particles to accomplish something useful, until Feynman proposed the idea of building a computer that could exactly simulate the quantum nature of reality [2]. Sparked by the rapid developments in techniques for experimenting with single atoms and single photons, this concept of harnessing quantum mechanics for information processing has subsequently led to the emergence of quantum information science.

Within this context, bit of information is encoded in a two-level quantum system, coined as a qubit. A qubit is no longer limited to only being in the logical states of 0 or 1, but can be in a coherent superposition of states 0 and 1. Moreover, multiple qubits can be entangled, for which the multi-qubit state can only be described as an inseparable whole. These counter-intuitive properties enable quantum information science to engineer novel technologies that can offer functionality beyond any classical device, most notably in the fields of computation, cryptography, metrology, and simulation.

Taking one of the most celebrated quantum algorithms as an example, Shor's algorithm can factor an integer into primes exponentially faster than the best classical algorithm [3]. While this may seem to suggest that the conventional public-key cryptography, like the widely used RSA scheme, is in serious trouble, only

factorization of small numbers has been realized in proof-of-principle experiments thus far (such as factoring 21 into 3×7 [4]). In fact, it has been estimated that for Shor’s algorithm to crack a typical 2048-bit RSA code reliably, no less than tens of millions of physical qubits are required [5]. Even for selected quantum sampling algorithms that are considered more feasible in the noisy-intermediate scale quantum (NISQ) computing stage [6], achieving “quantum supremacy” requires substantial hardware resources. For instance, quantum supremacy is only manifested in the recent pioneering experimental works with more than a hundred optical modes for Gaussian boson sampling [7–9], and at least fifty logical qubits for sampling the output of a pseudo-random quantum circuit [10, 11]. Overall, the scalability of physical qubits is essential for quantum computers to be practically useful.

Distributed Quantum Network

One of the proposals to scale up quantum systems envisions the construction of a distributed quantum network [12]. In this protocol, a stationary qubit forms a small-scale information processing unit and is manipulated locally at a node in the network. Subsequently, quantum information is transferred from one node to another at a distant location with a flying qubit. To date, a range of systems has been explored as potential stationary qubits, including quantum dots [13, 14], color centers in diamonds [15, 16], trapped ions [17, 18], neutral atoms [19], and superconducting circuits [20]. Much like in classical information processing, any quantum system used for quantum information processing must allow efficient state preparation, manipulation, and measurement with high fidelity.

For the flying qubit, the most natural candidate is a photon. This is because photons only interact weakly with the environment, and hence they can preserve coherent superposition states well over a long distance. In particular, photons at telecom wavelengths can propagate through optical fibers with low transmission loss (at 1550 nm) or low dispersion (at 1310 nm). Moreover, it represents an economical choice, considering the existence of a vast network of optical fibers deployed by the telecommunication industry. This pre-existing network infrastructure can significantly reduce the required outlay cost for photon transmission over long distances. Adding to the anticipation is the recent development in frequency converters that allow for an efficient down-conversion to telecom wavelength from a short-wavelength

single photon emitted from a quantum emitter while preserving the quantum information [21, 22]. Through careful engineering of wavelength conversions compatible with multiple species of quantum emitters, this technique enables the entanglement of qubits across heterogeneous platforms over long distances.

One landmark experiment for realizing the quantum network is the demonstration of atom-photon entanglement. Conventionally, two distinct techniques are employed for this purpose. The first approach relies on the spontaneous Raman scattering process to achieve continuous-variable entanglement between ensembles of atoms and light fields. Promising results have already been shown for atomic ensembles [23] and rare earth ions in solids [24].

For the second method, the emitter is initialized in a suitable excited state, so that a spontaneous emission process entangles the polarization of the emitted photon and the final electronic state of the quantum emitter. Previous studies in this direction encompass various systems including single neutral atoms [25–27], trapped ions [28], nitrogen-vacancy centers [29] and quantum dots [30]. In all these demonstrations, the entanglement distribution is restricted to tens of kilometers even after the implementation of frequency conversion into low-loss telecom wavelengths, due to decoherence in the atomic state [27]. Fortunately, the issue of atomic decoherence can be mitigated by incorporating quantum error correction protocols [31], decoherence-free subspaces [32, 33] or dynamical decoupling sequences [34–36] into the generation scheme.

Another major challenge for the quantum network lies in achieving efficient transfer of quantum information between a photonic qubit and an atomic qubit. One popular remedy is to place the quantum emitter within an optical resonator to enhance the strength of the light field. However, operating a cavity requires precise active stabilization of the cavity length to maintain a substantial atom-light coupling, restricting its potential for upward scalability. In the realm of nanophotonics, diverse waveguide structures are engineered to achieve tight confinement of light via an evanescent field [37–39]. Thanks to the recent advancement in nanofabrication technology, it is now possible to combine those two concepts of evanescent field and cavity, leading to the development of nanofiber cavities [40, 41] and whispering-gallery-mode microcavities [42, 43] to demonstrate near-deterministic coupling.

Interfacing Single Atoms in Free Space

Employing a cavity or a nanowaveguide will impose boundary conditions on the interface platform and can allow only a countable set of optical modes to interact with the atom, which is often undesirable for the study of continuum dynamics in quantum optics. One simple alternative approach involves tightly focusing light fields onto single atoms in free space. To maximize the amplitude of the electric field in the focus, the recipe is to transform the incident radiation into an atomic dipole mode. As such, the coupling efficiency Λ , given by the spatial mode overlap between the incident probe mode and the atomic dipole mode, can be used to quantify the interaction strength:

$$\Lambda = \frac{|\int E_d E_{in}^* d\Omega|^2}{\int |E_d|^2 d\Omega \int |E_{in}|^2 d\Omega}, \quad (1.1)$$

with E_d the atomic dipole mode, E_{in} the incident radiation mode, and $\int d\Omega$ the integral over the full solid angle. In particular, the physical bound for an incident light mode focused down by a lens is given by $\Lambda \leq 0.5$ [44].

Empirically, determining the coupling efficiency Λ is not straightforward. It requires inference from the optical response of the atom, such as reflection measurement. For that, the amplitude of backward scattered light collected in the input mode is measured in relation to the incident probe power. For a weak coherent input field, the backscattering light power depends only linearly on the probe power. As such, the reflection coefficient R , quantified as the ratio between the backscattering intensity and the probe intensity, is then stipulated by:

$$R(\Delta) = 4\Lambda^2 \frac{\Gamma^2}{\Gamma^2 + 4\Delta^2}, \quad (1.2)$$

with Γ the transition linewidth and Δ the laser detuning from atomic resonance. The maximum efficiency of retrieving a reflected single photon is then given by $4\Lambda^2$.

Another frequently employed measurement for assessing the interaction strength is transmission spectroscopy. The principle underlying this technique is that the light coherently scattered by the emitter undergoes destructive interference with the incident beam on the detector. This interference results in the attenuation of transmitted power, commonly referred to as extinction. For a weak input probe field, the single-mode transmission coefficient T can be represented as

$$T(\Delta) = \left| 1 - 2\Lambda \frac{i\Gamma}{i\Gamma + 2\Delta} \right|^2. \quad (1.3)$$

Besides the aforementioned measurements that emphasize light intensity, a strong interaction strength also implies a large phase shift imprinted by a single quantum system onto a coherent beam. This is particularly interesting due to its potential for realizing a photonic phase gate, in which the phase of a photon is altered based on the atom's presence or the internal state of the atom. It can be shown that the phase shift $\delta\phi$ has the form [45],

$$\delta\phi(\Delta) = \arg\left(1 - 2\Lambda\frac{i\Gamma}{i\Gamma + 2\Delta}\right). \quad (1.4)$$

The phase shift is maximum at half linewidth detuning.

It should be noted that the formulations for the measurements provided above remain applicable for a classical dipole as well. In the field of quantum optics, predictions suggest that a two-level emitter can instigate nonlinear interactions among photons. In particular, the saturable nature of a two-level emitter prevents the absorption of multiphoton components, leading to a modification of the photon statistics of the transmitted light. This is given by the second-order correlation function,

$$g^{(2)}(\tau = 0) = \frac{(1 - 4\Lambda)^2}{(1 - 2\Lambda)^4}. \quad (1.5)$$

Notably, for $\Lambda = 0.25$, the atom can function as a photon turnstile that converts a coherent field completely into a single-photon field [$g^{(2)}(\tau = 0) = 0$] [38, 46–48]. For $\Lambda > (2 - \sqrt{2})/2$, we will observe that the transmitted light displays a bunching behavior [$g^{(2)}(\tau = 0) > 1$]. This is because the one-photon Fock state is strongly suppressed by the scattering process, leaving behind the multiphoton components that saturate the atomic transition in the transmitted port [49].

Fundamentally, it is of interest to find the maximum achievable absorption probability by focusing light onto a single quantum system. Although the atom-light interaction in free space is typically weaker than in cavity QED systems, the free-space approach is more robust and much simpler to set up. For those reasons, explorations are being undertaken across a spectrum of focusing techniques, including multi-element objectives [50–56], aspherical singlets [48, 57], Fresnel lenses [58], metasurface lenses [59], and parabolic mirrors [60–62]. An overview of these works is outlined in Table 1.1.

Here, we choose to achieve an efficient atom-light coupling by tightly focusing light onto single atoms with an aspheric lens. Early experiments in our group employed

Experimental system	Year	Measurement	Λ
$^{198}\text{Hg}^+$ [63]	1987	Extinction of $\leq 0.1\%$	$\leq 0.025\%$
Quantum dot (microscope) [50]	2007	Extinction of 12%	3.1%
Dye molecule (microscope) [52]	2008	Extinction of 22%	5.8%
^{87}Rb (aspherics) [57]	2008	Extinction of 9.8%	2.51%
^{87}Rb (aspherics) [57]	2009	Phase shift of 0.97°	1.66%
Organic molecule (microscope) [53]	2011	Extinction of 19%	5%
		Phase shift of 3°	5%
$^{174}\text{Yb}^+$ (parabolic mirror) [60]	2014	Saturation at 692pW	1.8%
^{87}Rb (aspherics) [48]	2017	Extinction of 36.6%	10.2%
		$g^{(2)}(0) = 0.934$	10.2%
$^{174}\text{Yb}^+$ (parabolic mirror) [62]	2017	Phase shift of 2.2°	3.7%

Table 1.1: State of the art of atom-light coupling in free space.

an off-the-shelf molded glass aspheric lens with a numerical aperture (NA) of 0.55 and successfully demonstrated about 10% extinction [57] and 1° phase shift [45] of a weak coherent field. Subsequent work further investigated the excitation probability of a two-level atom depending on the temporal profile of the photons. For the second iteration under the same topic, a customized aspheric lens of $\text{NA} = 0.75$ is used for the demonstration of 20% extinction with single-sided illumination and nearly 40% extinction in a 4π configuration [48].

With the groundwork laid by previous efforts, we can now explore various schemes and control techniques that can be useful in developing building blocks for a distributed quantum network. First, the coherence of an atomic state is particularly important because it limits the duration during which quantum information can be maintained and transferred. Previously, we have examined the potential of suppressing atomic motion-induced qubit dephasing by employing a linearly polarized dipole trap [64]. With a high-fidelity coherent control of the ground state hyperfine manifold, we look into the implementation of various dynamical decoupling schemes. The construction of an optimal dynamical decoupling sequence also unveils the spectral characteristics of the underlying qubit dephasing mechanism.

Second, the generation of highly non-classical light fields is of paramount importance to quantum information processing, contributing to heightened communication security [65, 66] and enhanced measurement sensitivity [67, 68]. A single atom, the smallest unit for a quantum light source, is of fundamental interest. The efficient

fluorescence collection provided by our high numerical-aperture optics allows us to measure the power spectrum of the resonance fluorescence from a single quantum emitter, resolving the Mollow triplet spectrum [69]. Going one step further, we also experimentally investigated the intensity cross-correlation between the sidebands of the Mollow structure, motivated by the theoretical predictions pointing towards a time ordering feature among the sideband photons [70]. This scheme can be a novel approach for generating Fourier-limited photon pairs that might find applications interfacing with atoms or atom-like systems as stationary nodes in a distributed quantum network.

As the thermal motion of the trapped atom can severely impair the coherent coupling between atom and light [71], an efficient cooling technique is always desirable to bring down the atomic temperature. A ground-state laser cooling technique based on electromagnetically induced transparency (EIT) has recently been proposed as a robust solution that can cool several vibrational modes simultaneously through continuous excitation [72]. Using the Zeeman sublevels in the hyperfine structure, we demonstrate EIT cooling of an optically trapped single neutral atom.

There is also an attempt to increase the number of qubits in our experimental system. Using the conventional wavefront shaping technique, we holographically create two optical single-atom trapping sites in arbitrary geometries. We foresee potentially using this platform for the generation of collective atomic states, with a specific focus on exploring phenomena such as subradiance and superradiance [73].

Thesis Outline

The rest of this thesis is organized as follows:

In Chapter 2, we provide an overview of the fundamental aspects of the experimental setup and offer a brief summary of each key component of the apparatus. Particularly, the details of trapping, cooling, and manipulating single atoms are provided along with their respective calibration measurements.

Chapter 3 focuses on measuring the power spectrum of the atomic fluorescence utilizing a Fabry-Perot cavity. By elevating the intensity of the driving field into the saturation regime, the spectrum shows the emergence of the Mollow triplet phenomenon. With an off-resonant driving field, we confirm the presence of asymmetry

in the intensity correlations between photons originating from the two sidebands of the fluorescence spectrum.

Chapter 4 presents the realization of coherent control over the atomic ground state hyperfine levels using a microwave field. By initializing the system in a superposition state of the magnetic sublevels, we perform a Ramsey experiment to investigate the coherence of the qubit. We further show that a suitable dynamical decoupling sequence can suppress qubit dephasing significantly, extending the coherence time by two orders of magnitude.

In Chapter 5, the emphasis shifts to the demonstration of a ground-state cooling technique based on electromagnetically induced transparency (EIT). We resolve the signature Fano profiles in the fluorescence scattering spectrum as well as the temperature measurement. A final temperature of around $6 \mu\text{K}$ has been achieved with EIT cooling, a factor of two lower than the previous value obtained using the polarization gradient cooling technique.

Chapter 6 documents the experimental efforts to scale up the number of single-atom traps formed by the direct image of a spatial light modulator. We implement the control system for the deterministic loading of single atoms in two dipole trap sites. Moreover, the chapter delves into a discussion regarding limitations inherent in the geometrical arrangement of the setup. A two-photon interference measurement is performed on the cooling fluorescence scattered by a pair of single atoms.

Finally, we conclude the entire thesis as well as discuss further directions for future research in Chapter 7.

Chapter 2

Experimental Setup and Techniques

This chapter introduces the key components for trapping and manipulating single ^{87}Rb atoms, which include the aspheric lens pair, the magneto-optical trap (MOT), and the far-off resonance optical dipole trap (FORT). Particularly, we introduce the release-recapture scheme to quantify the atomic thermal motion, and the parametric excitation method to measure the trap profile. We also present an optical pumping technique and a fluorescence-based lossless state detection technique for atomic state preparation and detection.

2.1 Lenses in vacuum

The heart of the optical setup is a pair of customized aspherical lenses with high numerical apertures (NA). They are manufactured by Asphericon GmbH with the key properties, including the clear aperture, and the back and effective focal lengths, labeled in Fig. 2.1.

The lenses serve the purpose of tightly focusing down a probe beam and a dipole beam, as well as collimating fluorescence from a single atom. They are held together in a confocal configuration using an aluminium holder (more details are provided in Wilson Chin's thesis [74]). This structure is placed inside the vacuum chamber, maintained at ultra-high vacuum using an ion pump (Agilent Varian Starcell, 20 L/s). Particularly, a readout from the ion pump current infers the current pressure to be around 8×10^{-9} mbar, which corresponds to a mean free path of around 1.2 km (using a temperature of 300 K and collision cross section between ^{87}Rb atoms and background gas molecules of 3 nm^2 [75]). This background pressure will ultimately limit the trapping lifetime of the single atoms to be around 4 s.

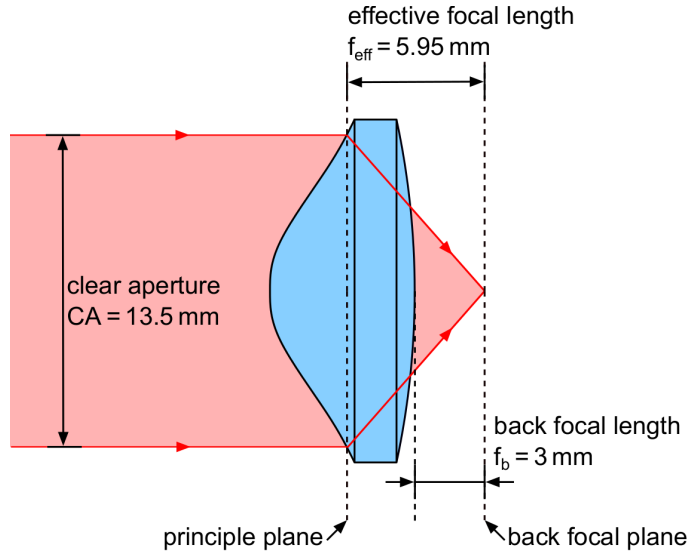


Figure 2.1: Schematic of the aspheric lens used in this work. Key parameters here are given for 780-nm light. The numerical aperture (NA) is 0.75. Anti-reflection coating on both sides of the lens ensures less than 0.5% reflection for wavelengths between 700 nm and 1400 nm.

2.2 Magneto-optical trap

A magneto-optical trap (MOT) is formed by a quadrupole magnetic field and a three-dimensional red-detuned radiation pressure force to confine and cool the atoms. Typically, a MOT has a trap depth on the order of Kelvins and a trapping range on the order of hundreds of micrometers, allowing a large number of atoms to be confined in a compact region [76]. Therefore, we can form a cold and dense atomic cloud, which is going to be the source of laser-cooled atoms for the optical dipole trap.

The MOT beams consist of 780-nm cooling light and 795-nm repump light. Both the 780-nm and 795-nm beams are generated from a home-built external cavity diode laser (ECDL) constructed with a diffraction grating in a Littrow configuration. The 780-nm cooling light is red-detuned from the $5^2S_{1/2}, F = 2 \leftrightarrow 5^2P_{3/2}, F' = 3$ closed transition by around 12 MHz using an acousto-optical modulator (AOM). The repump light, nearly resonant to the $5^2S_{1/2}, F = 1 \leftrightarrow 5^2P_{1/2}, F' = 2$ transition, brings the atoms that are off-resonantly transferred to the $F = 1$ ground state back to the $F = 2$ ground state, allowing them to resume on the closed cooling transition cycles.

CHAPTER 2. EXPERIMENTAL SETUP AND TECHNIQUES

The MOT beams are circularly polarized and retro-reflected to form three pairs of counter-propagating beams with opposite polarization. To achieve cooling in all directions, one MOT beam is placed in the horizontal direction perpendicular to the lens axis, and the other two MOT beams are placed vertically with a tilt angle of around 14° , overlapping at the center of the lens pair. The horizontal MOT beam carries cooling light of $300 \mu\text{W}$ and repump light of $180 \mu\text{W}$ with the same beam waist of 1.1 mm. On the other hand, the vertical MOT beams carry cooling light of $150 \mu\text{W}$ and repump light of $80 \mu\text{W}$, each having a beam waist of 1.1 mm.

The three pairs of MOT beams can interfere constructively or destructively at the location of the atom. Since the MOT cooling rate and scattering rate depend on the local intensity of the MOT light, we aim to avoid the interference effect that can cause a large variance in the shot-to-shot fluorescence collection. Therefore, we use piezoelectric actuators (Thorlabs KC1T-P) to stimulate movement on the mirrors that direct the vertical MOT beams into the system. Typically, an 80 Hz signal with an amplitude of 10 V continuously drives the piezos. This effectively washes out the interference effect and produces a uniformly distributed atomic fluorescence level scattered by the single atom (see the fluorescence telegraph in Fig. 2.5).

For the spatially varying Zeeman shift, a pair of coils in an anti-Helmholtz configuration is employed to generate the quadrupole magnetic field. At an operating current of 2 A, the quadrupole coils produce a magnetic field gradient of around 40 G/cm along the coil axis, and -20 G/cm in perpendicular directions at the region around the coil center. The formation of the atomic cloud can be observed on the imaging camera as the cold atoms scatter the cooling light in all directions. Figure 2.2 shows the images of the atomic cloud and also the optically trapped single atom (described in Chapter 2.3) recorded on the camera placed along the optical axis of the high NA lenses.

2.3 Far-off resonant optical dipole trap

Trapping cold atoms in a far-off resonant optical dipole trap (FORT) has become a well-established technique in the field of atomic and molecular physics, nicely summarized in several review articles [77, 78]. The main idea of this technique is to induce a position-dependent dipole force based on the interaction between a

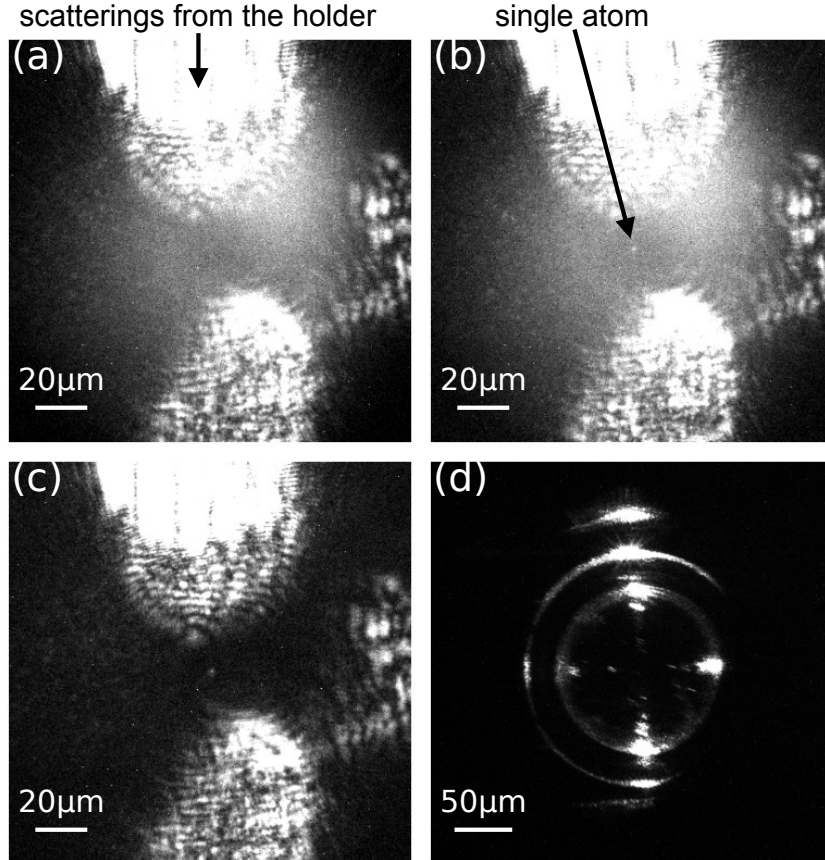


Figure 2.2: We image the focal plane of the high NA lens onto a camera placed along the optical axis (see Fig. 2.4). (a) Cooling fluorescence from the atomic cloud formed by the MOT. (b) The dipole trap is switched on and overlapped with the MOT. The presence of a bright spot indicates the loading of a single atom. (c) The dipole trap and cooling light are switched on, without the quadrupole field. The atomic cloud has been dispersed, but the trapped single atom (bright spot) can still be observed. The three clusters of white regions in (a),(b), and (c) are scatterings from the lens holder. (d) Shifting the camera imaging plane to set the clusters of white regions in focus. This adjustment allows us to identify these regions as the images of the aluminum holder.

polarizable particle and laser light, by sending an intense tightly focused off-resonant light. Here, we provide a brief overview of the theoretical background for optical trapping.

2.3.1 Theory

We consider an atomic system interacting with a classical dipole light field. The evolution of the quantum system is described by the sum of the free atomic Hamiltonian H_A and the atom–field interaction Hamiltonian $\hat{V}(t)$:

$$\begin{aligned}\hat{H}(t) &= \hat{H}_A + \hat{V}(t) \\ &= \hat{H}_A - \hat{d}E_1 \cos(\omega_1 t),\end{aligned}\quad (2.1)$$

for a dipole light with a frequency of ω_1 and a real electric field amplitude E_1 . Here, \hat{d} is the atomic dipole operator, projected to the polarization of the driving field E_1 .

By treating $V(t)$ as a weak physical disturbance, the new eigenstates are expected to exhibit only small deviations from the original atomic energy levels. Therefore, for any atomic energy level $|n\rangle$, the perturbed eigenstate can be approximated through the application of first-order time-dependent perturbation theory [79]:

$$\begin{aligned}|\psi_n(t)\rangle &\approx e^{-i\omega_n t} |n\rangle - \frac{i}{\hbar} \sum_k e^{-i\omega_k t} |k\rangle \int_0^t dt' \langle k| e^{i\hat{H}_A t'/\hbar} \hat{V}(t') e^{-i\hat{H}_A t'/\hbar} |n\rangle \\ &= e^{-i\omega_n t} |n\rangle + \sum_{k \neq n} e^{-i\omega_k t} |k\rangle \frac{d_{kn} E_1}{2\hbar} \left(\frac{e^{i(\omega_{kn} + \omega_1)t} - 1}{\omega_{kn} + \omega_1} + \frac{e^{i(\omega_{kn} - \omega_1)t} - 1}{\omega_{kn} - \omega_1} \right),\end{aligned}\quad (2.2)$$

where $\omega_{kn} = \omega_k - \omega_n$ is the energy difference between two atomic energy levels $|k\rangle$ and $|n\rangle$, and d_{kn} is the dipole moment associated with the optical transition between the $|k\rangle$ and $|n\rangle$ states.

Using these perturbative terms, one can evaluate the time-averaged energy shift (AC Stark shift) of the state $|n\rangle$ of the atom with

$$\begin{aligned}U_n &= - \lim_{T \rightarrow \infty} \frac{1}{T} \int_0^T dt \langle \psi_n(t) | \frac{\hat{d}E(t)}{2} | \psi_n(t) \rangle \\ &\approx - \sum_{k \neq n} \frac{|d_{kn}|^2 E_1^2}{4\hbar} \left(\frac{1}{\omega_{kn} + \omega_1} + \frac{1}{\omega_{kn} - \omega_1} \right) \\ &\equiv -\alpha_n(\omega_1) E_1^2,\end{aligned}\quad (2.3)$$

CHAPTER 2. EXPERIMENTAL SETUP AND TECHNIQUES

where α_n represents the dynamic polarizability of state $|n\rangle$ at frequency ω_1 . Here, all the fast oscillation (at optical frequencies) terms have been averaged out.

Some crucial properties of the optically induced energy shift can be clearly seen in the case of a two-level system. For a two-level atom described by a ground state $|g\rangle$ and an excited state $|e\rangle$ with an energy spacing of $\hbar\omega_0$, the expression in Eqn. 2.3 allows us to retrieve the celebrated results:

$$\begin{aligned}
 U_g &= -\frac{|d_{eg}|^2 E_1^2(\vec{r})}{4\hbar} \left(\frac{1}{\omega_0 + \omega_1} + \frac{1}{\omega_0 - \omega_1} \right) \\
 &= -\frac{3\pi c^2}{2\omega_0^3} \left(\frac{\Gamma}{\omega_0 + \omega_1} + \frac{\Gamma}{\omega_0 - \omega_1} \right) I(\vec{r}) \\
 &\approx \frac{3\pi c^2}{2\omega_0^3} \left(\frac{\Gamma}{\Delta} \right) I(\vec{r}) \\
 &= -U_e, \tag{2.4}
 \end{aligned}$$

for a dipole beam detuning $\Delta = \omega_1 - \omega_0$. The electric field amplitude is represented by the beam intensity $I = \epsilon_0 c E_1^2 / 2$, and the dipole moment term is substituted by the spontaneous decay term $\Gamma = \omega_0^3 |d_{eg}|^2 / 3\pi\epsilon_0 \hbar c^3$. From the expression in Eqn. 2.4, one observes that for a red-detuned light ($\Delta < 0$), the interaction is attractive for the ground state ($U_g < 0$). Therefore, focusing down a red-detuned light can create a potential well that traps an atom.

However, the condition of a red detuning ($\Delta < 0$) alone is not sufficient to ensure the functionality of optical trapping. Another mechanism that one has to consider is the radiation pressure exerted by the dipole beam. This is a dissipative process described by the rate at which a two-level system scatters the trapping light:

$$\begin{aligned}
 R_{sc} &= \frac{3\pi c^2}{2\hbar\omega_0^3} \frac{\omega_1^3}{\omega_0^3} \left(\frac{\Gamma}{\omega_0 + \omega_1} + \frac{\Gamma}{\omega_0 - \omega_1} \right)^2 I(\vec{r}) \\
 &\approx \frac{3\pi c^2}{2\hbar\omega_0^3} \left(\frac{\Gamma}{\Delta} \right)^2 I(\vec{r}). \tag{2.5}
 \end{aligned}$$

Comparing the expressions for Eqn. 2.4 and Eqn. 2.5, we can confirm that the dipole potential scales as $I(\vec{r})/\Delta$, while the scattering rate scales as $I(\vec{r})/\Delta^2$. Since the scattering rate decreases much faster than the conservative trapping potential as a function of detuning, we typically employ trapping lasers with large detunings of several THz [77]. An optical trap operating in this regime is referred to as a far-off-resonant optical dipole trap (FORT).

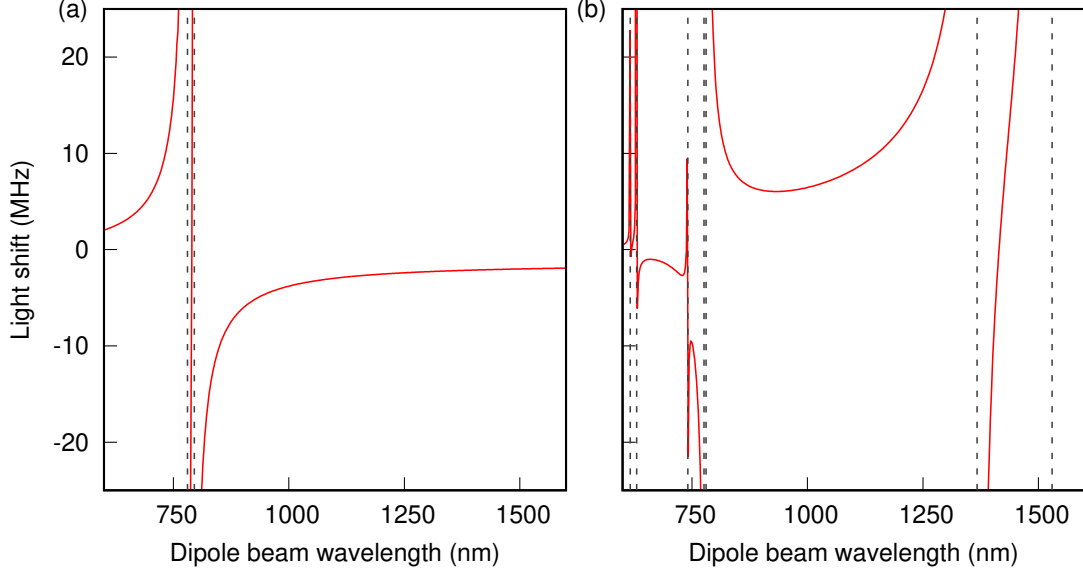


Figure 2.3: Light shift of (a) the ground state $5S_{1/2} |F = 2, m_F = 0\rangle$ and (b) the excited state $5P_{3/2} |F' = 3, m'_F = 0\rangle$ as a function of dipole beam wavelength for a dipole beam intensity at $1 \text{ mW}/\mu\text{m}^2$. Dashed lines indicate optical transitions to other fine structures.

When considering a physical atom rather than the idealized two-level system, the sum of all possible transitions has to be evaluated to calculate the overall optical potential. Particularly, the dipole coupling term can be boiled down to

$$\langle F m_F | \hat{d}_q | F' m'_F \rangle = \langle F || \hat{\mathbf{d}} || F' \rangle \langle F m_F | F' 1 m'_F q \rangle, \quad (2.6)$$

which is a product of a reduced matrix element and the corresponding Clebsch–Gordan coefficient. While in general the algebra involved can be tedious, there are already a vast number of open-source packages for various programming platforms to compute the coupling term above [80, 81]. As an example, we show the wavelength dependence of the atomic level shifts for a ^{87}Rb atom in Fig. 2.3. Here, the calculations are performed for the electrical dipole permitted transitions up to the principal quantum number of $n = 7$ for a dipole beam intensity of $1 \text{ mW}/\mu\text{m}^2$.

Generally, the dipole potential for the ground state is attractive for wavelengths longer than 795 nm, and repulsive for wavelengths shorter than 780 nm. In fact, an optical trap can also be formed using repulsive dipole light by surrounding a spatial region. The advantage of a blue-detuned dipole trap is that the atom generally stays

CHAPTER 2. EXPERIMENTAL SETUP AND TECHNIQUES

Atomic state	Scalar c_s	Vector c_v	Tensor c_t
$5S_{1/2}, F = 2$	-1.000	0.043	0.000
$5S_{1/2}, F = 1$	-1.000	-0.043	0.000
$5P_{3/2}, F' = 3$	0.742	0.122	-0.072
$5P_{3/2}, F' = 2$	0.455	0.158	0.000
$5P_{3/2}, F' = 1$	0.169	0.373	0.430
$5P_{3/2}, F' = 0$	0.455	0.000	0.000
$5P_{1/2}, F' = 2$	0.556	0.204	0.000
$5P_{1/2}, F' = 1$	0.556	-0.204	0.000

Table 2.1: Coefficients for scalar, vector, and tensor decomposition of the AC Stark shift for a dipole light of 851 nm, following the expression in Eqn. 2.7.

in the intensity minimum, which can effectively reduce the off-resonant scattering rate. There was an attempt in our group to construct a blue-detuned dipole hollow beam trap using a wavelength of 740 nm. More details about this trapping configuration are described in Boon Long Ng’s thesis [82]. In the remaining part of this thesis, we will only focus on the red-detuned dipole beam with a wavelength of 851 nm.

Accounting for the polarization of the dipole beam and the dipole strengths between Zeeman sublevels, it is possible to decompose the light shift into a compact form consisting of a scalar, a vector, and a tensor term [64, 83]:

$$\hat{H}_{I_s, F} = U_0 \left(c_s + c_v \text{Im}[\epsilon^* \times \epsilon] \cdot \hat{\mathbf{F}} + c_t |\epsilon \cdot \hat{\mathbf{F}}|^2 \right), \quad (2.7)$$

where U_0 is the dipole trap depth, ϵ the polarization unit vector of the trapping field, $\hat{\mathbf{F}}$ the total angular momentum operator, and c_s, c_v, c_t are the coefficients of the scalar, vector, and tensor light shifts, respectively. These coefficients can be computed numerically by summing over the relevant optical transitions, as given in Eqn. 2.3. The calculated values are listed in Table 2.1 for the hyperfine levels in $5S_{1/2}$, $5P_{1/2}$, and $5P_{3/2}$ manifolds. This allows us to estimate the light shifts on the hyperfine levels of interest, or conversely deduce the trap intensity from the resonance shift.

2.3.2 Implementation

To exclusively trap only a single neutral atom, the FORT needs to be formed in a tightly focused configuration. The mechanism at play here is the collisional blockade effect [84]. In the presence of cooling light, two or more atoms that are

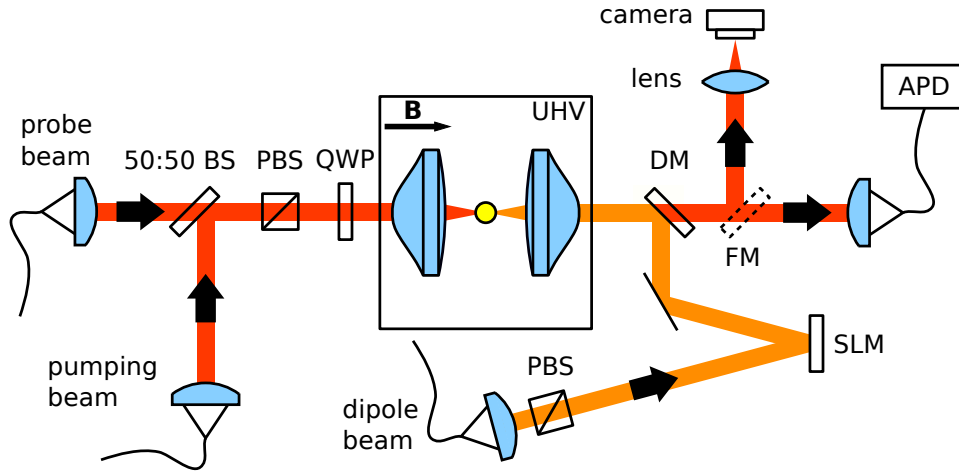


Figure 2.4: Optical setup for probing light-atom interaction in free space. A single atom is held at the joint focus of two high NA lenses using a far-off-resonant optical dipole trap (FORT) within an ultra-high vacuum (UHV) chamber. The lenses are also used to focus probe light onto the atom and to collect fluorescence light scattered by the atom. APD: avalanche photodetector, FM: flip mirror, DM: dichroic mirror, SLM: spatial light modulator, QWP: quarter-wave plate, (P)BS: (polarizing) beam splitter, B: magnetic field, UHV: ultra-high vacuum.

trapped in a small region undergo light-assisted collisions, which result in both colliding atoms being lost from the trap [85]. Figure 2.5 shows the typical signature of sub-Poissonian loading of single atoms with either zero or one atom trapped.

In our setup, the FORT is formed by tightly focusing a dipole beam using the same high-NA aspheric lens for probing light-atom interaction. Figure 2.4 shows the schematic of our optical setup. The trap laser is an 851-nm Titanium-Sapphire laser (M Squared SolsTis), pumped with a 532-nm diode-pumped solid-state laser (Coherent Verdi V10). The dipole beam is linearly polarized and collimated from a single mode fiber to have a beam radius of 2.7 mm using an off-the-shelf triplet collimator (Thorlabs TC25APC). The dipole beam is directed onto a reflective spatial light modulator (SLM, XY512L from Meadowlark Optics), which functions like a mirror by default but additionally allows for the manipulation of the wavefront of the dipole beam. This gives us the flexibility to steer the beam direction, or to form more complex beam profiles, including those that carry an orbital angular momentum [86, 87]. The dipole beam is then combined into the same beam path as the 780-nm probe beam for interfacing the atom.

CHAPTER 2. EXPERIMENTAL SETUP AND TECHNIQUES

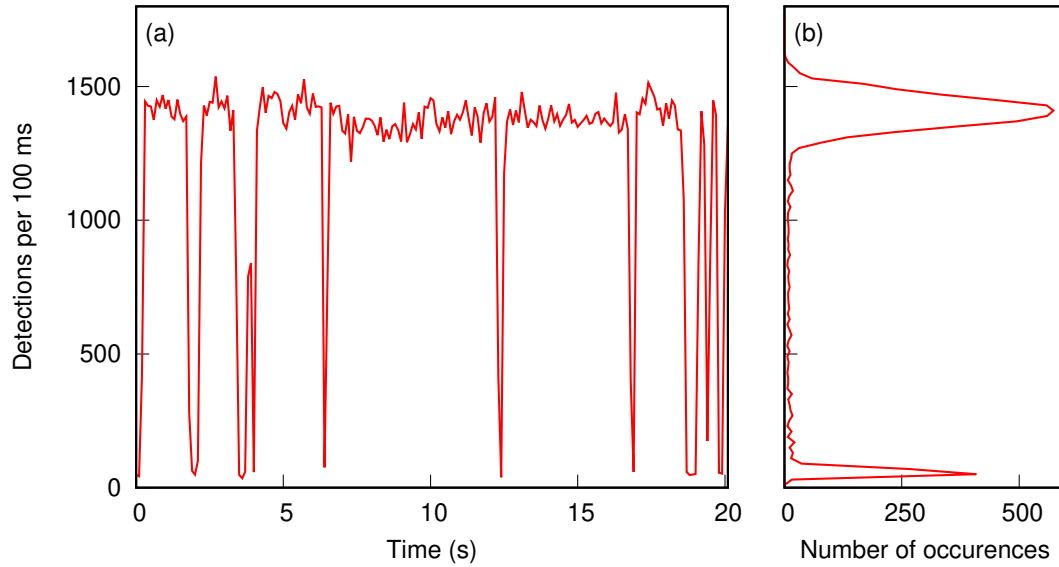


Figure 2.5: (a) Fluorescence of single atoms under continuous illumination of cooling beams. (b) Histogram of the single atom fluorescence for time traces (left) extended to ten minutes.

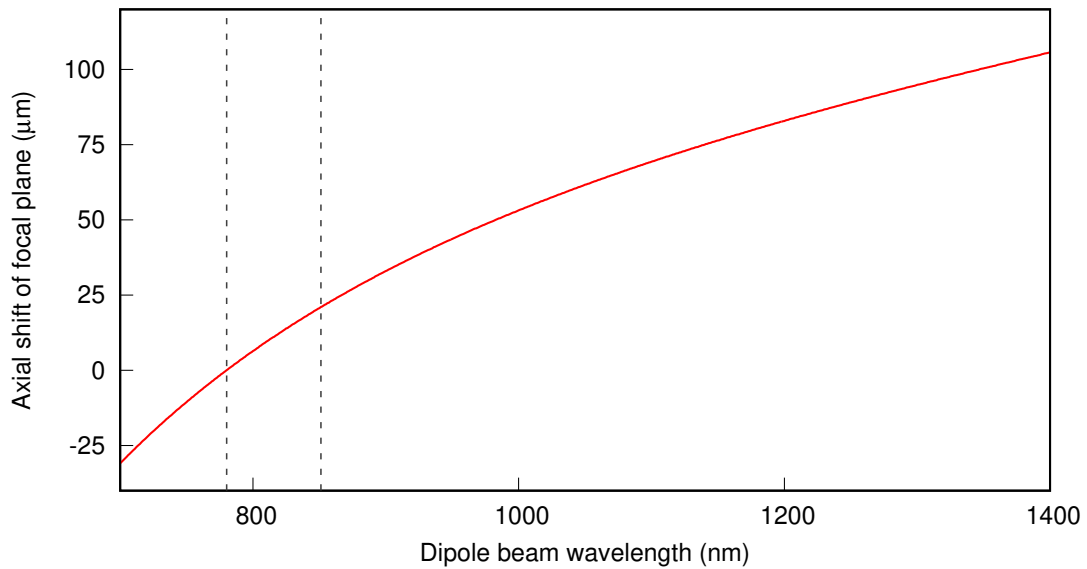


Figure 2.6: Calculated axial shift in the focal plane at different wavelengths relative to 780 nm due to chromatic aberration in the lens. The dashed lines indicate the reference at 780 nm and the wavelength of the dipole beam (851 nm).

Correction for chromatic aberrations

Ideally, the dipole beam, upon being focused down by the high NA lens, is expected to yield a Gaussian waist size of approximately $0.6 \mu\text{m}$, based on the input collimated dipole beam radius we employed. Achieving such a diffraction-limited performance would require the optics to be aberration-free, which is unfortunately not feasible since the aspheric lens was designed for a 780-nm light beam. Even worse, there will be a shift in the focal planes due to chromatic aberrations caused by the difference in wavelength between the dipole beam and the probing beam. With the surface profiles and dispersion of the lens material deduced using a Sellmeier equation, we can compute the effective and back focal lengths for a given input wavelength. As shown in Fig. 2.6, the calculations show a shift of around $21 \mu\text{m}$ between the back focal planes for collimated 780-nm and 851-nm light beams.

Conveniently, the SLM can function as a lens, allowing us to adjust the divergence of the beam, thereby facilitating the overlap of the two focal planes. To achieve the optimal alignment, we vary the focusing of the SLM phase lens to maximize the fluorescence collection in the probe mode. As a result, we obtain the highest collection for the SLM phase pattern displaying as a Fresnel lens with a focal length of 2.4 m, with the SLM positioned at a distance of approximately 1 m from the high NA lens. Using the standard ray optics propagation, the estimated focal shift of FORT is around $-f_{NA}^2/(L + f_{NA} - f_{SLM}) \approx -25 \mu\text{m}$, which is fairly consistent with the calculated axial shift in Fig. 2.6. Furthermore, the compound optical system will have an effective focal length of 10 mm, leading to an estimated diffraction-limited beam waist of $1.0 \mu\text{m}$.

Dipole power stabilization

To maintain a stable power level for the dipole trap over time, we implement the following power stabilization scheme: we sample a small part of the dipole beam power before it enters the high NA lens and measure it using a photodiode. Subsequently, the photodiode reading and an analog input (reference power level) are fed into a differential amplifier to generate an error signal for the reference level. The error signal is directed to control a radiofrequency (RF) attenuator, which in turn, regulates the RF power supplied to drive the AOM associated with the dipole beam. As this power stabilization scheme is employed only for long-term stability,

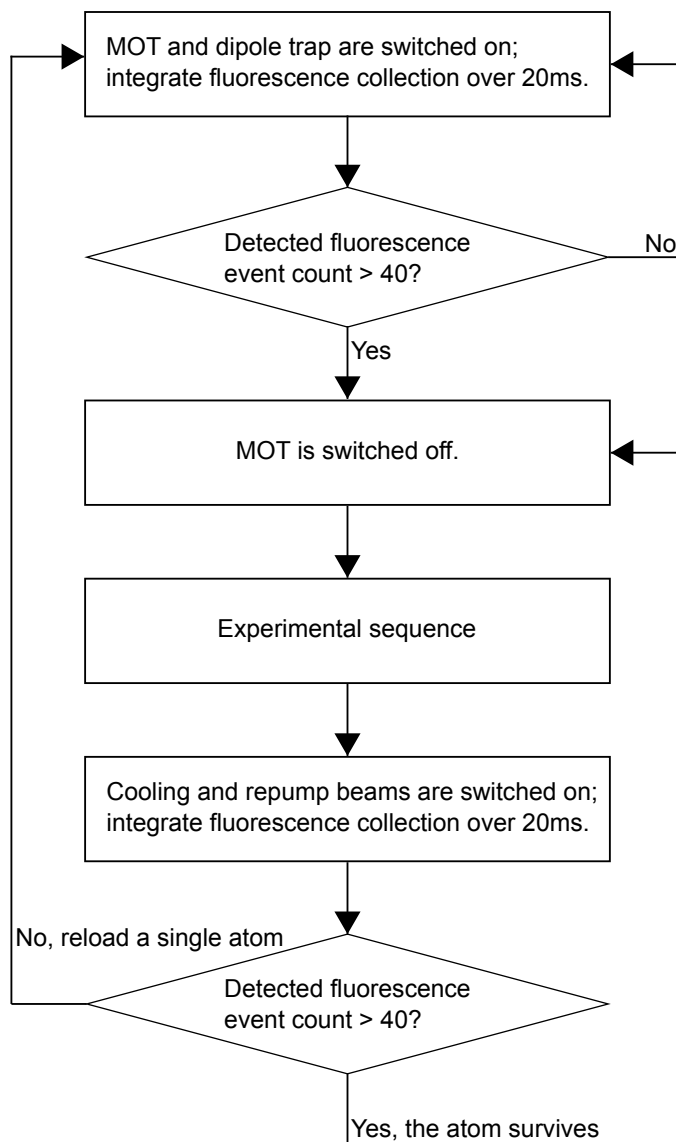


Figure 2.7: Flowchart illustrating a standard experimental sequence.

the control bandwidth is limited to about 500 Hz.

For the loading of a single atom, we employ a dipole beam power of 11.6 mW, which corresponds to a trap depth of $k_B \times 2$ mK. However, for experiments involving clean atomic spin states, we will ramp down the dipole beam power to a typical trap depth of $k_B \times 0.86$ mK (at an input power of 5.04 mW) to avoid detrimental tensor light shift effects.

2.3.3 Loading an atom into dipole trap

The experimental sequence is run on a home-built digital pattern generator based on a field-programmable gate array (FPGA), which allows for sequence branching conditioned on the input counts. A basic sequence is illustrated in Fig. 2.7. We always start with forming a cold cloud of ^{87}Rb atoms using a MOT. To load a single atom, the MOT is spatially overlapped with the FORT. Once an atom is loaded into the FORT, the count rate on the APD will increase from 200s^{-1} to 7000s^{-1} . This fluorescence will be collected by our experimental control system during a qualifying time window of 20 ms. If more than 40 photoevents are detected in this window, an atom is loaded into the dipole trap with a high probability (we refer to this as the “fluorescence trigger”). On qualification, the system branches to a sequence where the MOT is turned off to prevent further loading. Then the preloaded experimental sequence will take place, before a second qualifying test to exclude measurements where the atom was lost. If the atom survives the second qualifying test, the control system will branch back to the experimental sequence again. Otherwise, the MOT beams and quadrupole field will be switched on again for forming the ^{87}Rb cloud in order to load a new atom into the FORT again.

2.3.4 Atom lifetime

The atomic lifetime is an important parameter because it determines the number of successful measurements that can be performed in a given time window, enabling the accumulation of data for improved statistical accuracy. It is also an indication of the atomic temperature since atoms with higher energy tend to escape the dipole trap faster. Nonetheless, the atomic lifetime is notably influenced by the specific experimental sequence, as the light scattering can significantly elevate the atomic temperature.

We empirically measure the lifetime of the single atoms in the dipole trap without continuous illumination of the MOT beams, which should be the upper bound for how long an atom can stay inside a dipole trap. This can be determined by measuring the survival probability after a certain duration, upon confirming that there is an atom loaded into the trap. The measurement result is shown in Fig. 2.8. The survival probability fits an exponential curve with a decay time of around $2.51 \pm 0.06\text{ s}$. This

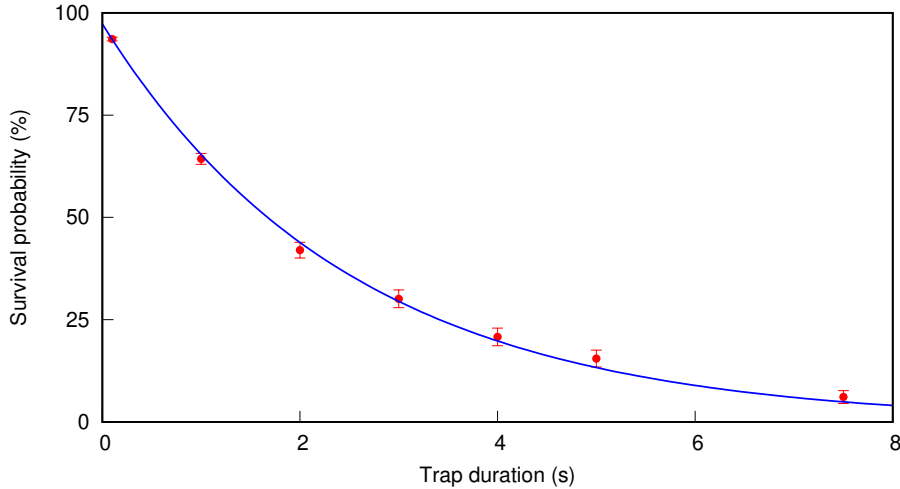


Figure 2.8: Lifetime of the atom in the optical dipole trap. The solid line represents a fit to the exponential function, indicating a lifetime of 2.5 s. Error bars represent the standard error of binomial statistics accumulated from 200-3000 repeated sequences.

dark lifetime should be mainly limited by one-body loss due to the collisions with fast atoms from the background gas. In our system, a typical experimental sequence lasts about 100 ms, which implies that each atom loading results in approximately 25 experimental runs on average.

2.3.5 Dipole trap as a harmonic trap

Near the bottom of the dipole trap, the Gaussian trap can be approximated as a harmonic trap by performing a Taylor expansion on the radial distance ρ and axial distance z from the trap center:

$$\begin{aligned}
 U(\mathbf{r}) &= -U_0 e^{-2\rho^2/w(z)^2} \frac{1}{1 + (z/z_R)^2} \\
 &\approx -U_0 \left(1 - \frac{2}{w_0^2} \rho^2 - \frac{1}{z_R^2} z^2 \right),
 \end{aligned} \tag{2.8}$$

where U_0 is the trap depth, w_0 the beam waist, z_R the Rayleigh range. By comparing the quadratic terms, we obtain the trap frequencies as a function of the beam intensity and geometry, as given by

$$\omega_\rho = \sqrt{\frac{4U_0}{mw_0^2}}, \quad \omega_z = \sqrt{\frac{2U_0}{mz_R^2}}, \tag{2.9}$$

where m is the mass of the atom.

CHAPTER 2. EXPERIMENTAL SETUP AND TECHNIQUES

To measure the trap frequencies, we parametrically heat the atoms by modulating the trap laser power. This can be seen from Eqn. 2.9, which states that the square of trap frequency is proportional to the trap potential. In the presence of a sinusoidal modulation in trap power, the atomic motion can be mathematically represented as a Mathieu equation [88]:

$$\ddot{x}(t) + \omega_0^2(1 + h \sin(\omega_m t))x(t) = 0, \quad (2.10)$$

where x represents the position of the atom relative to the trap center, ω_0 the trap frequency, ω_m the modulation frequency, and h the modulation depth. Although the solutions for Eqn. 2.10 cannot be represented analytically with standard functions, it is known that the motion will become unbounded at the primary parametric resonance frequency at $\omega_m^{(\text{res})} = 2\omega_0$ [89].

To drive the parametric resonances for the various atomic motional degrees of freedom, we run the following experimental sequence: after successful loading of a single atom, we switch off the MOT beams and quadrupole field, leaving the FORT on. We then modulate the power of the dipole beam at a modulation frequency ω_m by sinusoidally modulating the amplitude of the radio frequency (RF) voltage that drives the dipole beam AOM. This modulation is applied for a duration of $\tau_m = 100$ ms for the lower modulation frequencies ($\omega_m/2\pi$ between 5 kHz and 40 kHz) and modulation depth of 35 %. For the higher modulation frequencies ($\omega_m/2\pi$ between 45 kHz and 200 kHz), we apply the modulation for a duration of $\tau_m = 10$ ms with a modulation depth of 25 %. The longer modulation duration for the lower frequency is to ensure the parametric heating undergoes a similar number of oscillation cycles. Lastly, we detect the presence of a single atom by collecting the fluorescence from the illumination of cooling beams. By scanning the modulation frequency ω_m , we observe a reduction in atom survival probability in the trap at the parametric resonance frequency.

As shown in Fig. 2.9, we observe a reduction of atom survival probability at 20 ± 1 kHz and 147 ± 5 kHz. Knowing that a focused Gaussian beam trap is typically anisotropic (stronger confinement in the radial direction), we then deduce an axial frequency of $\omega_z/2\pi = 10 \pm 0.5$ kHz and a radial frequency of $\omega_\rho/2\pi = 73.5 \pm 2.5$ kHz.

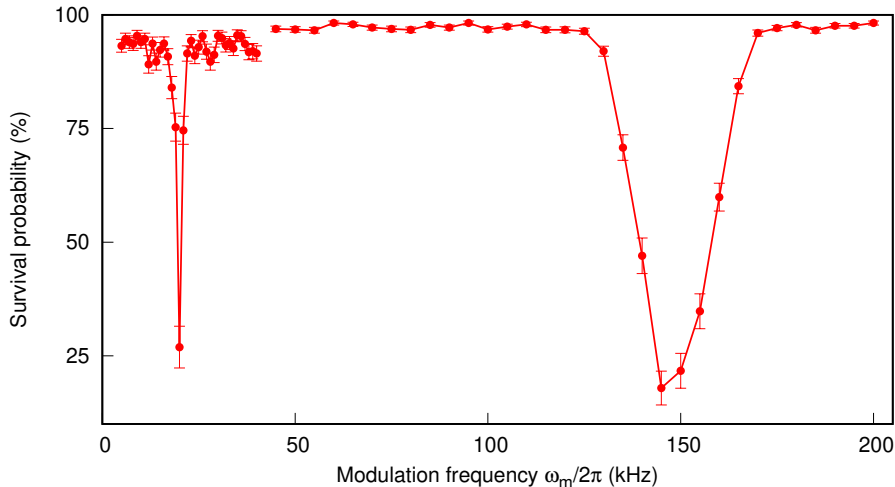


Figure 2.9: Parametric heating of the optically trapped atom to determine trap frequencies. We observe parametric resonances at $2\omega_z = 2\pi \times (20 \pm 1)$ kHz and $2\omega_\rho = 2\pi \times (147 \pm 5)$ kHz. Error bars represent the standard error of binomial statistics accumulated from 100-900 repeated sequences.

2.4 Polarization gradient cooling

For simplicity, a qubit system interacting with a flying photon is commonly assumed to be a static object. Practically, a single atom will always carry kinetic energy and move around in the dipole trap. This is generally undesired because atomic motion will introduce light shifts with respect to the light field. There are two mechanisms behind this: the Doppler shift due to the relative velocity between the atom and the light field, and the position-dependent light shift due to the relative position between the atom and the center of the dipole trap.

To mitigate these unwanted thermal effects, an efficient cooling method is necessary. For alkaline atoms with more than two Zeeman states, it has been known that polarization gradient cooling (PGC) is a well-established method to achieve sub-Doppler cooling [90, 91]. When subject to a pair of counter-propagating σ^+ - σ^- cooling light beams, the atomic motion will adiabatically redistribute population within the spin states of the ground state manifold, which gives rise to an unbalanced radiation pressure to slow the atom down. This phenomenon can be simplified as a damping coefficient that relies on the intensity of the cooling light. Experimentally, we employ the cooling scheme by using an optimized reduced cooling light power.

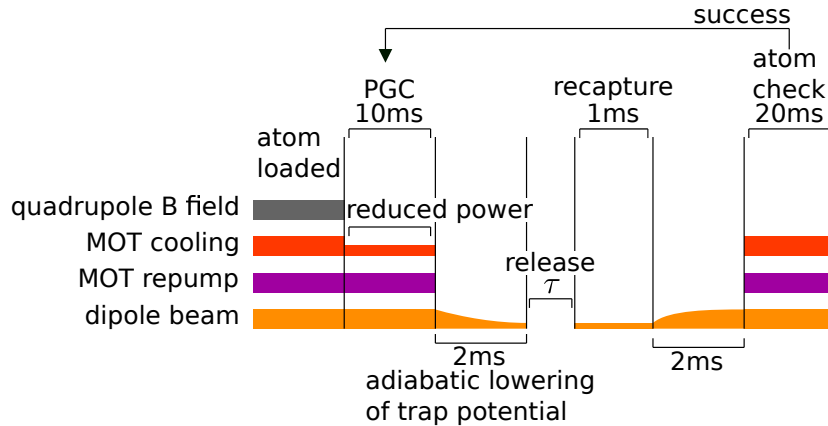


Figure 2.10: Experimental sequence for “release-and-recapture” technique to characterize atomic temperature.

2.4.1 Temperature characterization

To quantify the atomic temperature, we implement the standard release-and-recapture technique as described in [92]. The fundamental idea behind this approach is to gain insights into the energy distribution of a single atom by switching off the dipole trap for a variable time τ for the atom to diffuse away from the trapping region, and then determining the probability of recapturing the atom. Since an atom with higher energy travels faster, the atom can escape the trapping region in a shorter release interval τ , as compared to the atoms with lower energy.

The experimental sequence is shown in Fig. 2.10. After a single atom is successfully loaded into the FORT, we perform PGC for 10 ms by reducing the total power of the three cooling beams to $50 \mu\text{W}$ from $600 \mu\text{W}$. It is worth mentioning that due to the AC Stark shift exerted by the dipole trap, the cooling light is effectively $\Delta/2\pi = -67 \text{ MHz}$ red-detuned from the $F = 2 \leftrightarrow F' = 3$ closed transition. We then switch off the MOT beams and ramp down the dipole beam power. This is because at the end of PGC, the atoms typically have a low temperature of around tens of μK . The reduced FORT potential (from 2 mK to 0.86 mK trap depth) allows the atom to escape more easily, giving us a better signal to work with. In the next step, we release the atom by switching off the dipole beam over 13 different intervals ranging from $1 \mu\text{s}$ to $80 \mu\text{s}$. Finally, we recapture the atoms by switching on the dipole beam and detect the presence of the single atom by fluorescence detection with the MOT beams.

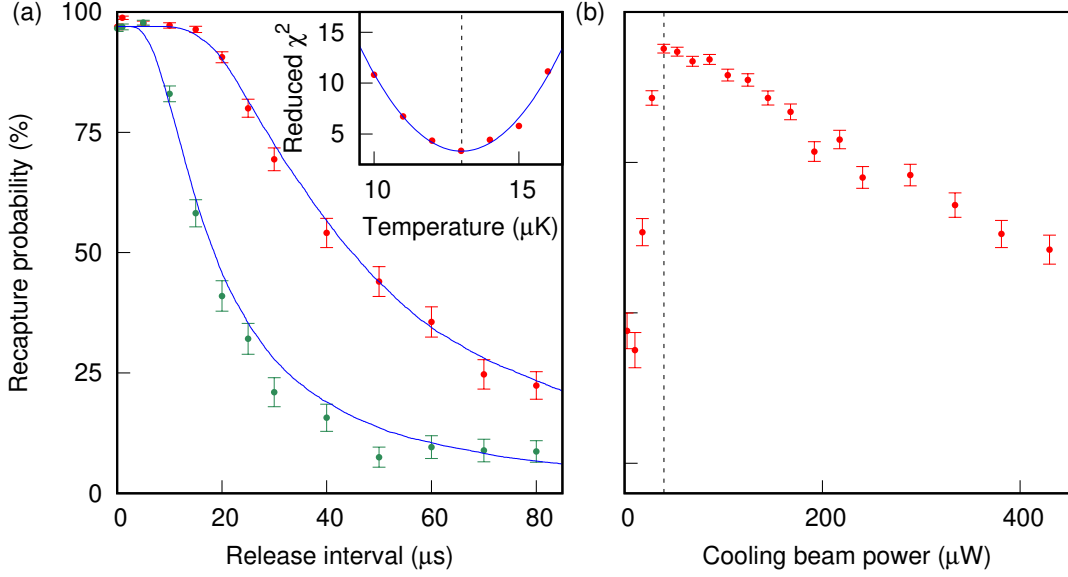


Figure 2.11: (a) Release-and-recapture measurement to deduce atomic temperature. Comparison of atom recapture probabilities to the Monte Carlo simulation (blue lines) shows that atomic temperature is around $13 \pm 0.3 \mu\text{K}$ (red points) after performing PGC and around $49 \pm 1 \mu\text{K}$ (green points) without performing PGC. Error bars represent the standard error from binomial statistics. Inset: Extracted χ^2 from the fit to the Monte Carlo simulation for atoms of various temperatures after performing a PGC. (b) Recapture probabilities after a release interval of $20 \mu\text{s}$ for various cooling beam powers set during the PGC stage. The highest recapture probability is observed for $50 \mu\text{W}$, indicated by the dashed line.

The “release-and-recapture” result after applying a PGC sequence is indicated by the red points in Fig. 2.11(a). From these measurements, we deduce that the typical temperature achieved after applying a PGC sequence is around $13.0 \pm 0.3 \mu\text{K}$. As a comparison, we also include the recapture probabilities without performing PGC, indicated by green points. The temperature observed without performing PGC is determined to be $49 \pm 1 \mu\text{K}$.

The choice of applying PGC with a total cooling power of $50 \mu\text{W}$ is empirically determined. We compare the recapture probabilities with the release interval $\tau = 20 \mu\text{s}$ after performing a PGC at varying cooling beam optical powers. The measurement result is shown in Fig. 2.11(b). This outcome will serve as the point of reference for subsequent experiments.

2.5 Ground state manipulation

For probing atom-photon interaction, we choose to restrict ourselves to only the $5^2S_{1/2}, F = 2, m_F = -2$ and $5^2P_{3/2}, F' = 3, m_{F'} = -3$ states. This necessitates the implementation of an optical pumping sequence to prepare the atom in the desired electronic state at the beginning of each experimental run. To this end, a state-selective detection scheme is employed to verify the optical pumping by monitoring the variations in atomic population over time.

2.5.1 Hyperfine state detection

We employ a lossless state-detection scheme to discriminate the hyperfine state of the atom [93]. In every readout attempt, we detect the atomic fluorescence by interrogating the atom with a weak 780-nm probe light near resonant to the $5^2S_{1/2}, F = 2 \leftrightarrow 5^2P_{3/2}, F' = 3$ transition. If the atom is in the $5^2S_{1/2}, F = 1$ (dark) state, this state-detection light is detuned from the nearest optical transition by more than 6 GHz, and thus the atom will not scatter any photon. In contrast, when

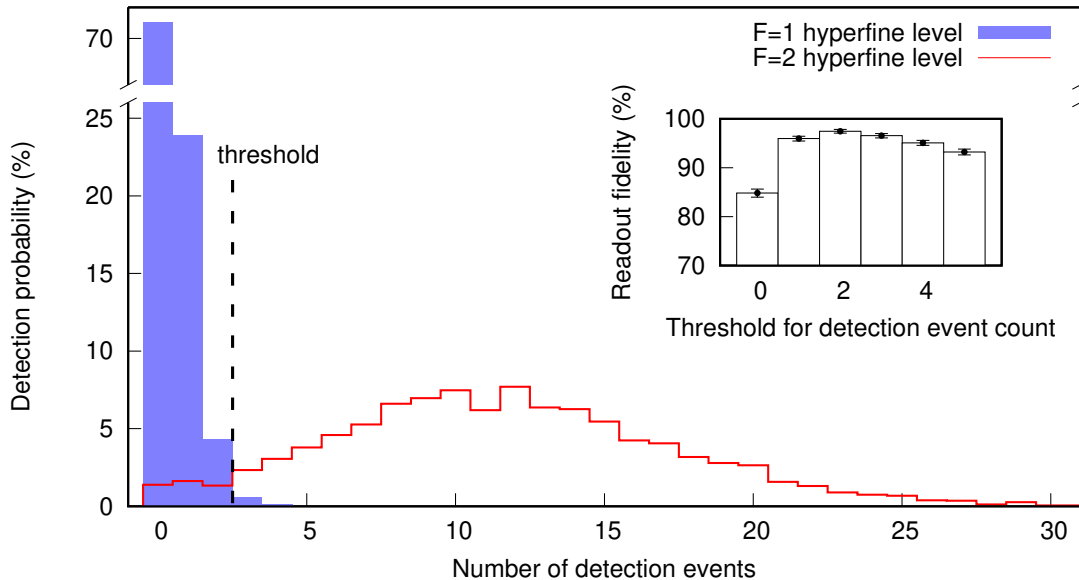


Figure 2.12: Histogram for fluorescence detection probability with a weak on-resonant excitation beam for atoms prepared in a bright state (red) and a dark state (blue), respectively. Inset: Readout fidelity F for setting different detection thresholds. The highest state readout fidelity is $97.4 \pm 0.4\%$ for a set threshold of 3 detection events.

the atom is initially prepared in the $5^2S_{1/2}, F = 2$ (bright) state, the incident light is almost on resonance, facilitating the observation of multiple scattering events.

To verify the state-detection scheme experimentally, we prepare the atom in the bright state by illuminating the atom with only MOT repumper light, before collecting fluorescence scattered by the on-resonant probe light over $600 \mu\text{s}$. We then repeat this again after depumping the atom into the $F = 1$ dark state by applying the red-detuned cooling beams for 10 ms. Figure 2.12 shows the typical histogram of detected fluorescence, accumulated for around 3300 experimental runs. We see that for the dark state, the average photodetection number \bar{n}_d is 0.36. For the bright state, we have an average photodetection number of $\bar{n}_b = 11.7$.

As the two distributions are clearly separated, it is possible to discriminate the two hyperfine states from the number of detection events. We define the readout fidelity F to be the probability with which the correct atomic hyperfine state is inferred in a single readout attempt. This probability is averaged over the two scenarios of initializing in either the bright state or the dark state with equal chance, which gives

$$F = \frac{1}{2} \left(P(\text{detect dark}|\text{dark}) + P(\text{detect bright}|\text{bright}) \right). \quad (2.11)$$

By analyzing the collected fluorescence data above, using a discrimination threshold of 3 detection events results in the highest readout fidelity of $97.4 \pm 0.4\%$ (see the inset of Fig. 2.12). At this set threshold, there is a probability of $95.6 \pm 0.4\%$ ($99.2 \pm 0.2\%$) to detect more than or equal to (less than) 3 detection events for an atom prepared in the bright (dark) state.

2.5.2 State initialization by optical pumping

To ensure the validity of assuming a ^{87}Rb atom to be a clean two-level system, we mostly focus on the $F = 2, m_F = -2 \leftrightarrow F' = 3, m_{F'} = -3$ closed transition in this thesis. Hence, at the beginning of each experimental run, the atom has to be prepared in the $F = 2, m_F = -2$ state for interfacing with the incoming probe light. To this end, we adopt the standard optical pumping technique [94]. A circularly σ^- polarized repumping laser at 795 nm, which resonantly drives the transition from $5^2S_{1/2}, F = 1$ to $5^2P_{1/2}, F' = 2$, is applied along the optical axis to transfer the atomic population to $F = 2$. At the same time, a pumping laser is applied

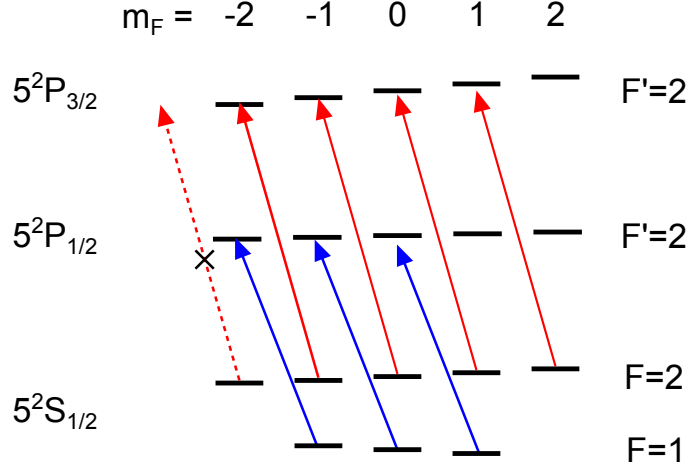


Figure 2.13: Optical pumping to prepare single atoms in the maximal Zeeman state. The red (blue) arrows indicate the transitions driven by the circularly σ^- polarized 780-nm pumping (795-nm repumping) light. Single atoms will be decoupled from the pumping light once it ends up in the $5^2S_{1/2}$, $F = 2$, $m_F = -2$ Zeeman state since no allowed transition exists.

along the optical axis with the same σ^- polarization, such that transitions from $5^2S_{1/2}$, $F = 2$ to $5^2P_{3/2}$, $F' = 2$ with $\Delta m_F = -1$ are driven (see Fig. 2.13). In this way, the single atom will be decoupled from the pumping light once it ends up in the $5^2S_{1/2}$, $F = 2$, $m_F = -2$ state, avoiding additional recoil heating due to fluorescence scattering.

To investigate the performance of our optical pumping scheme, we measure the atomic hyperfine state following the application of the pumping lights for different pumping durations. For an atom initialized in a mixture of different Zeeman states in $F = 2$ by the MOT repumper beams, the σ^- pumping beam depumps the atomic state with a time constant of $600 \pm 50 \mu\text{s}$, as shown in Fig. 2.14(a). We observe that the steady-state bright state population is not zero. This is compatible with the fact that the atom is decoupled from the depumping process once it is transferred into the desired $F = 2$, $m_F = -2$ state. In Fig. 2.14(b), we deduce a time constant of $110 \pm 20 \mu\text{s}$ by applying the σ^- repumper light on the atom initialized in the $F = 1$ state with the red-detuned MOT cooling lights. With both the σ^- pumping and repumping light in operation, a single atom can be deterministically prepared in the $F = 2$, $m_F = -2$ state with an exponential time constant of $135 \pm 30 \mu\text{s}$ (see Fig. 2.14(c)). In the following experiments, we typically perform the optical

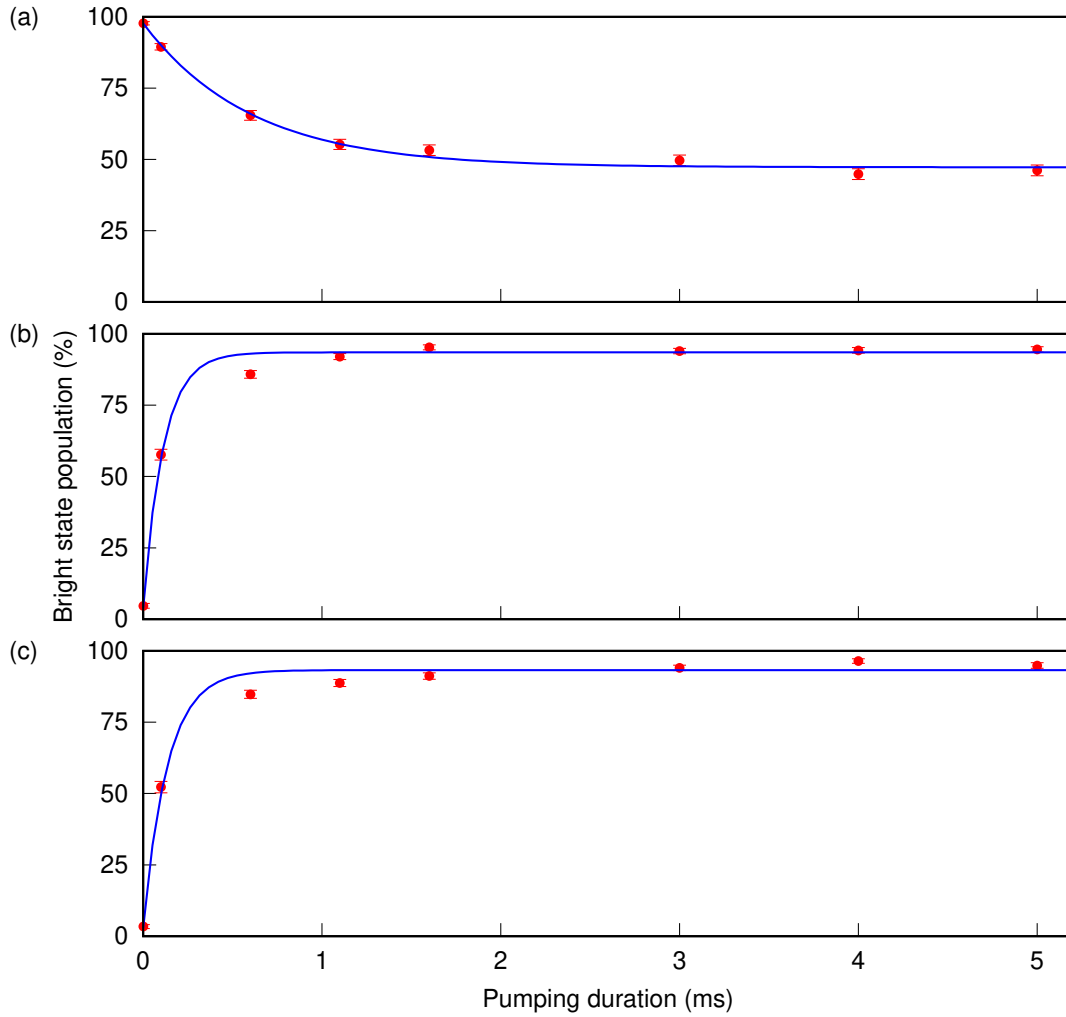


Figure 2.14: Optical pumping to prepare a single atom in the maximal Zeeman state. Three measurements are performed to confirm the proper functioning of optical pumping: (a) depumping beam only for the atom initialized in the $F = 2$ ground state, (b) repumping beam only for the atom initialized in the $F = 1$ ground state, and (c) both depumping and repumping beams for the atom initialized in the $F = 1$ ground state. Error bars represent the standard error of binomial statistics accumulated from around 300 repeated sequences.

pumping for 10 ms.

2.6 Transmission measurement

We routinely perform transmission measurements on a single atom to benchmark the system: (1) to estimate the mode-matching efficiency between the atomic dipole mode and probe mode, and (2) to measure the AC Stark shift induced by the dipole beam from the resonant frequency shift.

The experimental sequence is described in Fig. 2.15. After the atom is loaded, we apply 10 ms of PGC to cool the single atom down to $13 \mu\text{K}$. Then, we lower the trap depth and switch on the quantization magnetic field of 14.4 G along the optical axis. An optical pumping scheme prepares the atom in the state $5^2\text{S}_{1/2}$, $F = 2$, $m_F = -2$ as described in Chapter 2.5.2. Next, we apply 780-nm probe light resonant with the $5^2\text{S}_{1/2}$, $F = 2$, $m_F = -2 \leftrightarrow 5^2\text{P}_{3/2}$, $F' = 3$, $m'_F = -3$ transition for 1 ms at various probe detunings, and record the transmission on the APD (mean photodetection number $\bar{n} = 60$). As a reference, we also want to record the transmission without the atom taking part in the scattering process. Therefore, we apply for 5 ms red-detuned MOT cooling light without a repumper beam to depump the atomic state to the $5^2\text{S}_{1/2}$ $F = 1$ dark state, before applying probe light again for reference. Finally, we check if the atom is still present in the trap by measuring the fluorescence from cooling light. If the atom is gone, there is a chance that the atom loss happens during the probing stage and that will cause a problem to the measurement. The transmission data will be discarded in this case and we will wait for the next atom loading. Else, we will go back to the PGC step and repeat the procedures.

A typical transmission spectroscopy measurement is shown in Fig. 2.16. The probe transmission is obtained by normalizing the transmitted photon count in the bright state over the transmitted photon count in the dark state. Probe detuning in the x -axis refers to the frequency from the $5^2\text{S}_{1/2}$ $F = 2 \leftrightarrow 5^3\text{P}_{3/2}$ $F' = 3$ D_2 spectroscopy line. From the fit to a Lorentzian function (solid line), we can infer a linewidth of $2\pi \times (7.0 \pm 0.2)$ MHz and extinction of $21.2 \pm 0.4\%$. This allows us to deduce the mode-matching coefficient $\Lambda = 5.6 \pm 0.1\%$ according to Eqn. 1.3.

The transmission resonance is around $2\pi \times (9.4 \pm 0.1)$ MHz blue shifted from the D_2 spectroscopy line. This is due to magnetic Zeeman shift ΔE_B and dipole trap

CHAPTER 2. EXPERIMENTAL SETUP AND TECHNIQUES

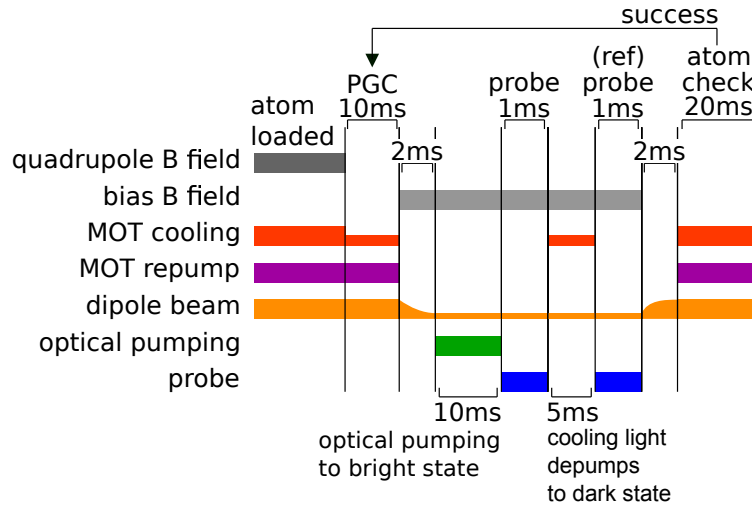


Figure 2.15: Experimental sequence for measuring transmission.

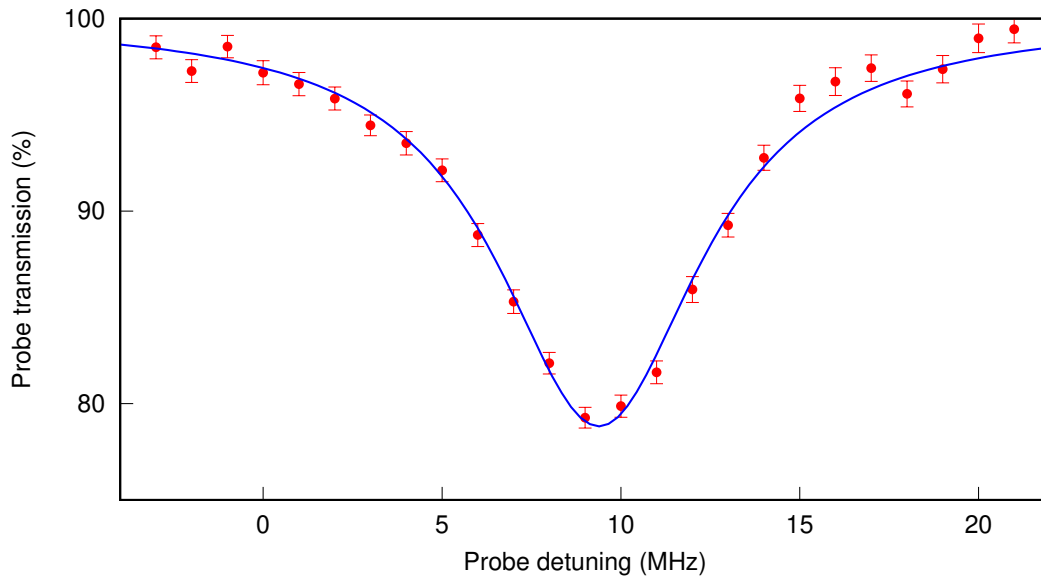


Figure 2.16: Transmission spectroscopy for a weak coherent laser. The solid line is a fit to a Lorentzian function. Error bars represent the standard error of the mean determined from around 800 repeated experimental sequences.

light shift ΔE_{AC} . With the bias magnetic field of 1.44 mT applied, the corresponding Zeeman shift between the two levels is approximately $\Delta E_B/h = 20$ MHz. Comparing to the AC Stark shift calculations in Eqn. 2.7, we can deduce a trap depth of $U_0 = k_B \times (0.864 \pm 0.003)$ mK.

Ideally, the transmission linewidth should match the natural linewidth of the atom, $2\pi \times 6.065$ MHz. Here, the measured linewidth is slightly broader (by $2\pi \times 1$ MHz) than the natural linewidth. We hypothesize that this broadening arises from the position-dependent light shift in the dipole trap, caused by the thermal distribution of the atoms.

2.6.1 Absorption imaging of single atom

In the previous part, the transmission measurement is performed with the probe light projected into the well-defined spatial mode of a single-mode fiber. Here we explore the possibility of conducting a transmission measurement using a camera, which could possibly provide us with more spatial information about the mode-matching between the probe mode and atomic dipole mode.

The experimental sequence for the absorption imaging on a camera follows the sequence outlined in Fig. 2.15. The sole distinction lies in the fact that rather than detecting transmitted photons with an APD, we capture images with a complementary metal-oxide-semiconductor (CMOS) camera (PCO panda 4.2) with a pixel size of $6.5 \times 6.5 \mu\text{m}^2$. Here, after the probe beam interacts with the atom and passes through the high NA lens pair, it is directed into the camera imaging system using a flip mirror. An imaging lens (achromatic doublet AC254-100-B, focal length $f = 100$ mm) focuses down the probe beam onto the camera, which is externally triggered by a signal connected to our experimental control system. We capture two photos for each experimental sequence: one image taken when the atomic absorption is present (signal), and another image taken when the atom is depumped into the dark state (reference). We repeat the experimental sequences for a total of around 300,000 runs.

The processed images are shown in Fig. 2.17. In these images, we have already corrected the background counts using a mean background count rate per pixel of 34.0 s^{-1} , empirically determined from the dark region far from the probe spot. Then,

CHAPTER 2. EXPERIMENTAL SETUP AND TECHNIQUES

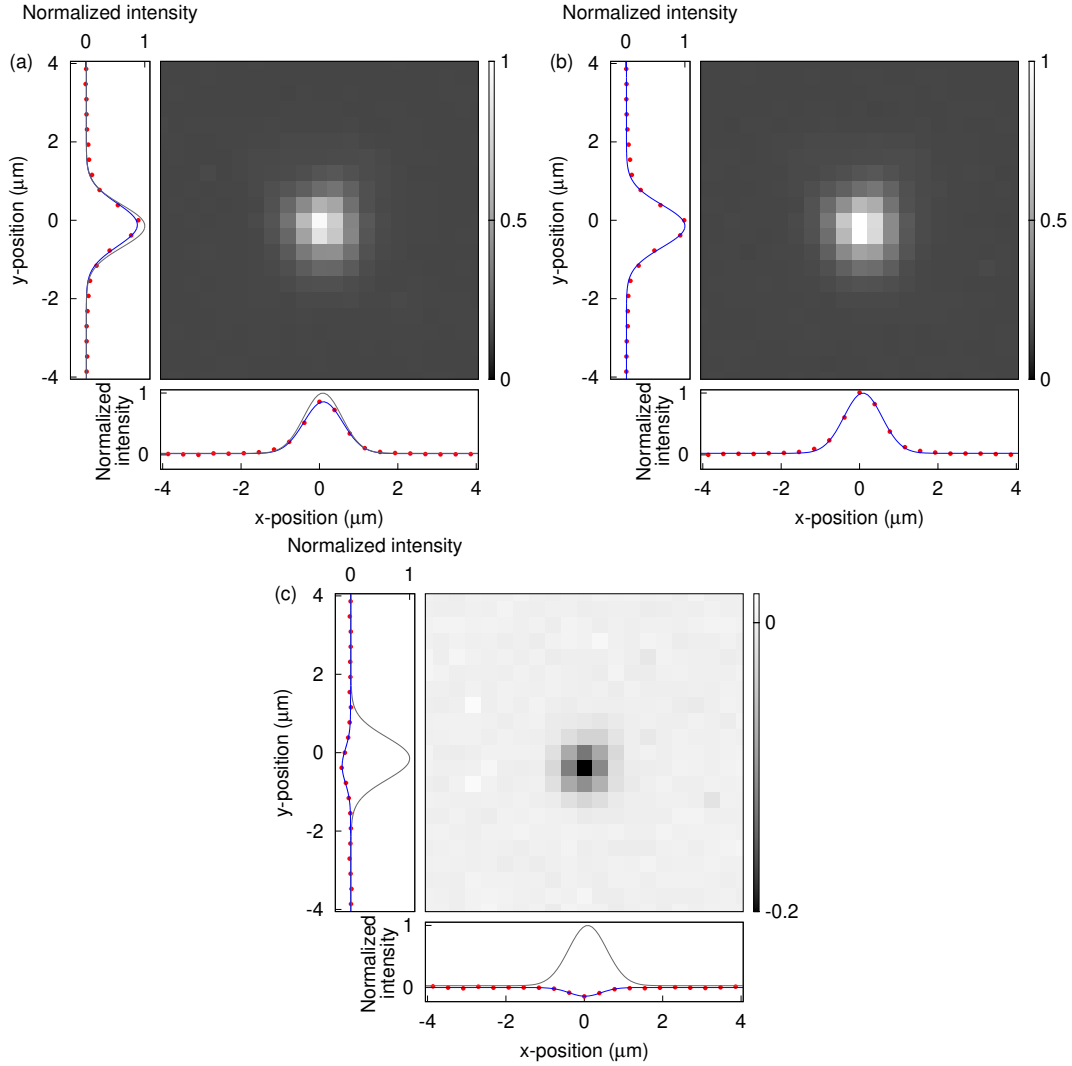


Figure 2.17: The signal (a), reference (b), and absorption (c) images of a single ^{87}Rb atom probed with a weak, on-resonant coherent light, averaged over 30,000 photos. The normalized intensities averaged over x - and y -axes are displayed alongside the images. For better visualization and comparison, the intensity profile for the reference image is duplicated in the other subplots as gray solid lines.

CHAPTER 2. EXPERIMENTAL SETUP AND TECHNIQUES

the absorption image (Fig. 2.17(c)) is obtained by subtracting the signal image (Fig. 2.17(a)) from the reference image (Fig. 2.17(b)). We compute the extinction of the probe light on every pixel of the absorption image, following the expression:

$$1 - T = \frac{I_{\text{ref}} - I_s}{I_{\text{ref}}}. \quad (2.12)$$

We observe a maximum extinction of $19.9 \pm 0.4\%$, in agreement with the value measured on an APD coupled to a single-mode fiber.

We now examine the spatial profile obtained from the absorption images. Ideally, the shadow spot area should follow the dipole scattering cross-section $(3/2\pi)\lambda^2$, scaled with a magnification factor (≈ 16.8) determined by the imaging system. Similarly, the probing beam spot will have an area following the diffraction-limited cross-section $(\pi/2)w^2$, scaled with the same magnification factor. The expected $1/e^2$ radii for the shadow spot and the probing beam spot imaged by the camera are $7.23 \mu\text{m}$ (1.1 pixels) and $9.19 \mu\text{m}$ (1.4 pixels), respectively.

A Gaussian fit to the probing beam spot determines the $1/e^2$ beam radius to be 2.58 ± 0.03 pixels ($16.8 \mu\text{m}$) in the x -direction and 2.82 ± 0.03 pixels ($18.3 \mu\text{m}$) in the y -direction. These measured values are approximately $1.9\times$ larger than the expected diffraction-limited beam radius. Interestingly, for the shadow spot, we are able to observe a slightly smaller $1/e^2$ radius of 2.2 ± 0.1 pixels ($14.3 \mu\text{m}$) in the x -direction and 2.3 ± 0.1 pixels ($15.0 \mu\text{m}$) in the y -direction. These values are consistent with the spot size obtained from the fluorescence imaging (an exemplary image is shown in Fig. 2.2(c)). We hypothesize that these values are already limited by the spatial resolution of the imaging system, caused by the aberrations stemming from the optical elements used for camera imaging. By further improving the performance of the spatial imaging, we anticipate that this technique could allow for the direct imaging of atomic motion [38, 95], which could provide more insights into the role of atomic position spread in the absorption of light.

Chapter 3

Resonance fluorescence

In this chapter, we focus on measuring the power spectrum of the atomic fluorescence scattered by a ^{87}Rb atom utilizing a Fabry-Perot cavity. By elevating the intensity of the driving field into the saturation regime, the spectrum shows the emergence of the Mollow triplet phenomenon. With an off-resonant driving field, we confirm the presence of asymmetry in the intensity correlations between photons originating from the two sidebands of the fluorescence spectrum.

3.1 Theoretical background

The resonance fluorescence of a two-level system is one of the fundamental phenomena in quantum optics and has attracted great attention since the 1960s. Experiments have been performed in various platforms (including an atomic ensemble [96], trapped ions [97, 98], a single molecule [52], quantum dots [99–103], and superconducting qubits [104–106]) and the theories have been capitulated in great details in numerous textbooks [107, 108]. Here we briefly outline some key theoretical results to facilitate discussion.

Intensity of scattered field

Let us consider the scenario where a monochromatic driving field is interacting with a two-level atom. We will label the ground state and the excited state as $|g\rangle$ and $|e\rangle$ with energies 0 and $\hbar\omega_0$, respectively. Conventionally, light scattered by a two-level atom is described as having two distinct components: a coherent component and an incoherent component. The total scattering rate R_{sc} can then be

expressed as

$$R_{\text{sc}} = R_{\text{coh}} + R_{\text{incoh}} , \quad (3.1)$$

with R_{coh} the scattering rate for the coherent component and R_{incoh} the scattering rate for the incoherent component.

For a driving field of low intensity, the atom scatters the light mostly in a coherent manner. Within this regime, the spectral component of this coherent atomic fluorescence mirrors exactly the spectrum of the driving field. As the driving intensity increases, incoherently scattered light starts to appear in the spectrum, while the coherent component will gradually reduce. This manifests as the emergence of a Lorentzian profile with the linewidth of the natural decay rate, and subsequently, the appearance of sidebands in the spectrum.

Quantitatively, the transition between these two regimes is characterized by the saturation parameter $s = 2\Omega^2/\Gamma^2$, where Ω is the Rabi frequency for the driving field and Γ is the natural decay rate of the two-level atom. This is shown in Fig 3.1(a). The total scattering rate is given by the atomic population in the excited state, such

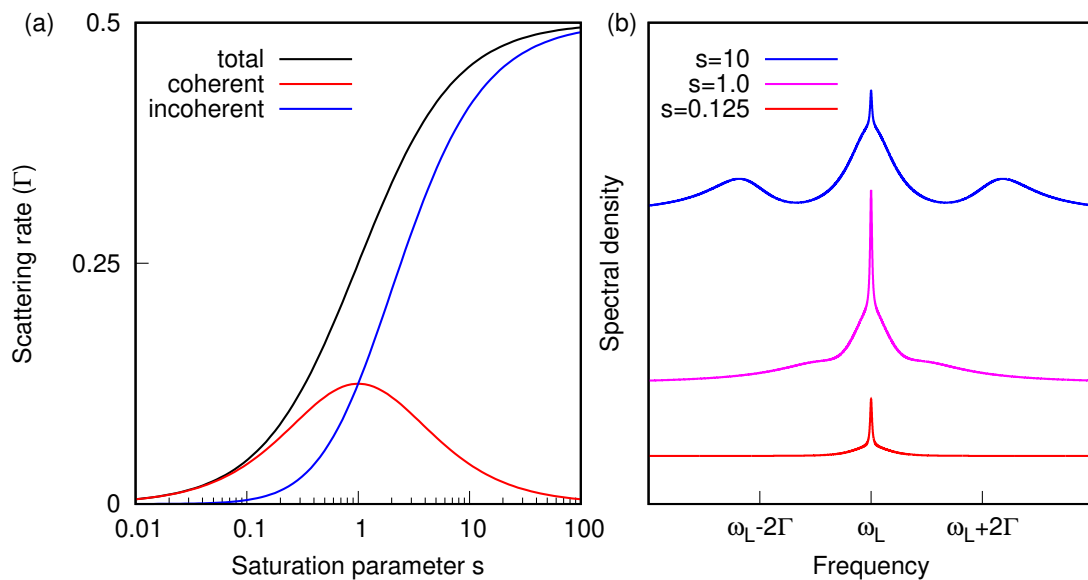


Figure 3.1: (a) Scattering rates for an on-resonance driving field ($\Delta = 0$) as a function of saturation parameter s . (b) Spectral density $S(\omega)$ of the atomic emission at different saturation parameters s . The zero reference lines for various s have been shifted for better visualization.

that

$$R_{\text{sc}} = \Gamma \rho_{ee} = \Gamma \frac{\Omega^2}{2\Omega^2 + 4\Delta^2 + \Gamma^2}, \quad (3.2)$$

and the coherent scattering rate R_{coh} and the incoherent scattering rate R_{incoh} are given by

$$\begin{aligned} R_{\text{coh}} &= \Gamma |\rho_{eg}|^2 = \Gamma \frac{\Omega^2(4\Delta^2 + \Gamma^2)}{(2\Omega^2 + 4\Delta^2 + \Gamma^2)^2}, \\ R_{\text{incoh}} &= R_{\text{sc}} - R_{\text{coh}} = \Gamma \frac{2\Omega^4}{(2\Omega^2 + 4\Delta^2 + \Gamma^2)^2}, \end{aligned} \quad (3.3)$$

where $\rho_{eg} = \Omega(2\Delta + i\Gamma)/(2\Omega^2 + 4\Delta^2 + \Gamma^2)$. The expression for ρ can be obtained by solving for the steady-state solution of the optical Bloch equation:

$$\dot{\rho} = -\frac{i}{\hbar}[\rho, \hat{H}_I] + \Gamma \hat{L}_\sigma(\rho), \quad (3.4)$$

where $\sigma = |g\rangle\langle e|$ is the atomic lowering operator, \hat{L}_σ is the Lindblad superoperator describing the decoherence due to spontaneous decay, and \hat{H}_I is the interaction Hamiltonian representing the coherent interaction with the classical light field:

$$\hat{H}_I = \hbar \frac{\Omega}{2} (\sigma + \sigma^\dagger) - \hbar \Delta \sigma^\dagger \sigma. \quad (3.5)$$

Here, Ω is the Rabi frequency (chosen to be a real number) and $\Delta = \omega_L - \omega_A$ is the laser detuning from the atomic transition.

Spectrum of scattered field

To evaluate the power spectrum of atomic fluorescence, we first have to look at the first-order correlation function of the atomic scattered electric field, $\langle E(t')E^*(t) \rangle$, which is determined by the two-time atomic correlation function $\langle \sigma^\dagger(t)\sigma(t') \rangle$. We can express the power spectral density of the atomic fluorescence $I(\omega, \vec{r})$ as [108]

$$I(\omega, \vec{r}) = \frac{\hbar\omega_0\Gamma}{2\pi} \frac{f_\epsilon(\theta, \phi)}{r^2} \int_{\mathbb{R}} d\tau e^{-i\omega\tau} \langle \sigma^\dagger(t)\sigma(t+\tau) \rangle_t, \quad (3.6)$$

where $f_\epsilon(\theta, \phi)$ represents the angular emission pattern for the dipole polarization ϵ . We can see that $I(\omega, \vec{r})$ is essentially a Fourier transform of the atomic correlation function, which is a result of the Wiener–Khinchin theorem.

In general, $I(\omega, \vec{r})$ does not have a clean analytical expression. Nevertheless, we can approximate the power spectral density with the first few leading orders of s

and $1/(1+s)$ for the two regimes where $s \ll 1$ (weak driving) and $s \gg 1$ (strong driving), respectively. Adapting to the convention where we express $I(\omega, \vec{r}) = \hbar\omega_0\Gamma f_\epsilon(\theta, \phi)S(\omega)/(2\pi r^2)$, where $S(\omega)$ is a normalized spectral density for which $\int S(\omega)d\omega$ is dimensionless, we can have

$$S(\omega) = S_{\text{coh}}(\omega) + S_{\text{incoh}}(\omega). \quad (3.7)$$

Similar to the previous part, $S(\omega)$ can be partitioned into a coherent and an incoherent contribution. For a weak coherent driving field $s \ll 1$, we can write

$$S_{\text{coh}}(\omega) = \frac{s}{(1+s)^2} \delta(\omega - \omega_L), \quad (3.8)$$

$$S_{\text{incoh}}(\omega) = \frac{s}{8\pi(1+s)} \frac{\Gamma}{(\omega - \omega_L)^2 + (\Gamma/2)^2}, \quad (3.9)$$

Here the dominant term is the Dirac delta distribution given in the coherent contribution. For increasing s , the Lorentzian profile with a full-width half maximum (FWHM) of Γ will become more pronounced as the $s/(1+s)^2$ term in the coherent part decays faster than the $s/(1+s)$ part of the incoherent part (see Fig. 3.1(b)).

For a strong coherent driving field, $s \gg 1$, the coherent contribution $S_{\text{coh}}(\omega)$ has the same form as in Eqn. 3.8, but the incoherent contribution takes the following form:

$$\begin{aligned} S_{\text{incoh}}(\omega) = & \frac{s}{8\pi(1+s)} \frac{\Gamma}{(\omega - \omega_L)^2 + (\Gamma/2)^2} \\ & + \frac{s}{32\pi(1+s)^2} \frac{3\Gamma(s-1) + (\Gamma/\Omega)(5s-1)(\omega - \omega_L + \Omega)}{(\omega - \omega_L + \Omega)^2 + (3\Gamma/4)^2} \\ & + \frac{s}{32\pi(1+s)^2} \frac{3\Gamma(s-1) - (\Gamma/\Omega)(5s-1)(\omega - \omega_L - \Omega)}{(\omega - \omega_L - \Omega)^2 + (3\Gamma/4)^2}. \end{aligned} \quad (3.10)$$

Particularly, $S_{\text{incoh}}(\omega)$ has a central resonant Lorentzian peak with a FWHM of Γ as well as two side peaks $\pm\Omega$ away from the resonance, with a FWHM of $3\Gamma/2$. These sidebands, together with the central peak, form the Mollow triplet [69].

3.2 Dressed-state representation

The spectral features can be understood intuitively by adopting the dressed-atom description[70, 109]. We consider the total system consisting of the two-level atom and the laser photons, subject to the Hamiltonian

$$H = \hbar(\omega_L - \Delta)\sigma^\dagger\sigma + \hbar\omega_L a^\dagger a + \hbar\frac{\Omega}{2}(\sigma^\dagger a + \sigma a^\dagger), \quad (3.11)$$

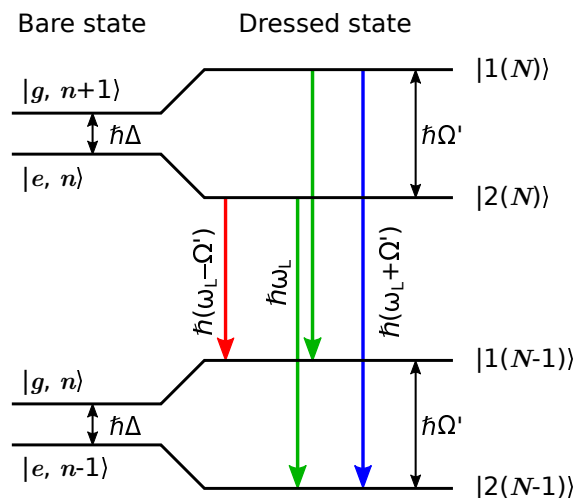


Figure 3.2: Dressed-state picture for an atom coupling to an intense driving field. Bare states are characterized by the photon number Fock state (n) and the atom in the ground (g) or excited (e) state. Their energy difference is $\hbar\Delta$ in the rotating frame, where Δ is detuning of the driving field from atomic resonance. Dressed states are described by a pair of states with a number of total excitations N split by $\hbar\Omega'$ where $\Omega' = \sqrt{\Omega^2 + \Delta^2}$ is the generalized Rabi frequency.

where each term represents the bare atom, laser photon, and atom-light interaction, respectively. The operator a (a^\dagger) is the annihilation (creation) operator for the photon number Fock state $|n\rangle$ from the driving field. By diagonalizing H , the new eigenstates are a superposition of the bare states $|g, n+1\rangle$ and $|e, n\rangle$ (see Fig. 3.2). In every manifold where the total number of excitations N is the same, the eigenstates are split by the generalized Rabi frequency $\Omega' = \sqrt{\Omega^2 + \Delta^2}$. We will focus on the case for on-resonance excitation $\Delta = 0$, which gives $\Omega' = \Omega$.

The three peaks in the fluorescence spectrum can be understood as the spontaneous decay process from the manifold of N total excitations to the manifold with $(N-1)$ excitations. Notably, four optical transitions are possible in this process. Two of them are degenerate (green decays in Fig. 3.2) and correspond to the central peak in the fluorescence spectrum, while the sidebands $\pm\hbar\Omega$ away from the central peak originate from the other two transitions (red and blue decays in Fig. 3.2). This leads to the weighting of $1 : 2 : 1$ in the total spectral intensities of the incoherent peaks under resonant excitation. Note that this picture is most useful when $\Omega \gg \Gamma$ where the dressed states are spectrally resolved.

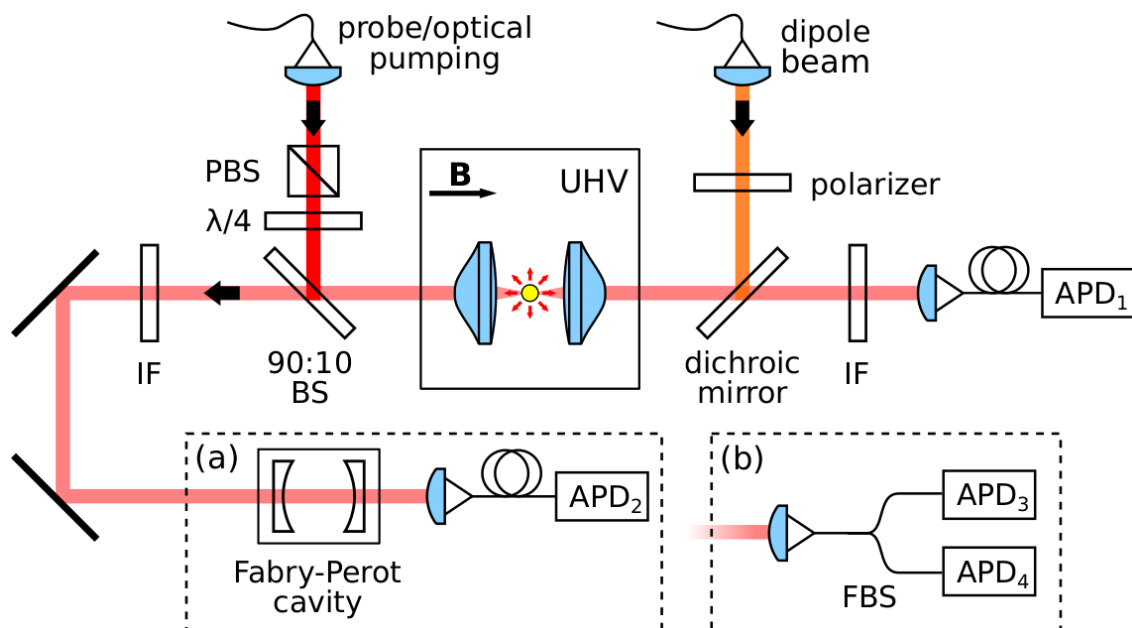


Figure 3.3: Optical setup for collecting atomic fluorescence from a single atom in free space. One avalanche photodiode (APD_1) is used to monitor the atomic fluorescence and acts as a trigger to start the experimental sequence. (a) A Fabry-Perot cavity resolves the frequency spectrum of the atomic fluorescence. (b) Hanbury-Brown and Twiss (HBT) configuration to measure second-order intensity autocorrelation.

3.3 On-resonant excitation

3.3.1 Experimental implementation

The schematic diagram of the experimental setup and the experimental sequence are described in Fig. 3.3 and Fig. 3.4, respectively. Once a single ^{87}Rb atom is trapped in the FORT, we apply PGC for 10 ms to reduce the atomic motion to a temperature of around $13\ \mu\text{K}$ (as described in Section 2.4), corresponding to a Doppler broadening of approximately 110 kHz. A bias magnetic field of 1.44 mT is then applied along the FORT laser propagation direction to remove the degeneracy of the Zeeman states, followed by an optical pumping step that prepares the atom in the $|F = 2, m_F = -2\rangle$ Zeeman sublevel. Next, we turn on the σ^- polarized on-resonant probe laser beam along the optical axis for $2\ \mu\text{s}$. This pulse length is chosen to maximize the duty cycle of photon collection while avoiding excessive

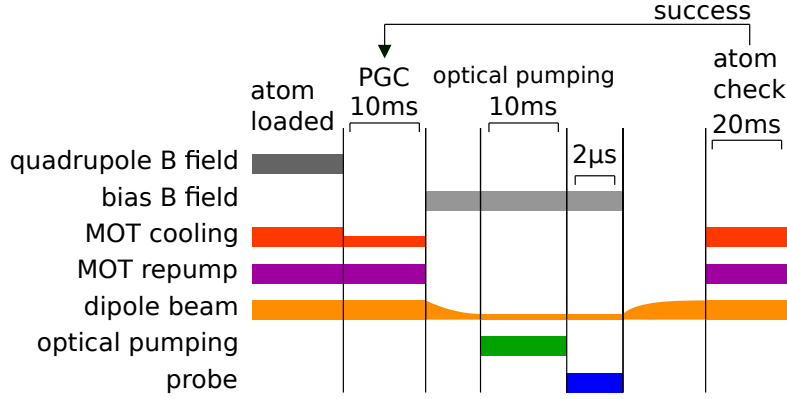


Figure 3.4: Experimental sequence for probing the Mollow triplet. The probe driving field is applied for $2\ \mu\text{s}$, during which the atomic fluorescence is collected.

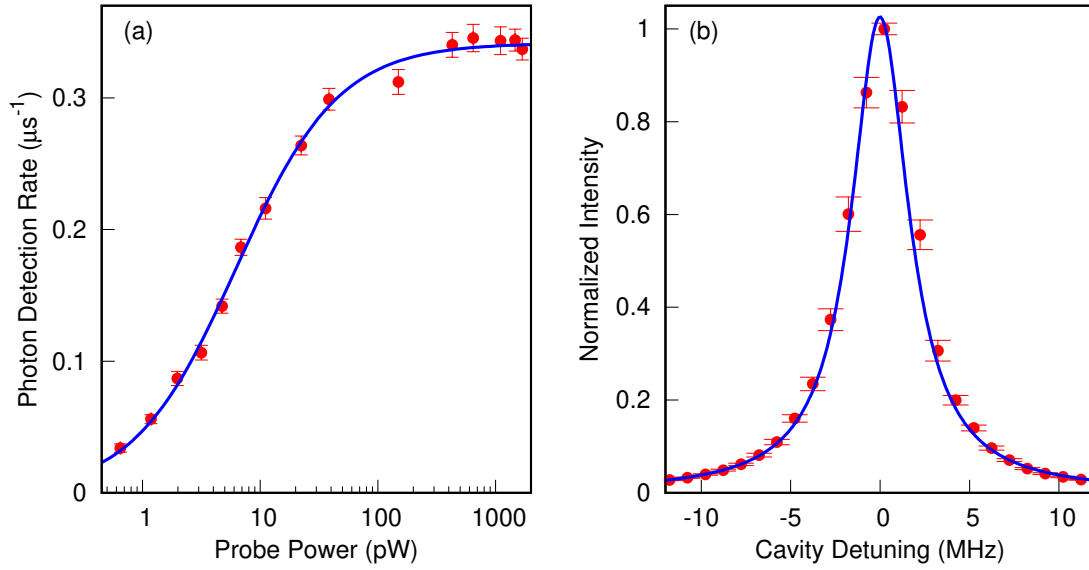


Figure 3.5: (a) Resonant saturation measurement, with the blue solid line representing the fit to the saturation curve $\frac{\eta\Gamma}{2} \frac{P_{\text{probe}}}{P_{\text{probe}} + P_{\text{sat}}}$, where P_{probe} is the incident probe power, P_{sat} is the saturation power, and η is the total detection efficiency. (b) Cavity transmission of the probe laser to characterize the cavity linewidth. The solid line represents a fit to Lorentzian function $\gamma_c^2 / (\gamma_c^2 + 4\Delta^2)$, where γ_c is the cavity linewidth.

recoil heating of the atom (refer to Chapter 3.3.2 for more discussions). During the probing period, we collect photons scattered backward through the same lens into a single-mode fiber-coupled APD, avoiding the strong light levels of the probe laser for analysis. The photon scattering rate is first characterized for different intensity levels of the probe field, as illustrated in Fig 3.5(a). From the fit, we deduce that the atomic scattering saturates at a probe power of 6.3 ± 0.2 pW, and the total detection efficiency is around $\eta = 1.79 \pm 0.02\%$.

After we establish a better understanding of the saturation parameter s for the probe field, we employ a Fabry-Perot cavity to frequency-filter the collected fluorescence photons, as shown in Fig. 3.3(a). By scanning the cavity resonance frequency, the frequency spectrum of the fluorescence can be obtained from the transmission count rates. To precisely control the resonance frequency of this cavity, it is locked to a tunable sideband generated by an electro-optical modulator (EOM) from our 795-nm laser locked to the D_1 transition line of a ^{87}Rb atom. The linewidth of the cavity is characterized to be $\gamma_c/2\pi = 3.92 \pm 0.05$ MHz with an external cavity diode laser (see Fig 3.5(b)). This value will be used for deconvolution of the atomic spectrum in the following sections.

3.3.2 Atom loss due to heating

At the early stage of the experiment, we encountered difficulties in reaching the saturation regime due to underestimation of the heating effect. In the following, we discuss the two mechanisms that are responsible for this issue.

Reduced trap depth due to atomic state

For increasing the Rabi frequency of the driving field Ω , the population for the excited state also increases accordingly. However, since the FORT does not behave as an attractive potential in the excited state, the trapping force experienced by the atom will decrease for a larger Ω .

As the atomic state will undergo Rabi oscillation and vary in time, the trapping potential will also be changing as a function of time. For large saturation parameters ($s \gg 1$), the Rabi frequency of more than tens of MHz is much higher than the trap frequency of the FORT. Therefore, the atomic motion is not able to respond as fast as the oscillation of the atomic state. Consequently, the effective potential as seen

by the center-of-mass motion will be given by the steady-state population of the atom. This is illustrated in Fig. 3.6(a).

Accounting for the repulsive AC Stark shift of the excited state, the average light shift experienced in the atomic steady state is approximately 36.6% of the original trap depth U_g , which in our case is around $k_B \times 0.32$ mK.

Recoil heating

We treat the motion of the atom classically and consider the change in the atomic momentum due to a ballistic collision with a probe photon. Every scattering event is treated as an absorption of the probe photon in the $+z$ direction, followed by a spontaneous decay that obeys the dipole emission pattern. Assuming a Maxwell-Boltzmann distribution, the probability distribution for the atomic momentum $P(p_x, p_y, p_z)$ can then be expressed as

$$P(p_x, p_y, p_z) \propto \exp\left(-\frac{p_x^2 + p_y^2}{2mk_B T_0 + 0.3N\hbar^2 k^2} - \frac{(p_z - N\hbar k)^2}{2mk_B T_0 + 0.4N\hbar^2 k^2}\right), \quad (3.12)$$

where N is the number of scattering events, $\hbar k$ the momentum of 780-nm photon, m the mass of a ^{87}Rb atom, k_B the Boltzmann constant, and T_0 is the initial atomic temperature. Notably, the mean value for p_z follows $N\hbar k$ as the probe beam pushes the atom in the same $+z$ direction constantly. Also, the variance for p_x, p_y , and p_z increases linearly with $N\hbar^2 k^2$, with different coefficients. This is because the dipole scattering pattern is anisotropic. For a circularly polarized dipole, the angular emission profile follows $(3/8\pi)(1 - (\sin^2 \theta)/2)$ [110], where θ is the polar angle in the spherical coordinate.

With this expression, we can evaluate the probability of an atom possessing kinetic energy $E_k = (p_x^2 + p_y^2 + p_z^2)/2m > U_0$ numerically, as shown in Fig. 3.6(b). For an atom in the trapping potential of $k_B \times 0.86$ mK ($k_B \times 0.32$ mK), it takes about 70 (45) scattering events for the atom to gain a kinetic energy comparable to U_0 . With a strong driving field that is far in the saturation regime ($s \gg 1$), we can assume the scattering rate is approximately $\Gamma/2$. This allows us to establish the characteristic heating time $\tau_{\text{heat}} = 2\sqrt{U_0/(\Gamma^2 E_r)}$, which corresponds to a probing duration of $3.7 \mu\text{s}$ ($2.4 \mu\text{s}$) for $U_0/k_B = 0.86$ mK (0.32 mK). Therefore, in the experiment, we choose a probing period of $2 \mu\text{s}$, which is shorter than τ_{heat} to avoid excessive recoil heating of the atom.

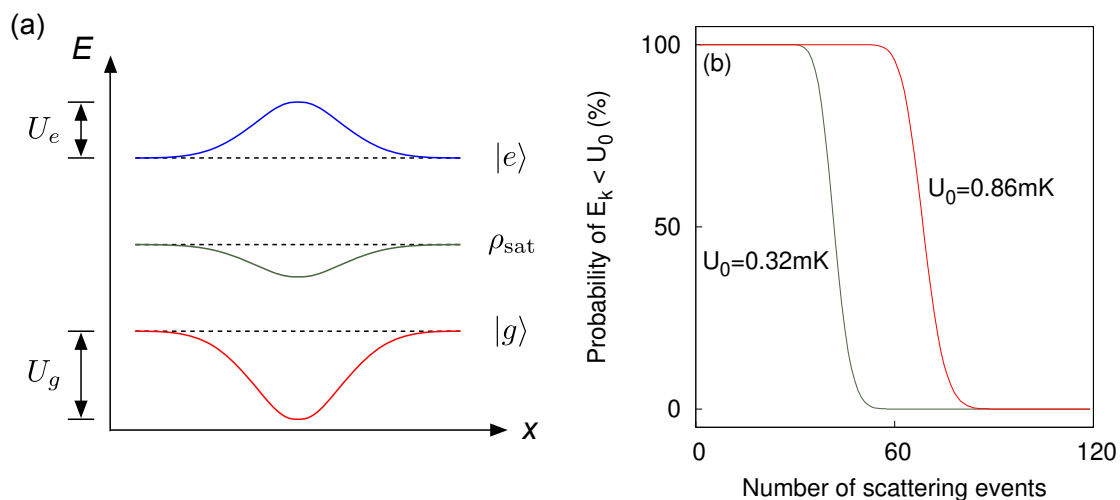


Figure 3.6: (a) Schematic diagram for the trapping profile for different atomic levels. (b) Numerical result of the probability for an atom to remain $E_k < U_0$ after photon scatterings.

3.3.3 Discussion

Measured spectrum of the atomic fluorescence

We record the frequency spectra for increasing excitation powers, as shown in Fig. 3.7. Here, we normalize the spectra with the maximum peak intensity for better visualization. At weak excitation, the FWHM of the single peak in Fig. 3.7(a) is 2.5(3) MHz after deconvolution from the cavity contribution. The deconvolution is performed numerically by convoluting the cavity transfer function $\gamma_c^2/(\gamma_c^2 + 4\omega^2)$ with the fit equations $S(\omega)$ described in Eqn. 3.8, 3.9, and 3.10. The observation is in agreement with the premise that the coherent scattering component with a linewidth smaller than Γ dominates the spectrum for a driving power that is well below saturation.

As the power increases, the three-peak structure emerges and the splitting between the peaks also increases. After excluding cavity contribution, the central peak in Figs. 3.7(d) and (e) have a FWHM of around 8 MHz extracted from the fit. This value is close to the atomic natural linewidth of ^{87}Rb , thus justifying the claim that an optically trapped single atom can be laser cooled to mitigate the Doppler broadening effect.

As discussed in the theoretical section, we expect the height ratio between the

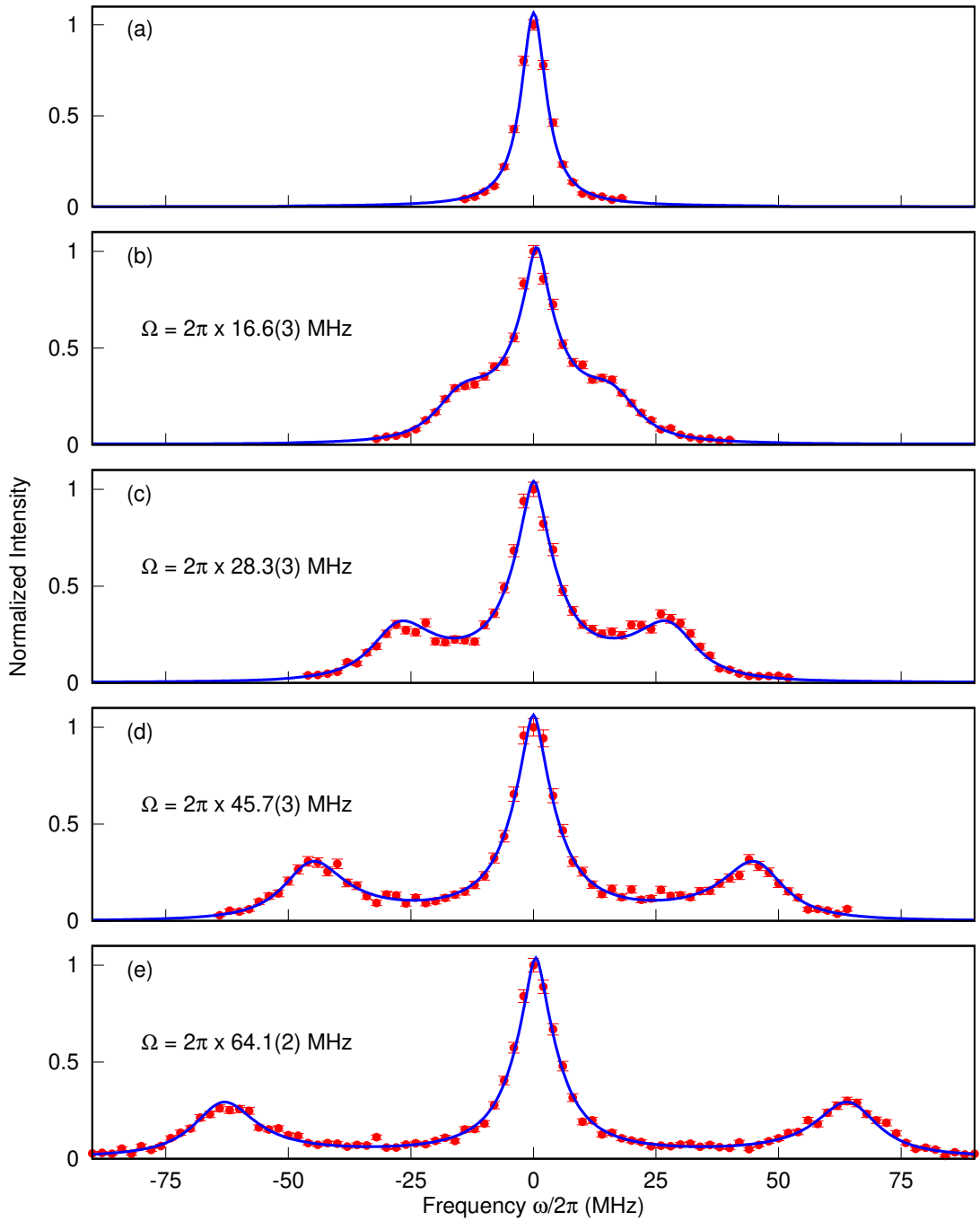


Figure 3.7: Normalized resonance atomic emission spectra at different excitation intensities recorded by scanning the Fabry-Perot cavity. The solid line is a fit to $S(\omega)$ convoluted with the cavity transfer function and the effect of laser reflection. The Rabi frequency extracted from the fit is labeled in the respective subplots. Error bars represent the standard error of the mean determined from around 20,000 repeated experimental sequences.

central peak and the sidebands to be around 1 : 3 : 1 according to Eqn. 3.10 as the sidebands have a larger width compared to the central peak. Accounting for the linewidth of the filtering cavity, the height of the central peak should decrease such that the ratio reaches around 1 : 2.6 : 1. However, the measured spectra show central peaks with about 3.7 times the height of sidebands, averaged over Figs. 3.7(c) to (e). This inconsistency between the theoretical prediction and the experimental data can be likely attributed to the reflection and scattering of the probe laser from the optics. By introducing this laser component in our model, we deduced a contribution of 0.9 %, 2.4 %, and 4.5 % of the total power in the spectra in Figs. 3.7(c) to (e), respectively.

Second-order correlation

Next, we are interested to see if the Mollow splitting measured is consistent with the Rabi frequency driving the two-level system. In this part of the experiment, we replace the Fabry-Perot cavity with a fiber beam splitter and two APDs in a Hanbury-Brown and Twiss configuration as shown in Fig. 3.3(b) to perform an intensity correlation measurement. We refer to the arrival times of the fluorescence photons on the two APDs as t_1 and t_2 , respectively. The differences of detection times $\tau = t_2 - t_1$ of a pair of photodetection events are then recorded on a time-tagging device for the construction of a histogram for τ . Given that τ is smaller than the reciprocal of the mean photodetection rate, we can assume the intensity at time t follows $I(t) \approx \mathbb{P}(t)/\Delta_t$, where $\mathbb{P}(t)$ is the probability of detecting a photon for the time bin t and Δ_t is the time bin width. Therefore, the second-order intensity correlation function $g^{(2)}(\tau)$ of the atomic fluorescence can be inferred from $\langle \mathbb{P}(t_2 = t_1 + \tau | t_1) \rangle_{t_1}$.

This correlation function can reveal some characteristics of the photons emitted by a single atom such as photon antibunching at $\tau = 0$ and Rabi flopping dynamics for $|\tau| < 1/\Gamma$. For driving fields of low intensity, $g^{(2)}(\tau)$ shows a monotonic increase to unity as τ increases from zero to much larger than $1/\Gamma$. When the driving field intensity increases above saturation, $g^{(2)}(\tau)$ resembles the case for weak excitations at a large delay, but oscillations corresponding to the Rabi frequency appear around zero delays. Upon detection of the first fluorescence photon, the atom is projected onto the ground state and the probability of detecting the subsequent photon at

some later time τ is proportional to the excited state population of the atom. This correlation function for fluorescence from a single atom can be expressed as [111]

$$g^{(2)}(\tau) = 1 - e^{-(3\Gamma/4)|\tau|} \left(\cos(\Omega\tau) + \frac{3\Gamma}{4\Omega} \sin \Omega|\tau| \right). \quad (3.13)$$

As shown in Fig. 3.8, we record a series of second-order intensity correlation measurements for the same excitation power used in spectrum measurement. The correlation measurements are fitted to Eqn. 3.13, multiplied with a triangle function that results from a convolution of two square pulses of the same length. This is done to account for the fluorescence from each detector being collected during a 2- μ s-wide time window. In fact, the time window effect will result in a 4- μ s-wide triangular envelope being applied to the correlation measurement. We can deduce the corresponding Rabi frequencies from the fit so that these measurements can serve as an alternative approach allowing comparison to the values obtained from the Mollow triplet spectral measurement. The extracted values, labeled in Fig. 3.8 for increasing driving powers, are in good agreement with the values of Ω obtained from the Mollow triplet spectra.

3.4 Off-resonant excitation

While the atom is excited resonantly, the emission of the sideband photons does not have a preferred order. As such, the cross-correlation between photons from different sidebands is symmetric with respect to zero time delay $\tau = 0$. However, if the excitation field is detuned from the atomic resonance, this symmetry is broken as the emission process of the sideband photons now has a preferred order [70, 112, 113]. The preferred order of the emission depends on the sign of the detuning and manifests as an asymmetry in the correlation measurement around $\tau = 0$.

3.4.1 Correlation between two sideband photons

In this part of the experiment, we red-detuned the excitation laser by 30 MHz from the atomic resonance. As shown in Fig. 3.9, there is a Fabry-Perot cavity in front of each APD to filter the incoming fluorescence such that photon correlation between chosen spectral components can be measured. To better transmit the

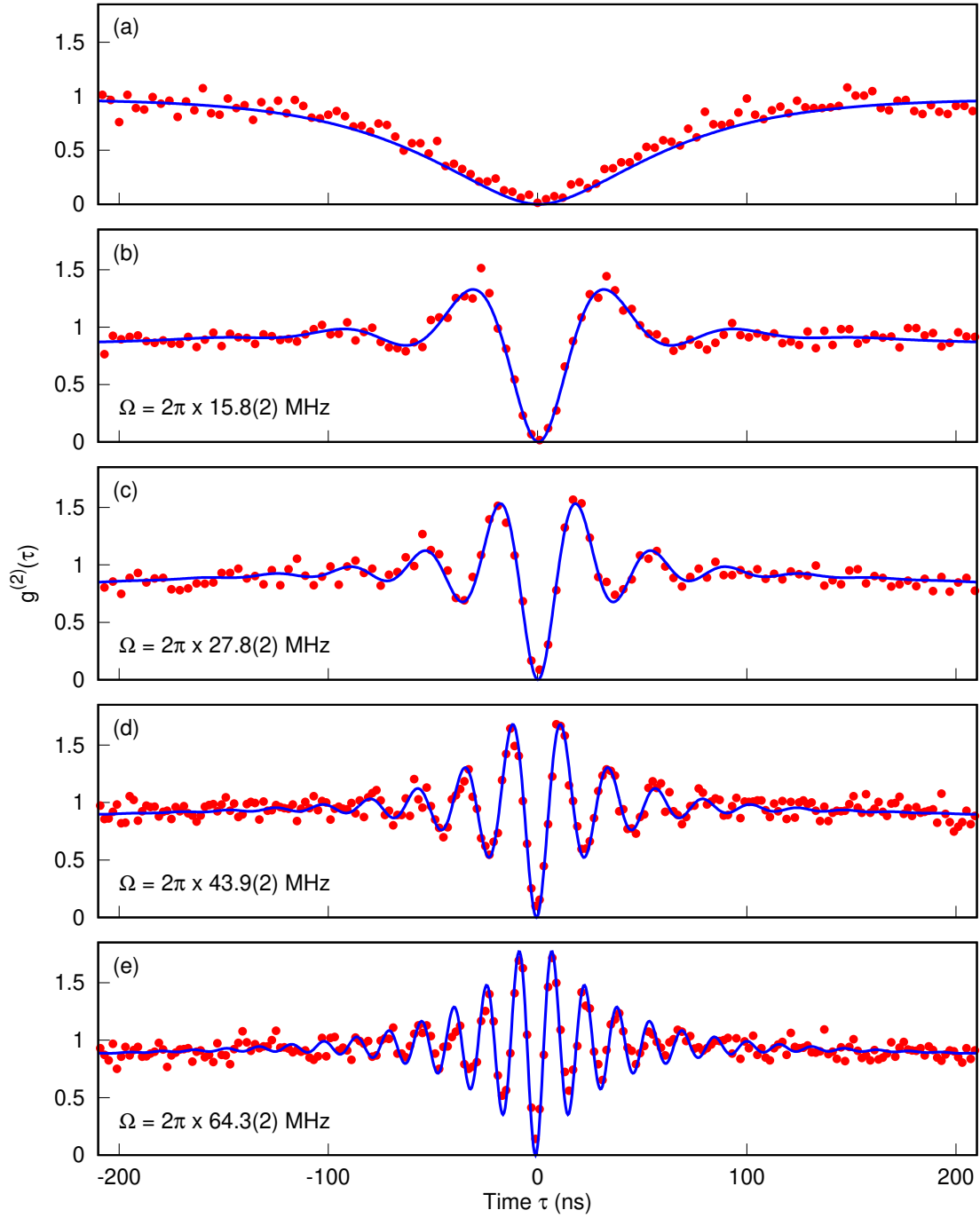


Figure 3.8: Second-order correlation function of the single atom for increasing excitation intensities. The solid line is a fit to Eqn. 3.13 accounting for a triangle function resulting from the convolution of two square pulses. The Rabi frequency shown for each spectrum is deduced from the respective fit.

photons from different peaks, we replace the cavities used in this experiment to have a linewidth of 20 MHz.

The spectrum of the fluorescence is slightly different when the atom is excited off-resonantly, with the central peak sitting at the driving frequency and the sideband separated from the central peak by the generalized Rabi frequency $\Omega' = \sqrt{\Omega^2 + \Delta^2}$, where Δ is the detuning of the laser from atomic resonance. The power ratio between the central peak and the sidebands deviates from the on-resonance case, with the central peak being suppressed as detuning increases. To align the cavity resonance with the respective sidebands, we first measure the second-order correlation of the off-resonance fluorescence. The data are shown in the inset of Fig. 3.10 and the blue

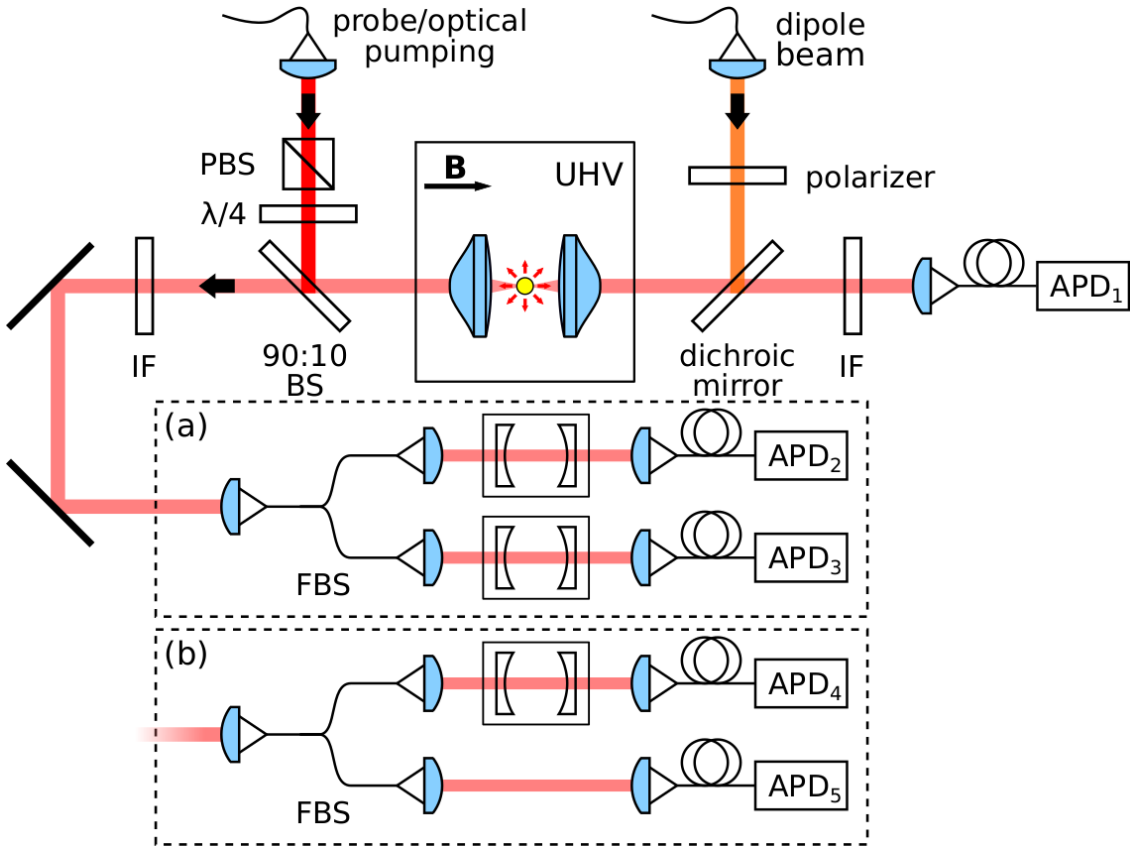


Figure 3.9: Optical setup for collecting atomic fluorescence from a single atom in free space for $g^{(2)}$ measurements, similar to the previous part. (a) Cross-correlation measurement setup with a cavity in each arm before APD₂ and APD₃ to select photons from a specific frequency window. (b) Cross-correlation measurement setup with only one filtering cavity in one of the two arms.

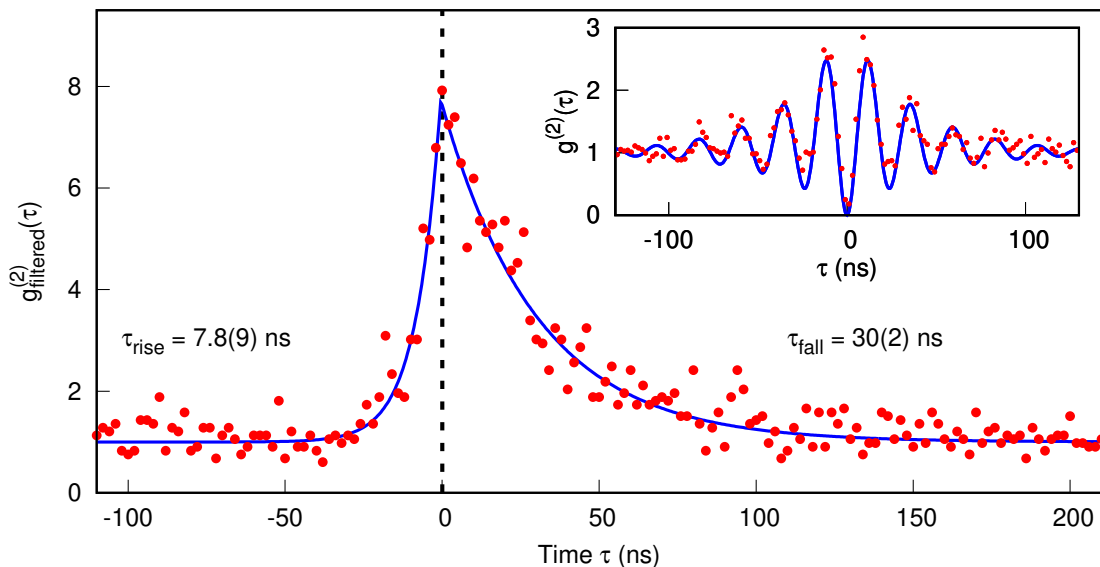


Figure 3.10: Normalized cross-correlation between photons from two opposite Mollow sidebands as a function of delay τ between detection of a blue sideband photon after detecting a red sideband photon. Inset: Normalized intensity autocorrelation of the unfiltered off-resonance atomic fluorescence to extract the generalized Rabi frequency Ω' .

solid line is the fit to extract Ω' , which is $2\pi \times 42 \pm 1$ MHz in this case. As such, the cavity resonance is locked at $\pm\Omega'$ away from the driving frequency to isolate the sideband photon.

Figure 3.10 shows the cross-correlation measurement between the opposite Mollow sidebands where we use a photon from the lower-energy sideband as the “start” trigger and the photon from the other sideband as the “stop” signal. The measurement shows a clear bunching behavior around $\tau = 0$. We normalize the correlation function with respect to coincidence counts from a time window that is far from $\tau = 0$. With this, we obtain a bunching value of 8.1 ± 0.8 . Applying Eqn. (40) from reference [70], the theoretically predicted bunching value is approximately 11 for the parameters in our experiment. The discrepancy to our observed value of 8.1 could be attributed to the imperfect spectral filtering. With the separation of 42 ± 1 MHz, cavities with a linewidth of 20 MHz cannot suppress the photons from the central peak and the opposite sideband entirely. Therefore, there are some correlation contributions from different combinations of photons in our experiment, for example, between photons

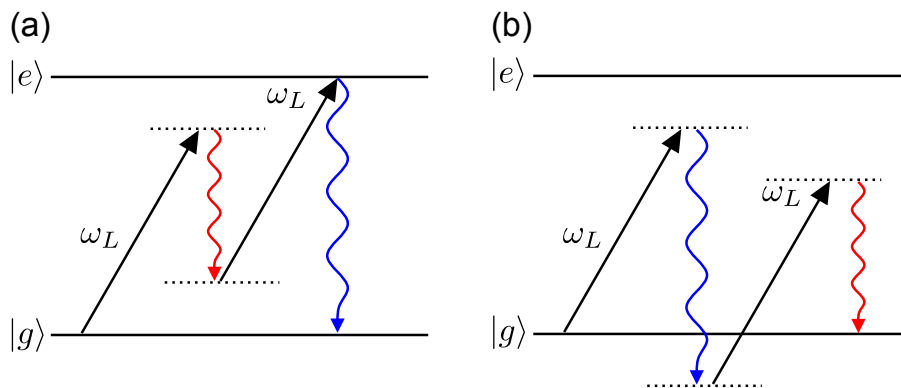


Figure 3.11: Two possible multiphoton scattering processes. (a) Emission of a red sideband photon followed by a blue sideband photon. (b) Emission of a blue sideband photon followed by a red sideband photon. Scattering process (b) is less likely to occur because it involves more virtual levels.

from the central peak and photons from two sidebands. These would reduce the expected bunching value.

Asymmetrical temporal correlation

By performing fits to exponential functions on the rising and decaying edges of the normalized correlation, we obtain time constants of $\tau_{\text{rise}} = 7.8 \pm 0.9$ ns and $\tau_{\text{fall}} = 30 \pm 2$ ns, respectively. As a comparison, the corresponding theoretical prediction following the model in [70] for τ_{rise} and τ_{fall} are 7.96 ns and 35.02 ns. The asymmetry of the correlation function indicates that the emission of the sideband photons has a preferred time order for off-resonant excitation, in this case first an emission from the lower-energy sideband, followed by a second emission from the higher-energy sideband.

To explain this observation, one can look at multiphoton scattering processes [112] involving the absorption of two laser photons and the emission of two fluorescence photons having frequencies $\omega_L \pm \Omega'$, as illustrated in Fig. 3.11. In Fig 3.11(a), we can see that there is an intermediate resonance when the atom arrives at the excited state $|e\rangle$ after the absorption of the second laser photon. Here, the ordering is important because the emission process in the reverse order (see Fig. 3.11(b)) involves an additional virtual state to occur. Hence, the reverse process proceeds at a much smaller rate.

The dressed-state picture also offers an alternative explanation for the correlation

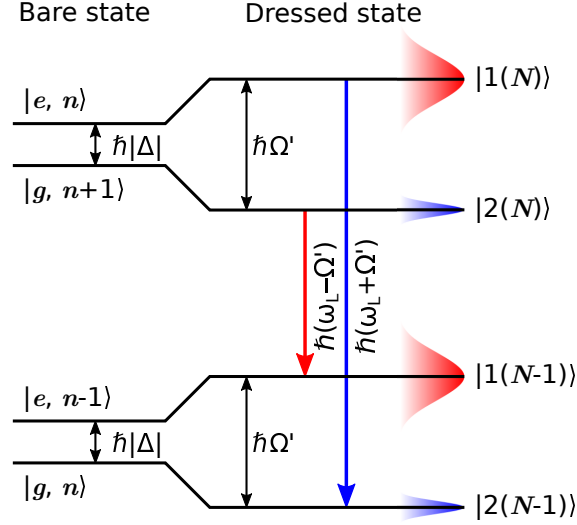


Figure 3.12: Dressed-state picture for an atom coupling to an off-resonant driving field. Bare states are characterized by the photon number Fock state (n) and the atom in the ground (g) or excited (e) state. Their energy difference is $\hbar\Delta$ in the rotating frame, where Δ is the detuning of the driving field from atomic resonance. Dressed states are described by a pair of states with a number of total excitations N split by $\hbar\Omega'$ where $\Omega' = \sqrt{\Omega^2 + \Delta^2}$ is the generalized Rabi frequency.

asymmetry. In contrast to the on-resonance scenario, the new eigenstates accounting for the off-resonant driving do not have the same population distribution in the excited state $|\langle e, n|1(N)\rangle|^2$ and $|\langle e, n|2(N)\rangle|^2$. This leads to significantly distinct energy widths for the eigenstates, as highlighted in Fig. 3.12. Thanks to the frequency selectivity of optical cavities, we can restrict ourselves to only look at the emissions of the two sideband photons $\omega_L \pm \Omega' \approx \omega_L \pm \Delta$ for large detuning $\Delta \gg \Omega$. The eigenstate $|1(N)\rangle$ then consists mostly of the excited state $|e, n\rangle$ and the eigenstate $|2(N)\rangle$ consists mostly of the ground state $|g, n+1\rangle$. As such, the energy width of $|1(N)\rangle$ will be much closer to Γ , and hence much larger than the energy width of $|2(N)\rangle$. Now we consider a two-photon detection scheme, where the transition $|1(N)\rangle \rightarrow |2(N-1)\rangle$ emits a blue sideband photon while the transition $|2(N)\rangle \rightarrow |1(N-1)\rangle$ emits a red sideband photon. The detection of a red sideband photon as a trigger implies that the atom is now projected to the $|1(N)\rangle$ state. Since the state $|1(N)\rangle$ has a large energy width, from the uncertainty principle we expect that the radiative decay occurs very quickly, leading to the high coincidence rate of observing a blue sideband photon after a red sideband photon. On the other

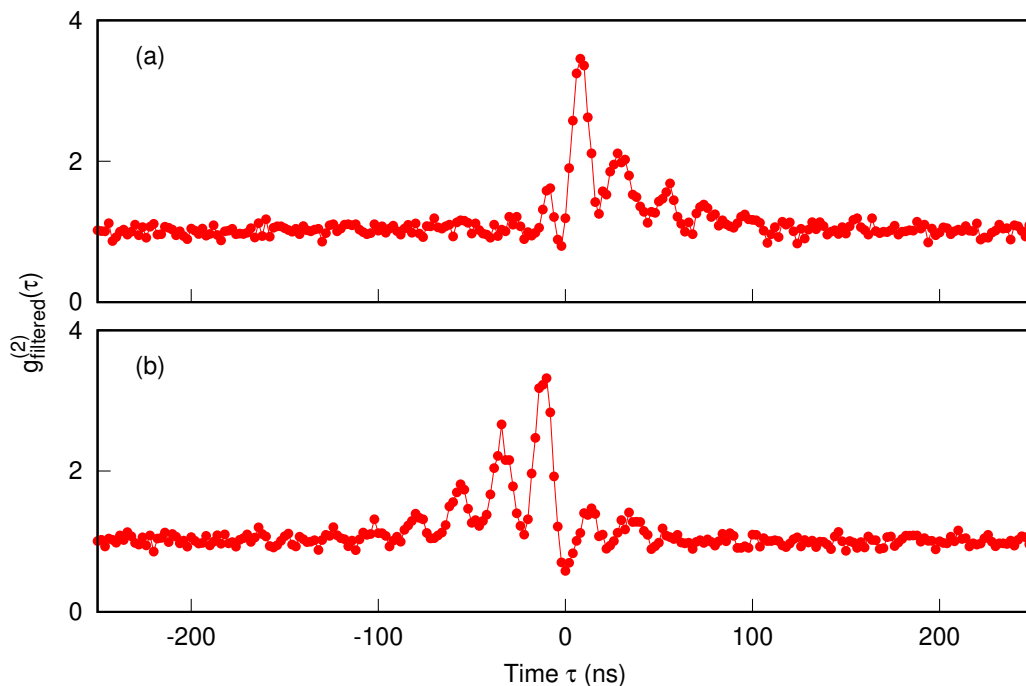


Figure 3.13: Normalized cross-correlation between photon projected to the Mollow sideband and unfiltered photon as a function of delay τ , with $\tau = t_{\text{unfiltered}} - t_{\text{sideband}}$. (a) Red Mollow sideband $\omega_L - \Omega'$ is transmitted. (b) Blue Mollow sideband $\omega_L + \Omega'$ is transmitted.

hand, the detection of a blue sideband photon as a trigger implies that the atom is now projected to the $|2(N)\rangle$ state. It is very unlikely to record a red sideband photon within $1/\Gamma$ as the state $|2(N)\rangle$ has a much narrower energy width and thus corresponds to a smaller decay rate.

3.4.2 Correlation with single-sided filtering

As a supplementary measurement, we also look at the cross-correlation between a filtered sideband photon and the unfiltered arm (see Fig. 3.9(b)). For this measurement, the excitation light is red-detuned by 46 MHz relative to the atomic transition, and the filtering cavity employed has a slightly broader FWHM of $\gamma_c/2\pi = 38$ MHz. The cavity resonance is set to be centered at either the red sideband or the blue sideband of the fluorescence spectrum. Next, we use the photon transmitted through the cavity (sideband photon) as the “start” trigger and the

unfiltered photon as the “stop” signal.

The result is shown in Fig. 3.13, where the subplot (a) takes the red sideband photon as the trigger, and (b) takes the blue sideband photon as the trigger. We observe that the temporal asymmetry is still very pronounced, such that in (a) most pair detections occur after the red sideband photon, and in (b) most pair detections occur before the blue sideband photon. The ordering, governed by the sign of the detuning, is also in agreement with the measurements in the previous part. In particular, we observe an oscillatory feature (with a period of $1/\Omega'$) in both subplots that do not exist in the cross-correlation between opposite Mollow sideband photons. The oscillatory feature is due to the interference with the photons generated from the Mollow central peak, which was filtered out by the optical cavities previously. Since the Mollow central peak can arise from the $|1(N)\rangle \rightarrow |1(N-1)\rangle$ and $|2(N)\rangle \rightarrow |2(N-1)\rangle$ transitions, it does not exhibit a preferable time ordering relative to the sideband photons. Consequently, this results in oscillations occurring for both $\tau < 0$ and $\tau > 0$.

3.5 Summary

In this experiment, we measured the frequency spectra of the resonance fluorescence of an optically trapped atom at different excitation intensities. The signature Mollow triplet was observed and compared to the theoretical model. The measurement results agree well with the theoretical prediction after taking into account the effect of the cavity transfer function and laser reflections. We then compare the Rabi frequencies obtained from the spacing between Mollow sidebands with the second-order correlation function of the atomic fluorescence $g^{(2)}(\tau)$. The extracted Rabi frequencies from $g^{(2)}(\tau)$ are also consistent with the Mollow spectra. In a different setting, we confirm that the photons from opposite sidebands have a preferred order of emission which is reflected in the asymmetry of the temporal correlation function with an off-resonant excitation. Such a preferred time ordering of the emitted photons from opposite sidebands could be used in a heralded narrowband single-photon source that can find potential applications in quantum networks using atoms or atom-like systems as stationary nodes.

Chapter 4

Ground state coherence

In this chapter, we demonstrate the preparation and measurement of the coherence between the Zeeman sublevels $|F = 2, m_F = -2\rangle$ and $|F = 1, m_F = -1\rangle$ in the $5^2S_{1/2}$ manifold of a single ^{87}Rb atom. This is accomplished using an on-resonant microwave field that couples the two Zeeman sublevels via a magnetic dipole transition. By implementing various dynamical decoupling schemes in our atomic qubit system, we manage to extend the qubit coherence time to approximately 7 ms, which can be useful for the high-fidelity transfer of quantum states between stationary atomic qubits separated by long distances [114].

4.1 Motivation

For future quantum information applications such as a distributed quantum network, entanglement between material qubits and photons is crucial to function as the interface between atomic quantum memories and photonic quantum communication channels, allowing for the distribution of quantum information over long distances. To achieve this objective, multiple proposals have been put forward [114–117]. In particular, we will focus here on one such scheme [118] that is suitable for the generation of time-bin atom–photon entanglement and the sequential generation of an entangled photonic string, such as the Greenberger–Horne–Zeilinger (GHZ) state [119].

The proposed scheme relies on a relatively simple two-level system ($|\uparrow\rangle$ and $|\downarrow\rangle$) with one of the energy eigenstate coupled to a cycling optical transition ($|\uparrow\rangle \leftrightarrow |e\rangle$) to facilitate state readout and entangled photon generation, as shown in Fig. 4.1(a). The experimental sequence is described as follows:

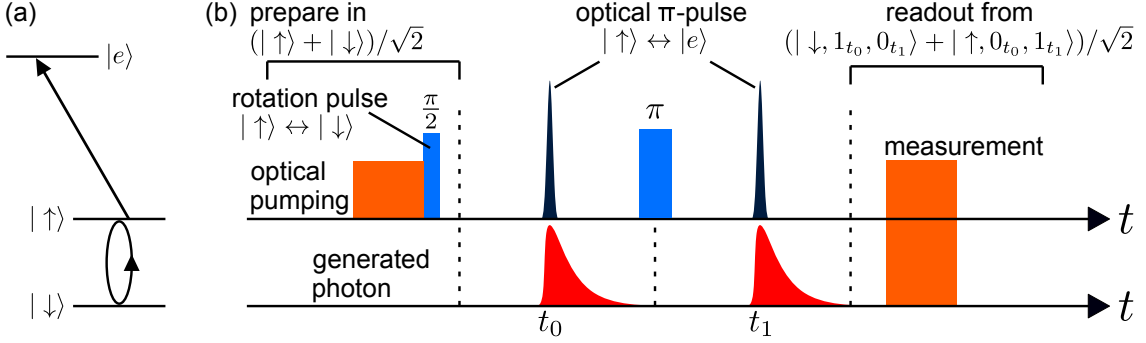


Figure 4.1: (a) Energy level scheme described in [118] to create atom-photon and photon-photon entanglement. (b) Experimental sequence described in the proposal. The two-level system is prepared in the superposition state $(|\uparrow\rangle + |\downarrow\rangle)/\sqrt{2}$ before being driven by an excitation pulse that couples $|\uparrow\rangle$ and $|e\rangle$ states to generate a photon in time-bin t_0 conditional on the qubit state. After a rotation in the qubit state, the same excitation pulse drives the system to generate another photon in time-bin t_1 conditional on the qubit state. Ideally, the atomic qubit and the photonic time-bin qubit can be represented as a Bell state.

1. Initialize the qubit in the superposition state $\frac{1}{\sqrt{2}}(|\uparrow\rangle + |\downarrow\rangle)$.
2. Resonantly drive the optical transition with a π -pulse to generate a photon in the first time-bin (t_0) conditional on the atom being in the $|\uparrow\rangle$ state, yielding $\frac{1}{\sqrt{2}}(|\uparrow, 1_{t_0}\rangle + |\downarrow, 0_{t_0}\rangle)$.
3. Flip the qubit to have $\frac{1}{\sqrt{2}}(|\downarrow, 1_{t_0}\rangle + |\uparrow, 0_{t_0}\rangle)$.
4. Resonantly drive the optical transition with a π -pulse to generate a photon in the second time-bin (t_1) conditional on the atom being in the $|\uparrow\rangle$ state, yielding $\frac{1}{\sqrt{2}}(|\downarrow, 1_{t_0}, 0_{t_1}\rangle + |\uparrow, 0_{t_0}, 1_{t_1}\rangle)$.
5. Flip the qubit again to have $\frac{1}{\sqrt{2}}(|\uparrow, 1_{t_0}, 0_{t_1}\rangle + |\downarrow, 0_{t_0}, 1_{t_1}\rangle)$.
6. Repeat steps (2) to (5) to build up the desired photonic state. By rewriting the photonic qubit in the basis of odd ($|0'\rangle$, following $|0'_{kl}\rangle = |1_{t_k}, 0_{t_l}\rangle$) and even-numbered time-bins ($|1'\rangle$, following $|1'_{kl}\rangle = |0_{t_k}, 1_{t_l}\rangle$), we can have $\frac{1}{\sqrt{2}}(|\uparrow, 0'_{01}, 0'_{23}, 0'_{45}\rangle + |\downarrow, 1'_{01}, 1'_{23}, 1'_{45}\rangle)$ after three iterations.

A schematic diagram for the procedure is also shown in Fig. 4.1(b). By projecting the qubit system to the state $|+\rangle = (|\uparrow\rangle + |\downarrow\rangle)/\sqrt{2}$ at the end of the photon generation process, we can create the three-photon GHZ state $(|0'_{01}, 0'_{23}, 0'_{45}\rangle + |1'_{01}, 1'_{23}, 1'_{45}\rangle)/\sqrt{2}$.

The scheme above assumes the single photon emission from the atom into a single optical mode, which is not really the case in the free space. Particularly, the free-space atom-light interface will have a finite coupling efficiency. Therefore, the generation of an entangled state between atoms and photons typically requires additional post-processing conditioning on the detection of the generated photons, which results in longer experimental runtime.

The quantum states required for this relatively simple scheme can actually be mapped to the energy levels of a ^{87}Rb atom. For instance, the cycling optical transition used in the previous chapter ($5^2\text{S}_{1/2}$, $F = 2$, $m_F = -2 \leftrightarrow 5^2\text{P}_{3/2}$, $F' = 3$, $m_{F'} = -3$) can be exploited for the generation of entangled photons. Consequently, we can use the Zeeman sublevels in the $5^2\text{S}_{1/2}$ ground state manifold, $|\uparrow\rangle \equiv |F = 2, m_F = -2\rangle$ and $|\downarrow\rangle \equiv |F = 1, m_F = -1\rangle$ as the qubit basis. In the subsequent sections of this chapter, we will experimentally study the coherent manipulation of these two Zeeman sublevels.

4.2 Rabi flopping

We consider the two-level system formed by the two Zeeman sublevels in the $5^2\text{S}_{1/2}$ ground state manifold, with an energy spacing given by the hyperfine splitting of approximately $h \times 6.83$ GHz. We use an on-resonant microwave field to probe this transition between two hyperfine levels. Since there is no change in the azimuthal quantum number L , it is an electric dipole forbidden. As such, the coupling between $|\uparrow\rangle$ and $|\downarrow\rangle$ is in fact induced by a magnetic dipole in the microwave domain.

This transition can be described by the Breit-Rabi Hamiltonian $\hat{H}_\mu = \mu_B \mathbf{B}(t) \cdot (g_J \hat{\mathbf{J}} + g_I \hat{\mathbf{I}})$ [120], where μ_B is the Bohr magneton, g_J (g_I) the fine structure (nuclear) g -factor, $\hat{\mathbf{J}}$ ($\hat{\mathbf{I}}$) the operator for total electron angular momentum (total nuclear angular momentum), and $\mathbf{B}(t)$ is the magnetic driving field. Since $g_I \ll g_J$, the Hamiltonian term is often simplified to contain only the $\hat{\mathbf{J}}$ contribution. Restricting the Hilbert space to contain only $|\uparrow\rangle$ and $|\downarrow\rangle$, we can finally write the interaction Hamiltonian for a two-level system under rotating wave approximation:

$$\hat{H} = -\hbar\Delta |\uparrow\rangle\langle\uparrow| + \hbar\frac{\Omega}{2}(|\uparrow\rangle\langle\downarrow| + |\downarrow\rangle\langle\uparrow|), \quad (4.1)$$

where $\Delta = \omega_\mu - \omega_{\text{HFS}}$ the detuning of microwave frequency from the hyperfine

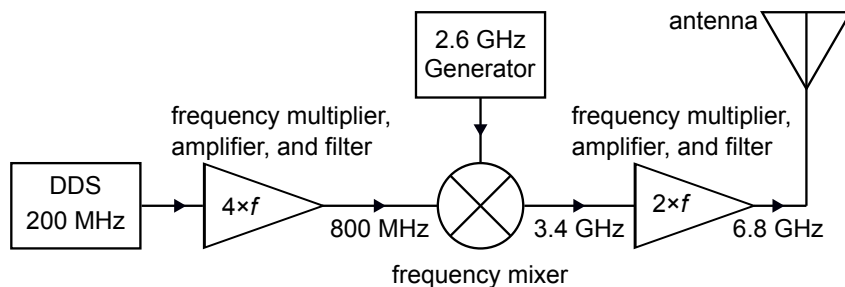


Figure 4.2: Schematic diagram for the generation of a microwave signal at approximately 6.8 GHz to resonantly drive the transition between $|F = 2, m_F = -2\rangle$ and $|F = 1, m_F = -1\rangle$.

splitting and $\Omega = -\sqrt{3}\mu_B B_0/(\sqrt{4}\hbar)$ is the Rabi frequency corresponding to the magnetic field strength B_0 , calculated from the related transition matrix. From the radiative power of an electromagnetic wave $P = AcB_0^2/(2\mu_0)$, where A represents the cross-section of irradiation, c the speed of light, and μ_0 the vacuum permeability, we can estimate that a Rabi frequency of $\Omega = 2\pi \times 50$ kHz necessitates an input power P of approximately 1.9 W for $A = (3/2\pi)\lambda^2 \approx 9.9$ cm².

By solving the Hamiltonian in Eqn. 4.1, we can write the probability of finding the atom in state $|\uparrow\rangle$ as

$$P_{\uparrow}(t) = 1 - \frac{\Omega^2}{\Omega^2 + \Delta^2} \sin^2\left(\frac{\sqrt{\Omega^2 + \Delta^2}}{2}t\right), \quad (4.2)$$

assuming the atom is prepared in the $|\uparrow\rangle$ state at $t = 0$. At resonance ($\Delta = 0$), the atom can deterministically go from $|\uparrow\rangle$ to $|\downarrow\rangle$ with a pulse duration of $t = \pi/\Omega$. This is called a π pulse. On the other hand, with a pulse duration of $t = \pi/(2\Omega)$, we can drive $|\uparrow\rangle$ to a superposition state $(|\uparrow\rangle + i|\downarrow\rangle)/\sqrt{2}$. This is called a $\pi/2$ pulse.

Microwave system

A simplified circuit diagram for the generation of microwave signal is shown in Fig. 4.2. We start with a homemade direct digital synthesizer (DDS) that allows for simple interfacing with the pattern generator that controls the experimental sequences to do frequency, amplitude, and phase modulations. From this DDS output frequency of around 200 MHz, we employ frequency multipliers followed by bandpass filters to derive a signal of 800 MHz. Then, a mixer combines the DDS signal and the output of a commercial radiofrequency signal generator (Stanford Research Systems SG386) of 2.6 GHz. The combined output results in a signal with

a frequency of 3.4 GHz, after filtering out the unwanted harmonics using a high-pass filter. Finally, a frequency doubler is used to increase the frequency to 6.8 GHz to match the hyperfine splitting of ^{87}Rb . The amplified output of approximately +32 dBm is then fed to a log periodic printed circuit board antenna to irradiate the single atom system.

4.2.1 Implementation

Figure 4.3 shows the optical setup to observe the Rabi oscillation in the ground state. Upon trapping and cooling down the single atom, a bias magnetic field of 14.4 G is applied to define the quantization axis for the Zeeman sublevels. Following the state preparation scheme in Chapter 2.5.2, the atom is optically pumped in the $|\uparrow\rangle$ state. We then resonantly drive the microwave transition $|\uparrow\rangle \leftrightarrow |\downarrow\rangle$ with a varying pulse duration, followed by a fluorescence-based state detection scheme (see Chapter 2.5.1) to measure the atomic state population. The experimental sequence is depicted in Fig. 4.4.

The Rabi oscillation in Fig. 4.5 exhibits a Rabi frequency of $\Omega = 2\pi \times (76.78 \pm 0.03)$ kHz, with a visibility of 0.837 ± 0.007 . Assuming there is no other source of error, the maximum visibility is bounded by the state detection fidelity F (see

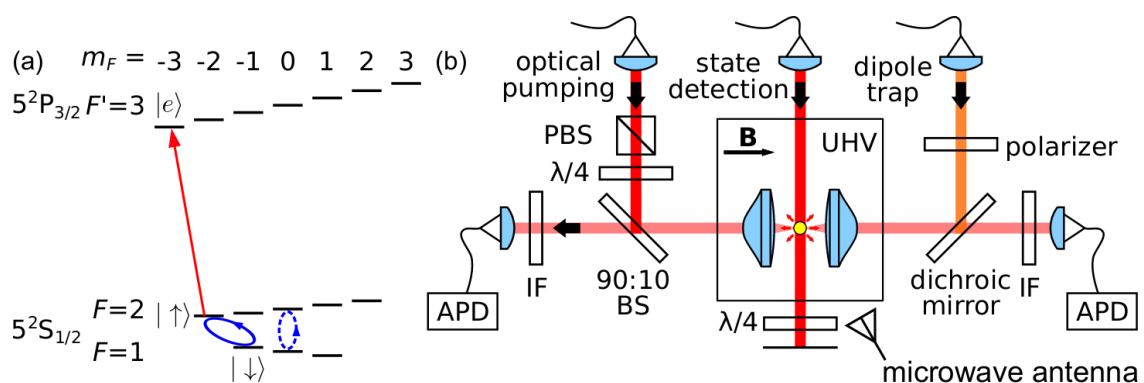


Figure 4.3: (a) Energy level scheme. The solid blue line represents the microwave transition of interest that couples the $|F = 2, m_F = -2\rangle \equiv |\uparrow\rangle$ and $|F = 1, m_F = -1\rangle \equiv |\downarrow\rangle$. The $|\uparrow\rangle$ state can be coupled to $5^2P_{3/2} |F' = 3, m_{F'} = -3\rangle \equiv |e\rangle$ via a cycling optical transition (red arrow). The dashed blue line represents another microwave transition (more description in Chapter 4.4) used as a reference for qubit coherence time. (b) Schematic for probing the coherence of the Zeeman qubit states. UHV: ultrahigh vacuum chamber, IF: interference filter centered at 780 nm, $\lambda/4$: quarter-wave plate, PBS: polarizing beam splitter, BS: beam splitter, B: magnetic field.

CHAPTER 4. GROUND STATE COHERENCE

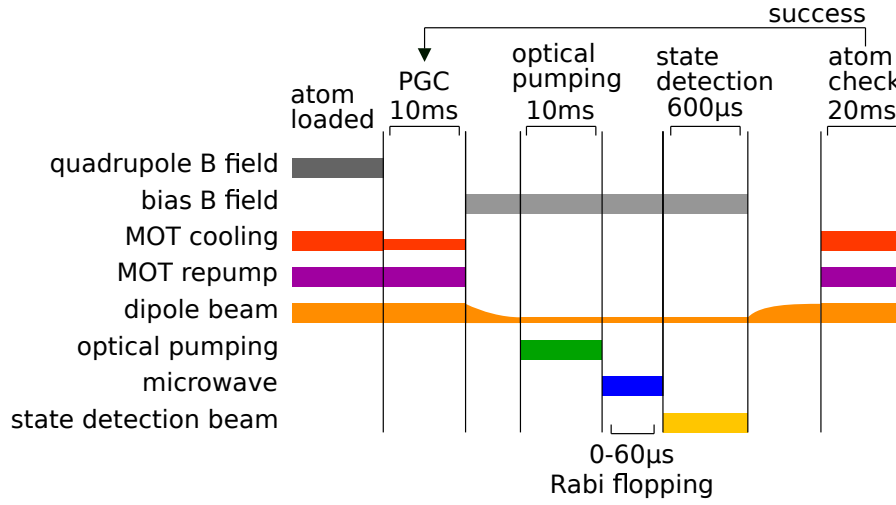


Figure 4.4: Experimental sequence for driving a microwave transition between two ground state Zeeman levels. The qubit system undergoes Rabi oscillations while a resonant microwave field is applied for a pulse duration between 0 and 60 μs .

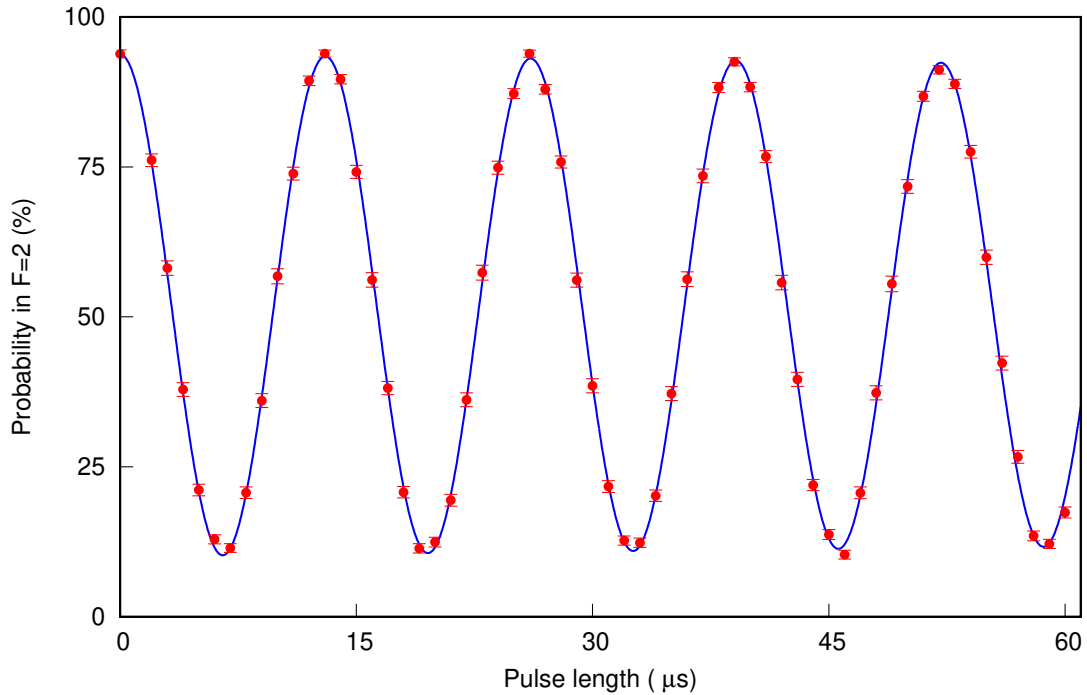


Figure 4.5: Rabi oscillation between $|\uparrow\rangle$ and $|\downarrow\rangle$. The solid line is a fit to an exponentially decaying cosine function to extract the Rabi frequency, $\Omega/(2\pi) = 76.78 \pm 0.03 \text{ kHz}$. Error bars represent the standard error of binomial statistics accumulated from around 1500 repeated sequences.

Eqn. 2.11) following $1 - 2(1 - F) = 0.948 \pm 0.004$. The Rabi oscillation shows little decay within the first $60 \mu\text{s}$, implying that the reduced visibility is most likely due to imperfections in the state preparation process. Particularly, if the atom is initialized in other Zeeman states, it does not couple to the microwave field since the corresponding microwave detuning $\Delta/(2\pi)$ is at least 10 MHz, which is much larger than the Rabi frequency Ω . From the detection fidelity, we deduce that the population of the atom prepared in $|\uparrow\rangle$ state is $88.3 \pm 0.08\%$.

4.3 Ramsey experiment

4.3.1 Implementation

In this part, we characterize the dephasing time for the superposition state $|+\rangle = (|\uparrow\rangle + i|\downarrow\rangle)/\sqrt{2}$. Typically, this decay in coherence is not exponential [121] but it follows

$$w(\tau) = |1 + 0.95(\frac{\tau}{T_2^*})^2|^{-3/2} \cos(\Delta\tau), \quad (4.3)$$

where Δ is the detuning of the driving field and T_2^* is the 1/e dephasing time. The damped profile of $w(\tau)$ is in fact the result of the Fourier transform of the atomic energy distribution (refer to Section 4.3.2 for more discussions on the dephasing mechanism).

The experimental sequence is depicted in Fig. 4.6. After preparing the atom in the $|\uparrow\rangle$ state, we apply a $\pi/2$ pulse to bring the atom to the $|+\rangle$ superposition state. The qubit system then undergoes a free evolution for a period τ in the dipole trap. Finally, a $3\pi/2$ pulse brings the atom back to the $|\uparrow\rangle$ state for a state measurement. We repeat the experiment for different τ and fit $w(\tau)$ in Eqn. 4.3 to the Ramsey contrast, which results in a dephasing time of $T_2^* = 63 \pm 5 \mu\text{s}$, as shown in Fig. 4.7. The oscillatory feature is mostly due to a small detuning between the microwave field and the hyperfine transition (estimated to be $4.3 \pm 0.2 \text{ kHz}$ from the fit).

Particularly, we observe that the Rabi flopping measurement in Fig. 4.5 shows a longer coherence time than in the Ramsey experiment. This is because in the presence of a driving field, the continuously rotating Bloch vector effectively averages out the dephasing mechanism. This phenomenon is also known as “spin locking” in

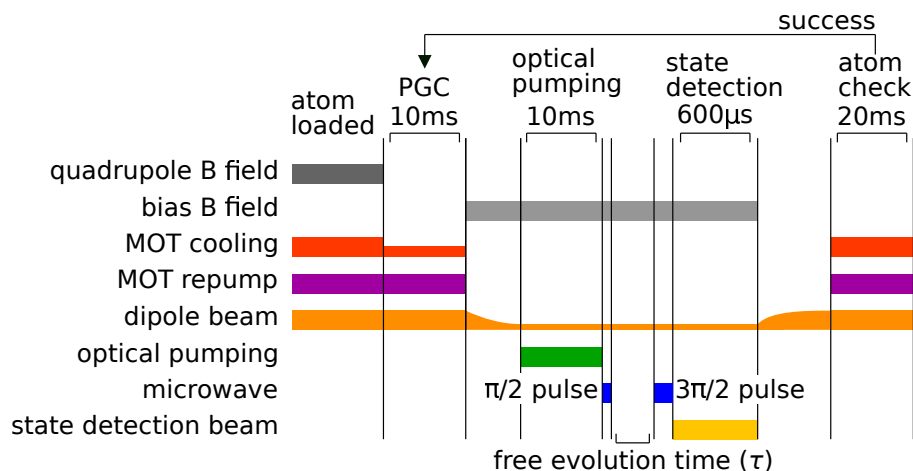


Figure 4.6: Experimental sequence for probing the coherence of the superposition state $|+\rangle = (|\uparrow\rangle + i|\downarrow\rangle)/\sqrt{2}$ using a Ramsey measurement. A $\pi/2$ pulse first prepares the qubit in the $|+\rangle$ state. The qubit system then undergoes a free evolution for a period τ in the dipole trap. Finally, a $3\pi/2$ pulse brings the qubit back to the $|\uparrow\rangle$ state for a state measurement.

the field of quantum control [122].

In the context of nuclear magnetic resonance (NMR), T_2^* refers to the inhomogeneous dephasing time constant which generally describes how a collection of nuclear spins gets out of phase with each other due to spatial inhomogeneity of the driving field [123]. Here we have only one single qubit, we are not able to perform an ensemble average to extract T_2^* . Instead, we measure the dephasing rate by averaging over repeated measurements, which is similar to observing an ensemble of many independent atoms. We will discuss several possible dephasing mechanisms in the following parts.

4.3.2 Dephasing mechanisms

We consider an optically trapped two-level atom prepared in the superposition state $|+\rangle = (|\uparrow\rangle + i|\downarrow\rangle)/\sqrt{2}$. Due to the thermal motion of the atom, in each realization of the experiment, the single atom will be located at a random position in the FORT and will therefore be subject to a different light shift. In particular, if the light shifts experienced by the two qubit states are not the same, this in turn will accumulate a relative phase between the two qubit states, leading to a dephasing process.

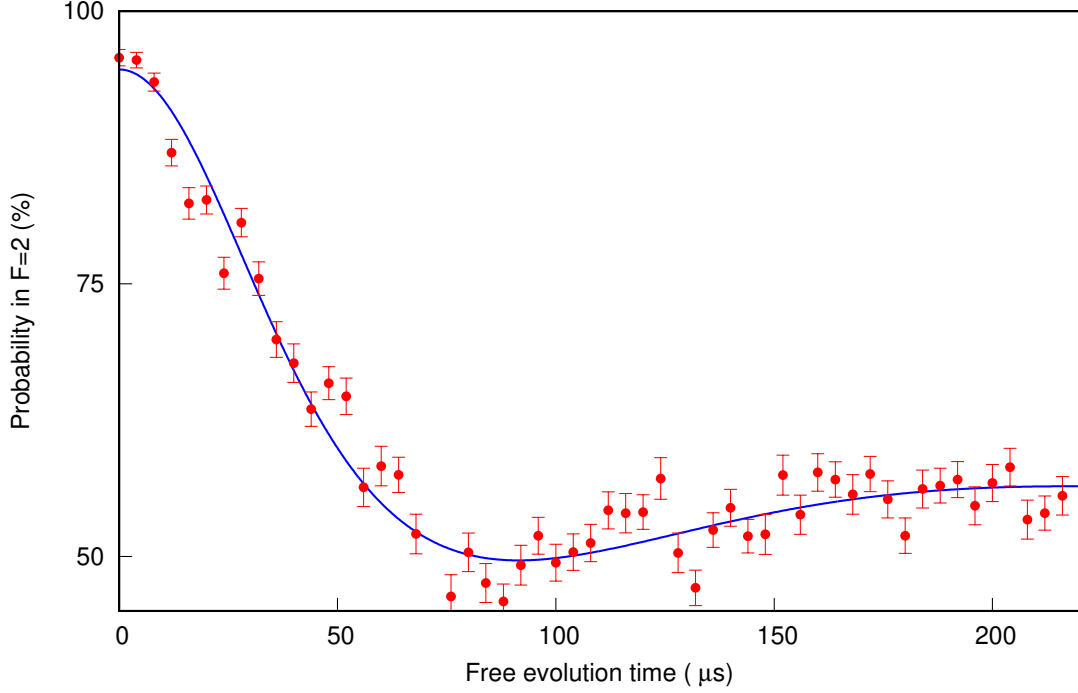


Figure 4.7: Ramsey measurement between the two Zeeman sublevels. From the fit, we extract the characteristic $1/e$ time constant $T_2^* = 63 \pm 5 \mu\text{s}$. The oscillatory feature is mostly due to a small detuning between the microwave field and the hyperfine transition. Error bars represent the standard error of binomial statistics accumulated from around 1000 repeated sequences.

We suppose for a trap potential of U , the light shift experienced by the $|\uparrow\rangle$ and $|\downarrow\rangle$ states are U and $(1 + \eta)U$, respectively. Here, η is a dimensionless scaling factor representing the difference in light shifts of the two Zeeman states. After a time interval of t , the superposition state will become

$$\begin{aligned}
 |\psi(t)\rangle &= \frac{1}{\sqrt{2}} \left(|\uparrow\rangle + i \exp\left[-\frac{i\eta}{\hbar} \int_0^t U(\tau) d\tau\right] |\downarrow\rangle \right) \\
 &\equiv \frac{1}{\sqrt{2}} (|\uparrow\rangle + i \exp[-i\Phi(t)] |\downarrow\rangle), \tag{4.4}
 \end{aligned}$$

for $U = m(\omega_x^2 x^2 + \omega_y^2 y^2 + \omega_z^2 z^2)/2$ for the atom located near the bottom of the FORT, $\vec{\omega} = (\omega_x, \omega_y, \omega_z)$ are the trap frequencies in three directions. Treating the

motion of the atom classically, the trajectory of the atom is then given by

$$\vec{r}(t) = \begin{pmatrix} x(t) \\ y(t) \\ z(t) \end{pmatrix} = \begin{pmatrix} x_0 \cos \omega_x t + (v_{x0}/\omega_x) \sin \omega_x t \\ y_0 \cos \omega_y t + (v_{y0}/\omega_y) \sin \omega_y t \\ z_0 \cos \omega_z t + (v_{z0}/\omega_z) \sin \omega_z t \end{pmatrix}, \quad (4.5)$$

where (x_0, y_0, z_0) is the initial position and (v_{x0}, v_{y0}, v_{z0}) the initial velocity. As the initial conditions are random in every experimental run, the statistical ensemble of the output state can then be evaluated by averaging the state $|\psi(t)\rangle$ over the Boltzmann-distributed initial conditions $p(r_i) \sim \exp(-m\omega_i^2 r_i^2/2k_B T)$ and $p(v_i) \sim \exp(-mv_i^2/2k_B T)$ for $i = x, y, z$:

$$\begin{aligned} \hat{\rho}(t) &= \mathbb{E} [|\psi(t)\rangle\langle\psi(t)|]_{\vec{r}_0, \vec{v}_0} \\ &= \int d^3\vec{r}_0 d^3\vec{v}_0 p(\vec{r}_0, \vec{v}_0) |\psi(t)\rangle\langle\psi(t)|, \end{aligned} \quad (4.6)$$

where $\mathbb{E}[\cdot]$ denotes the expectation value obtained from averaging over the initial conditions.

In general, the integral for the accumulated relative phase $\Phi(t)$ can be quite computationally tedious. One way to simplify this is to consider the atom is static within one experimental run [124], then the light shift experienced by the qubit will no longer have a dependence on time, $U(\tau) = U(\vec{r}_0)$. This assumption represents the worst-case scenario since any time-varying $U(\tau)$ will always oscillate back to 0, leading to a smaller dephasing compared to the constant field assumption. To take this oscillatory behavior into account, a factor of 1/2 can be incorporated into the accumulated phase $\Phi(t) = \eta U(\vec{r}_0)t/2\hbar$. Now, we can represent the statistical averaging with just one random variable $U(\vec{r}_0)$ (which is equivalent to a coordinate transformation from \vec{r}_0):

$$\begin{aligned} \hat{\rho}(t) &= \int_0^\infty dU \frac{2}{\sqrt{\pi}(k_B T)^{3/2}} \sqrt{U} \exp\left(-\frac{U}{k_B T}\right) |\psi(t)\rangle\langle\psi(t)| \\ &= \frac{1}{2} \begin{pmatrix} 1 & (1 - i\eta k_B T t/2\hbar)^{-3/2} \\ (1 + i\eta k_B T t/2\hbar)^{-3/2} & 1 \end{pmatrix}. \end{aligned} \quad (4.7)$$

Defining T_2^* as the $1/e$ dephasing time of the off-diagonal term $|\rho_{\uparrow\downarrow}|^2$, we can then obtain

$$T_2^* = \sqrt{e^{2/3} - 1} \frac{2\hbar}{\eta k_B T} \approx 0.97 \frac{2\hbar}{\eta k_B T}. \quad (4.8)$$

Therefore, the dephasing time T_2^* is inversely proportional to the atomic temperature and also the scaling factor η [121].

The value of the scaling factor varies greatly depending on the light shift mechanism. Here, we discuss three common mechanisms that can cause differences in the light shift on the hyperfine ground states of an optically trapped atom, namely circularly polarized dipole beam light shift, differential light shift, and non-paraxial polarization gradient light shift.

Circularly polarized dipole beam light shift

Consider a far-detuned dipole trap that is circularly polarized. From the expression in Eqn. 2.7, we observe that there is a vector light shift contribution for alkali atoms in the ground state, given by $c_v U_0 \text{Im}[\epsilon^* \times \epsilon] \cdot \hat{\mathbf{F}}$. This gives rise to a Zeeman sublevel-dependent energy shift that is equivalent to the effect of a fictitious magnetic field [125]. Comparing to the Zeeman energy shifts $E_Z = \mu_B g_F \mathbf{B} \cdot \hat{\mathbf{F}}$, we can express this circular light contribution as an effective magnetic field,

$$\mathbf{B}_{\text{eff}} = \frac{U_0 c_v}{\mu_B g_F} \text{Im}[\epsilon^* \times \epsilon], \quad (4.9)$$

where c_v is the coefficient for the vector light shift (refer to Eqn. 2.7), μ_B the Bohr magneton constant, g_F the Landé g-factor, and ϵ the polarization unit vector of the trapping field. We note that for a right circularly polarized light $\epsilon = (\hat{\mathbf{x}} + i\hat{\mathbf{y}})/\sqrt{2}$, \mathbf{B}_{eff} will be pointing towards the $+\hat{\mathbf{z}}$ direction.

Since both the qubit states that we focus on are magnetically sensitive, this circularly polarized component can cause a large frequency shift between the two ground state sublevels. For a circularly polarized trap at 851 nm, the vector light shift will lead to a scaling factor of $\eta_c = 3c_v \approx 0.129$. This corresponds to a dephasing time of $T_2^* \approx 0.97(2\hbar)/(0.129k_B T) = 8.8 \mu\text{s}$ for a typical atomic temperature of $T = 13 \mu\text{K}$, which is prohibitively short for quantum information purposes. One of the reasons we opted for a linearly polarized FORT is to eliminate this vector light shift contribution [64].

Differential light shift

Even in a linearly polarized FORT, the two hyperfine levels $F = 2$ and $F = 1$ in the $5^2\text{S}_{1/2}$ manifold do not experience the same light shift, as the dipole laser

detuning is a little bit closer (by $\omega_{\text{hfs}}/2\pi = 6.8$ GHz, the hyperfine splitting) to the atomic resonances for the $F = 2$ state.

To the first order, we can then express the frequency shift between the two qubit states due to this differential light shift as

$$\begin{aligned}\eta_{DFS} &= \left| \frac{U(\Delta) - U(\Delta - \omega_{\text{hfs}})}{U(\Delta)} \right| \\ &\approx \frac{\omega_{\text{hfs}}}{3} \left| \frac{1}{\Delta_{D1}} + \frac{2}{\Delta_{D2}} \right| \\ &= 2.3 \times 10^{-4},\end{aligned}\tag{4.10}$$

where we have approximated the effective detuning for the dipole light Δ with the weighted contributions from the D_1 and D_2 lines, $1/\Delta = (1/3)(1/\Delta_{D1} + 2/\Delta_{D2})$ [77]. The differential light shift will lead to a dephasing time of $T_2^* \approx 0.97 \frac{2\hbar}{2.3 \times 10^{-4} k_B T} = 5$ ms.

For many quantum metrology applications relying on the quality factor (ratio of transition frequency to dephasing rate) of the transition, this differential light shift effect is often the major limitation, which has to be eliminated via operating with a “magic wavelength” trap [126] or compensating with higher order light shift contributions [127, 128].

Non-paraxial polarization gradient light shift

Near the center of very tightly confining traps with beam waist $w_0 \approx \lambda$, non-paraxial effects can be quite significant. Particularly, even for an ideal linearly polarized input field, the trapping field will become elliptically polarized near the focus (see Fig. 4.8(a)), due to the fact that the polarization of light will have to rotate after passing through a lens for the polarization to remain transverse to the propagation direction [129]. This additional polarization component can be detrimental to coherent manipulation and cooling, as described already in the work of [130, 131].

To quantitatively describe the impact of this non-paraxial effect, we follow the formulation in [132] and [133]: (1) We first compute transformation to get the local polarization of the focusing field. (2) We then numerically propagate the focusing field to the focal region by projecting this focusing field on an orthogonal set of modes with cylindrical symmetry (also known as the angular spectrum) [134].

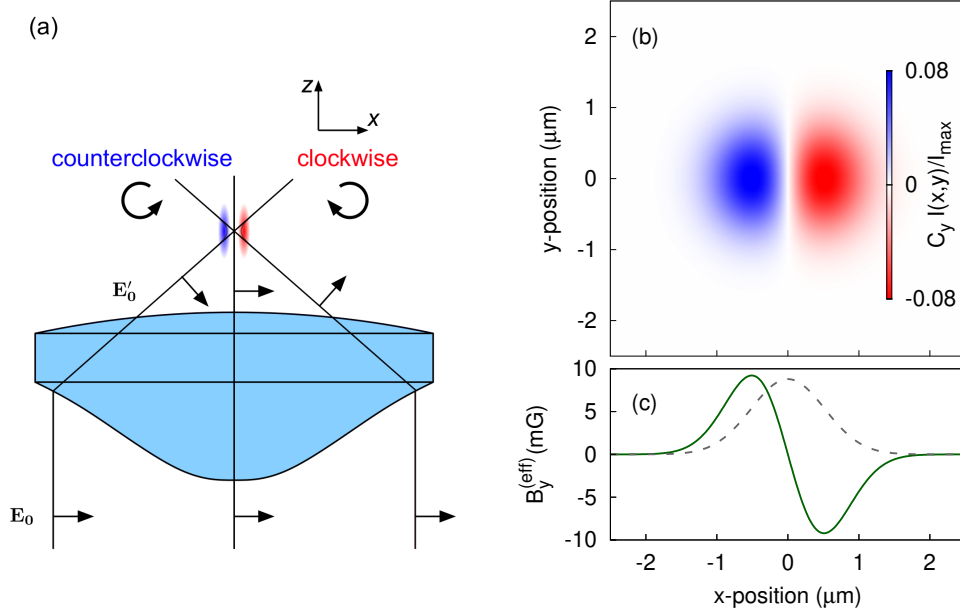


Figure 4.8: (a) Emergence of elliptical polarizations near the focus due to tight focusing. The elliptically polarized component in y -direction is colored in blue (right circularly polarized) and red (left circularly polarized). (b) Normalized intensity of the circularly polarized components $C_y I(\vec{r})/I_{\max}$ on the focal plane ($z = 0$), calculated with our lens and dipole beam parameters. The colors in the density plot represent the handedness of the polarization. (c) A slice of (b) at $y = 0$. Near the focus at $x = 0$, there is a large polarization gradient of $dC_y/dx = -0.27 \mu\text{m}^{-1}$, which corresponds to a magnetic field gradient of magnitude $0.30 \text{ G}/\mu\text{m}$ for a trap depth of $U_0 = k_B \times 0.88 \text{ mK}$. The gray dashed line shows the normalized intensity profile for the linearly polarized component as a comparison.

Using the parameters of our dipole beam and high NA lens, we numerically computed the electric field distribution on the focal plane. We define the vector $\vec{C} = \text{Im}[\epsilon^* \times \epsilon]$ to quantify the direction and degree of ellipticity of an electric field with unit polarization vector ϵ . In this convention, we will have the magnitude $|\vec{C}| = 1$ for a circularly polarized light and 0 for linear polarization. For an input field linearly polarized along x -direction, the most significant term corresponds to the circularly polarized component pointing in the y -direction C_y (orthogonal to the optical axis and the original polarization direction). Therefore, the normalized intensity of the elliptical components $C_y I(x, y)/I_{\max}$ on the focal plane is shown in Fig. 4.8(b).

We observe that the polarization at the focal point still remains linearly polarized.

As we deviate slightly along the x -direction, we quickly see the emergence of the elliptical electric field contribution, which peaks at approximately 8% of the maximum intensity roughly a beam waist away from the center. In our previous discussion on circularly polarized dipole beam light shift, we have established that a circular polarization component can be represented as a fictitious magnetic field according to Eqn. 4.9. The equivalent fictitious magnetic field strength is shown in Fig. 4.8(c). We obtain a polarization gradient of $dC_y/dx = -0.27 \mu\text{m}^{-1}$, which corresponds to a magnetic field gradient of magnitude $B'_y = dB_y/dx = 0.30 \text{ G}/\mu\text{m}$ for a trap depth of $U_0 = k_B \times 0.88 \text{ mK}$. This will lead to a position-dependent energy shift, which dephases the qubit as it undergoes oscillatory motion in the trap.

To mitigate this problem, the standard approach is to apply a large bias magnetic field $\mathbf{B} = B_z \hat{z}$ to suppress the effective field gradient B'_y [131]. In this case, the total magnetic field strength at the location of the atom follows $|\mathbf{B}| = \sqrt{B_z^2 + (B'_y x)^2} \approx B_z + (B_y^2/2B_z)x^2$. Following the treatment described above, the thermal motion of the atom will cause the two qubit states to gain a relative phase due to this fictitious magnetic field gradient. This in turn leads to a dephasing scaling factor of $\eta_{pg} = \mu_B \Delta(g_F m_F) B_y^2 / (3m\omega_{\text{trap}}^2 B_z) \approx 5 \times 10^{-3}$, where $\mu_B \Delta(g_F m_F)$ is the difference in the magnetic moment for the two qubit states. With the bias field of 14.4 G, such a polarization gradient effect has been significantly suppressed, resulting in a $T_2^* \approx 0.2 \text{ ms}$.

From the Ramsey measurement, the measured T_2^* of around $40 \mu\text{s}$ corresponds to a dephasing scaling factor of 2.8×10^{-2} , which is much larger than the estimated dephasing rate for the differential light shift effect and the non-paraxial polarization gradient effect. We suspect the observed dephasing is caused by some circular polarization components in the incident dipole trap beam due to the birefringence of the optics.

4.4 Spin echo

In this part, we apply standard spin echo sequences [135, 136], which add an extra π pulse in the middle of the free evolution window τ (see Fig. 4.9). These sequences help to refocus the atomic state and reverse the inhomogeneous dephasing during the free evolution time, resulting in a much slower decay of the Ramsey

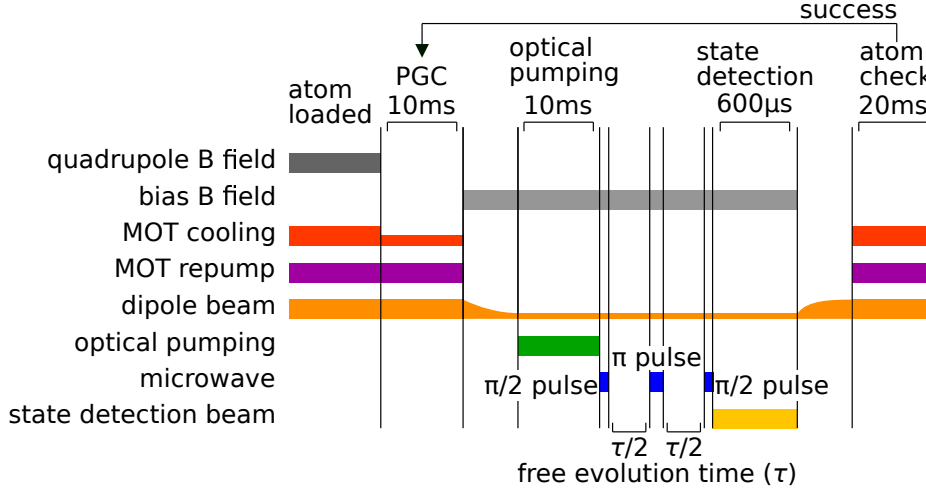


Figure 4.9: Experimental sequence for probing the coherence of the superposition state $|+\rangle = (|\uparrow\rangle + i|\downarrow\rangle)/\sqrt{2}$ in a spin echo measurement. A $\pi/2$ pulse first prepares the qubit in the $|+\rangle$ state. A π pulse is added in the middle of the free evolution window of duration τ to refocus the atomic state. Finally, a $\pi/2$ pulse brings the qubit back to the $|\uparrow\rangle$ state for a state measurement.

contrast. With these sequences, we obtain $T_2 = 480 \pm 21 \mu\text{s}$ for the superposition state $(|\uparrow\rangle + i|\downarrow\rangle)/\sqrt{2}$, as shown in Fig. 4.10(a).

In order to compare the coherence in this qubit with other ^{87}Rb systems [121, 137, 138], we apply the spin echo sequence on the transition between the magnetically insensitive $5^2\text{S}_{1/2}$, $|F = 2, m_F = 0\rangle$ and $|F = 1, m_F = 0\rangle$ Zeeman states, as most of the other experiments were also probing the coherence between these two magnetically insensitive Zeeman states. This magnetically insensitive microwave transition is referred to as the clock transition, as it has been historically exploited as one of the atomic fountain frequency standards [139].

Using the same experimental procedures described above, we find the coherence time of the magnetically insensitive qubit to be $T_2 = 9.5 \pm 0.6 \text{ ms}$ (see Fig. 4.10(b)). This is in reasonable agreement with previous experiments with a typical coherence time of around 10 ms [121, 137, 138]. This measured T_2 for the clock states is about 20 times longer than the one measured for the superposition of $|\uparrow\rangle$ and $|\downarrow\rangle$, also known as the stretched states for the sublevels with the maximum possible value of the angular momentum number. We speculate that the factor of 20 is mostly due to the circular polarization components of the dipole beam and ambient magnetic field fluctuations. Since the stretched states ($|\uparrow\rangle$ and $|\downarrow\rangle$) exhibit a higher sensitivity

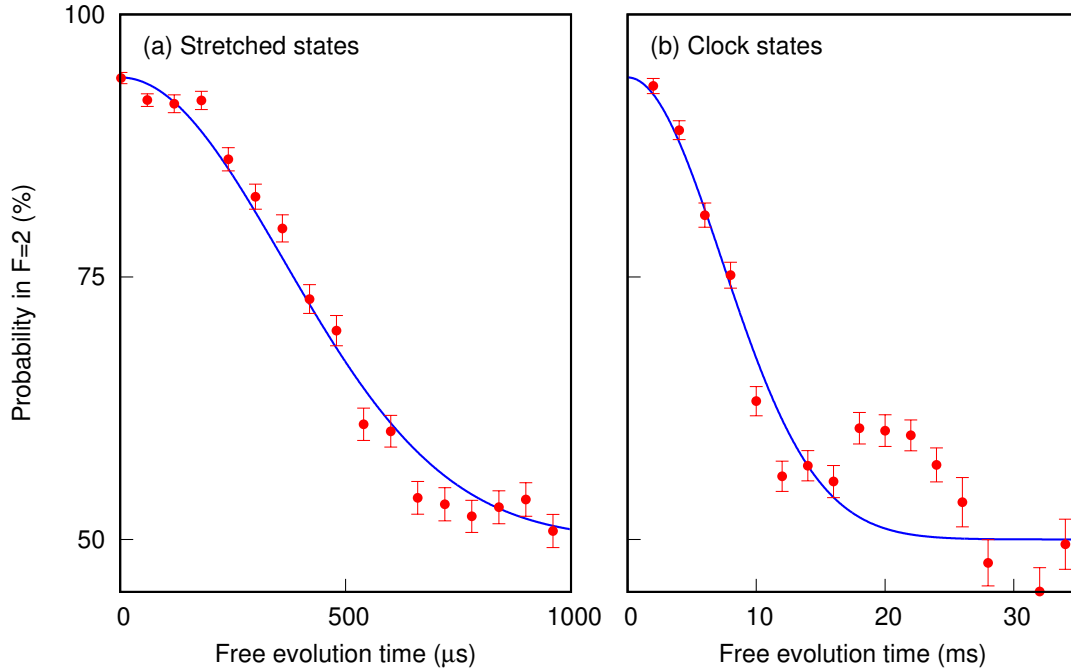


Figure 4.10: Spin echo measurements for the atom prepared in the basis of (a) stretched states $|\uparrow\rangle$ and $|\downarrow\rangle$ or in the basis of (b) clock states $|F = 2, m_F = 0\rangle$ and $|F = 1, m_F = 0\rangle$. We perform a fit to a decaying Gaussian on the spin-echo signals to extract their respective characteristic $1/e$ time: $T_2 = 480 \pm 21 \mu\text{s}$ in (a) and $T_2 = 9.5 \pm 0.6 \text{ms}$ in (b). Error bars represent the standard error of binomial statistics accumulated from around 1000 repeated sequences.

to both the magnetic field and the circular polarization components of the dipole beam, this leads to a more detrimental dephasing mechanism for the superposition states in the $|\uparrow\rangle$ and $|\downarrow\rangle$ basis.

For the clock transition, previous experimental demonstrations have shown that the coherence time can be further improved to tens of milliseconds by reducing the trap depth [121, 138]. The coherence time on the order of hundreds of milliseconds has also been demonstrated by reducing the differential light shift with a magic-intensity trapping technique [140]. Therefore, the magnetically insensitive states are often proposed to be used as a long-lived quantum memory [141].

4.5 Dynamical decoupling

In the previous section, we showed that the spin-echo technique can improve the coherence time of a qubit system. In fact, the spin-echo technique belongs to the class of dynamical decoupling (DD) protocols, which is one type of quantum control techniques to eliminate the effects of the environment [35]. To understand the effect of more complex DD on coherence, we adapt a semiclassical picture in the context of nuclear magnetic resonance (NMR) systems, which classifies decoherence processes into two classes: longitudinal energy relaxation and transverse dephasing, due to random fields imparted by the environment. The longitudinal relaxation process, described by a characteristic energy relaxation time, T_1 , is generally much slower than the transverse dephasing in our system. Particularly, this longitudinal relaxation process is caused by incoherent scattering of the dipole trap beam. A simple estimation following Eqn. 2.5 gives T_1 on the order of tens of milliseconds.

On the other hand, transverse dephasing involves the accumulation of random phases, which is the dominant factor that decreases the state coherence after a duration τ [142]. This can be compensated by applying the control π pulses that flip the sign of the accumulated random phases in different periods alternately. The sequences for some common DD strategies, for instance the periodic DD (PDD) and Uhrig DD (UDD) are shown in Fig. 4.11(a).

To qualitatively understand the efficiency of multipulse sequences on dephasing suppression, we define the state coherence as $W(\tau) = \langle \hat{\sigma}_y(\tau) \rangle$ following [142, 143], which calculates the probability of the qubit state remaining as the superposition state $|+\rangle = (|\uparrow\rangle + i|\downarrow\rangle)/\sqrt{2}$. The state coherence $W(\tau)$ is often described as an exponential decaying function $W(\tau) = \exp(-\chi(\tau))$, with

$$\chi(\tau) = \frac{2}{\pi} \tau^2 \int_0^\infty S(\omega) g_N(\omega, \tau) d\omega, \quad (4.11)$$

where $S(\omega)$ is the power spectral density of environmental noise in the semi-classical picture. Formally, assuming an environmental noise modifies the resonance frequency of the two-level system by $\Delta\omega(t)$, $S(\omega)$ is then defined as the Fourier transform of the autocorrelation for $\Delta\omega(t)$,

$$S(\omega) = \int_{-\infty}^{\infty} dt' e^{-i\omega t'} \mathbb{E}[\Delta\omega(t+t')\Delta\omega(t)]_t, \quad (4.12)$$

which has a unit of Hz^2/Hz .

The function $g_N(\omega, \tau)$ can then be viewed as a frequency-domain filter function of the accumulated random phases for a refocusing sequence consisting of N separate π pulses. The noise filter function $g_N(\omega, \tau)$ is given by

$$g_N(\omega, \tau) = \frac{1}{\omega^2 \tau^2} \left| 1 + (-1)^{1+N} \exp(i\omega\tau) + 2 \sum_{j=1}^N (-1)^j \exp(i\omega\delta_j\tau) \cos(\omega\tau_\pi/2) \right|^2, \quad (4.13)$$

where δ_j is the normalized position of the centre of the j -th π pulse within the total free evolution time τ , $\cos(\omega\tau_\pi/2)$ accounts for the delay caused by a physical π pulse having nonzero pulse interval τ_π .

Figure 4.11(b) illustrates the filtering properties of $g_N(\omega, \tau)$ for PDD sequences. For a fixed free evolution time τ , the peak of the filter function, which is centered close to $\omega = N\pi/\tau$, shifts to higher frequencies as N increases, leading to a reduction of integrated low-frequency noise. On the other hand, for a fixed number of π pulses, increasing the free evolution time τ will shift the filter to lower frequencies.

4.5.1 Periodic sequence

We first apply the simplest pulsed DD scheme, the periodic DD (PDD) sequence, to the single atom qubit for odd number N up to $N = 15$. Figure 4.12 shows the exemplary coherence evolution of the qubit system under the PDD sequence in the case of $N = 3$ and $N = 5$. In contrast to a monotonic decaying profile, we observe that the decaying envelopes contain collapses that always occur at the same partition period $\tau/N \approx 40 \mu\text{s}$, $120 \mu\text{s}$, and $200 \mu\text{s}$ for various N . This happens to match very well with $\omega_z\tau/N$ being the odd multiple of π , where ω_z is the longitudinal trap frequency. This can be understood as a dephasing process caused by the atomic motion in the dipole trap, which has also been observed in previous studies [144, 145]; we will discuss this further in the next section.

To compare various decaying envelopes, we define the coherence time T_2 as the time for the state coherence to decay by a factor of $1/e$. This is consistent with the usual definition in a bare two-level system. As more complex noise spectral components start to manifest because of the DD sequences, the state coherence profile no longer follows a simple Gaussian profile as in the case of a spin echo.

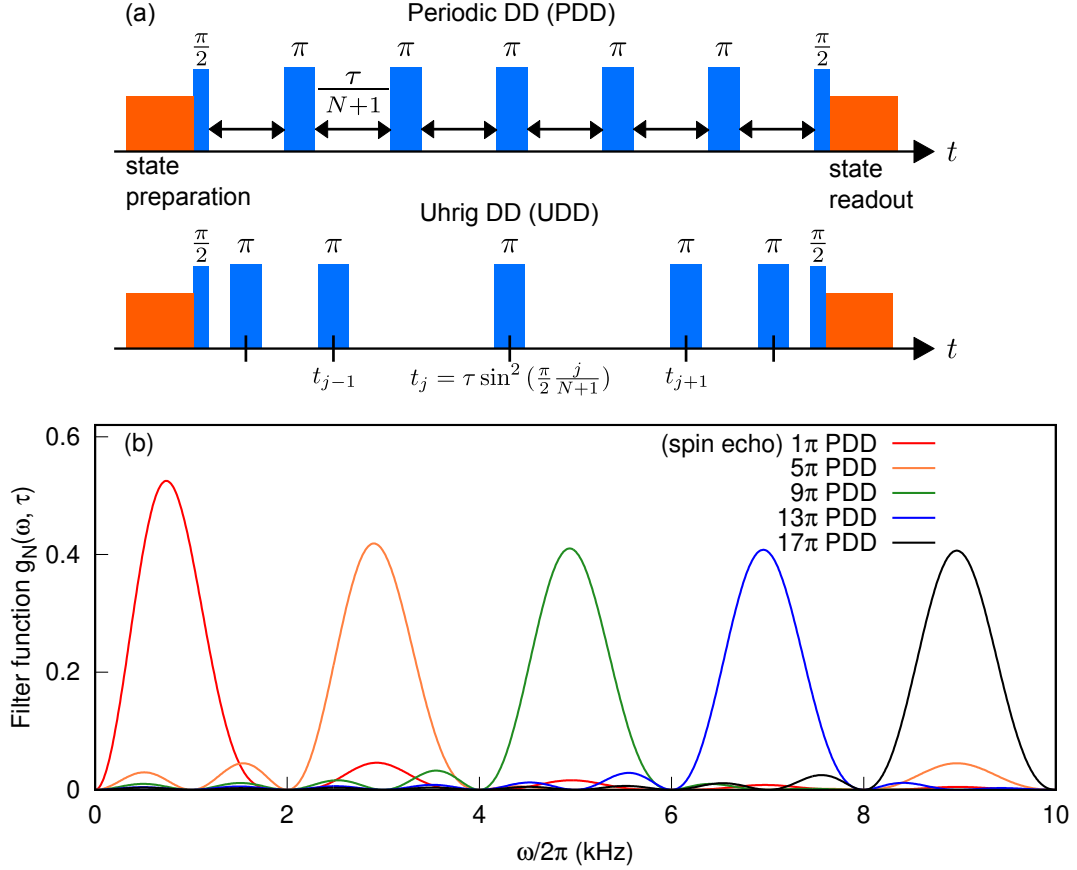


Figure 4.11: (a) Schematic representation of the PDD and UDD sequences. We bring the atom to the $(|\uparrow\rangle + |\downarrow\rangle)/\sqrt{2}$ superposition state and let it evolve freely for a total period τ , with τ being partitioned into small windows using N number of π pulses. PDD partitions τ into uniform periods. UDD has its j -th π pulse locating at t_j , with $t_j = \tau \sin^2[\pi j/(2N + 2)]$. (b) Calculated filter function $g_N(\omega, \tau)$ for PDD with $\tau = 1$ ms, which functions as a bandpass filter. Increasing the number N of π pulses shifts the peak to higher frequencies $\omega = N\pi/\tau$.

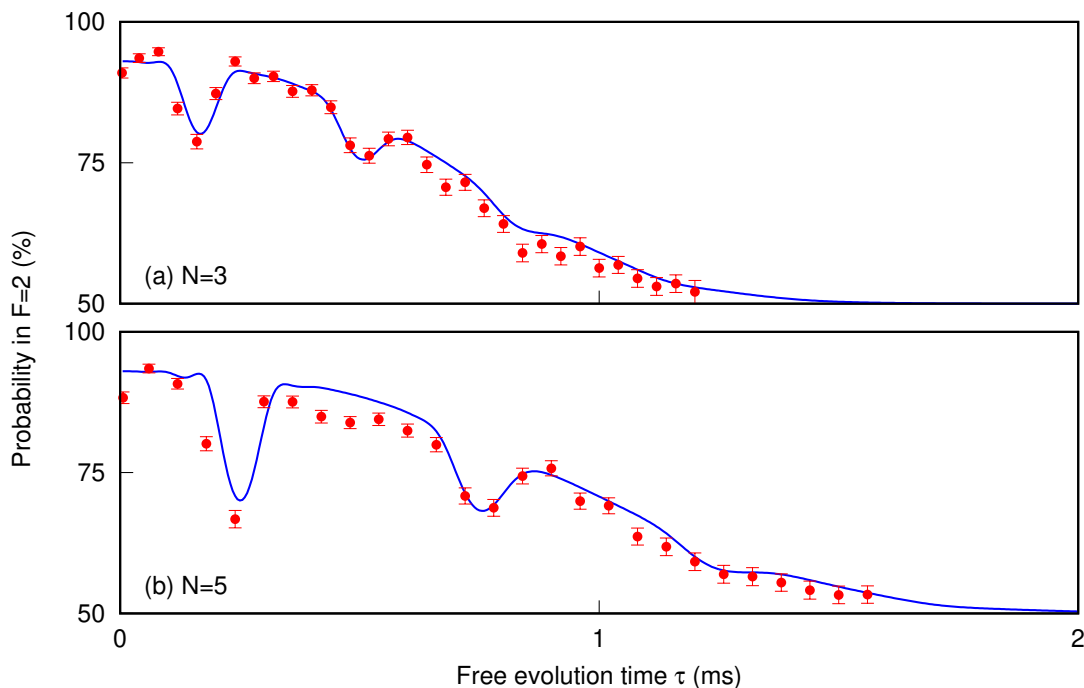


Figure 4.12: Coherence evolution under PDD for (a) $N = 3$ and (b) $N = 5$ π pulses. We observe a drop in the coherence at the same partition period of $\tau/N = 40 \mu\text{s}$, $120 \mu\text{s}$, and $200 \mu\text{s}$. Solid lines are numerical simulations using our heuristic noise model. Error bars represent the standard error of binomial statistics accumulated from 300 repeated sequences.

Therefore, to extract the $1/e$ time, we perform interpolation of experimental data by restricting ourselves only to the tail region of the coherence profile.

Figure 4.13 shows the interpolated coherence time as a function of the number of π pulses. We observe that the coherence time increases with the number of π pulses N in a sequence. From the filter function depicted in Fig. 4.11(b), we have established that increasing the number of π pulses N is equivalent to selecting a frequency band of noise at higher frequencies. As such, our measurements suggest that the noise follows a $1/\omega^\alpha$ spectrum with $\alpha > 0$. A similar trend has been observed in other qubit systems, including single silicon-vacancy centers [146], single nitrogen-vacancy centers [147], and single $^{43}\text{Ca}^+$ ion system [148]. In our system, we are currently limited to pulse sequences with $N \leq 20$ as the contrast of the coherence evolution drops as N increases. This is because pulse imperfections, including errors in the flip angles and the finite pulse width, introduce dephasing to the qubit, as discussed in [149].

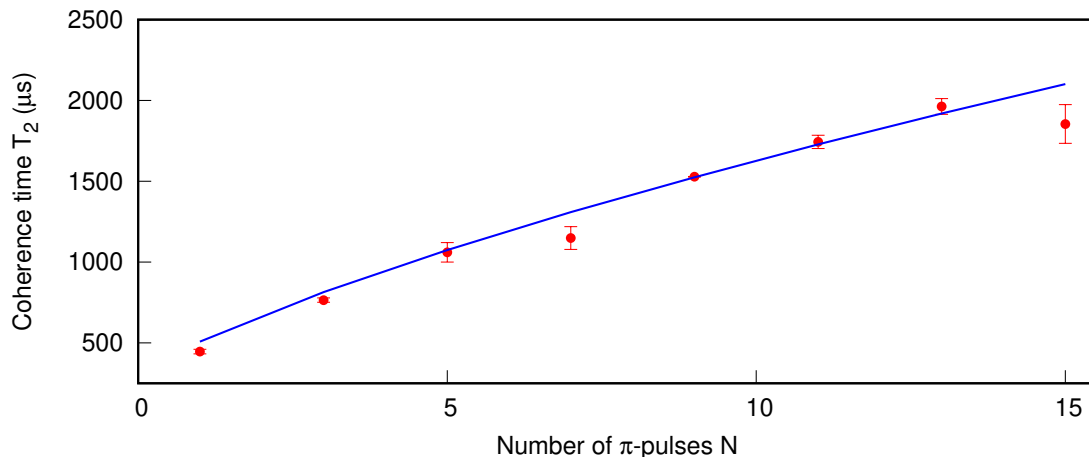


Figure 4.13: Coherence time T_2 as a function of the number N of π pulses. The solid line shows the simulation result for a noise spectrum $S(\omega) \propto 1/\omega^\alpha$ with $\alpha = 1.73$.

We attribute the main source of pulse imperfections in our system to the inexact π pulse timing. We estimate the uncertainty of π pulse timing to be 1% from the Rabi contrast for various numbers N of π pulses. With the multipulse DD sequences, this small deviation from the exact π rotation in the Bloch sphere gives a cumulative error in the results. More robust pulse sequences with pulse phases that are shifted appropriately can be applied to mitigate pulse errors. Nevertheless, the preliminary refocusing strategy here has offered us an insight into the dephasing mechanism of a magnetic-sensitive qubit state.

Noise simulation

With the distinctive features of coherence collapse at multiples of the trap oscillation period and the extended coherence time as more refocusing pulses, it seems to suggest that the environmental noise spectrum in our qubit system can be readily modeled. We consider a simple noise model $S(\omega)$ consisting of a $1/\omega^\alpha$ and a Gaussian centered at the axial trap frequency $\omega_{\text{trap}} = 2\pi \times 12.0$ kHz with a standard deviation of σ_1 :

$$S(\omega) = \frac{S_0}{\omega^\alpha} + S_1 \exp\left(-\frac{(\omega - \omega_{\text{trap}})^2}{2\sigma_1^2}\right). \quad (4.14)$$

Here, the $1/\omega^\alpha$ spectrum represents the noise floor produced by ambient magnetic field fluctuations and power fluctuations of the dipole light field. The Gaussian spectrum represents the light shift due to the atomic motion in an inhomogeneous

dipole light field. Our heuristic noise model is able to predict the recurring features, as shown in Fig. 4.12. We further test our model by comparing the coherence time T_2 for different numbers N of π pulses (Fig. 4.13). Again, the model is in excellent agreement with the experimental data.

Noise reconstruction

In the field of magnetometry, DD is also implemented as a technique to measure the noise spectrum [150, 151]. Particularly, we can reconstruct the noise profile from the state coherence measurement with various DD sequences. Knowing that the filter function behaves as periodic sinc-shaped peaks at frequency $\omega_l \approx (2l + 1)\omega$ with $\omega \approx N\pi/\tau$, we probe the noise spectral density by manipulating N and τ of the DD sequences.

The reconstruction of the noise spectral density $\sqrt{S(\omega)}$ follows the algorithm in [143, 152]. The state coherence $W(\tau)$ is first calculated from the measured bright state population $W(\tau) = 2P_{\uparrow}(\tau) - 1$, which can be approximated to $S(\omega = N\pi/\tau) = -\pi^2 \ln(W(\tau))/(8\tau)$ according to Eqn. 4.11. Essentially, we treat g_N like a transmission cavity with the transmission centered at $\omega = N\pi/\tau$. Then we scan this “cavity” by varying the evolution time τ or number of refocusing pulses N . The factor $\pi^2/8\tau$ gives the transmission bandwidth of this “cavity”.

In the experiment, we fix $N = 5$ and measure the state coherence for various free evolution periods τ . Figure 4.14 shows the noise spectra probed experimentally when the dipole beam power is being varied. We observe the maximum noise density around 10.4, 16.7, and 20.8 kHz for the dipole trap with a trap depth of 0.88, 1.04, and 1.41 mK, respectively. As the dipole beam power increases, the maximum noise density shifts to higher frequencies. The noise peaking at the axial trap frequency can be explained by the polarization gradients of a tightly focused FORT, following [131]. Around the focal plane, the tight focusing of the FORT results in a spatially varying vector light shift of the qubit states. As the trap frequency along axial direction $\omega_z = \sqrt{2U_0/(mz_R^2)}$ following Eqn. 2.9 increases along with the trap depth U_0 , the light shift noise due to oscillatory atomic motion shifts to higher frequencies.

We also observe recurring peaks in the noise spectra at lower frequencies. These peaks are caused by the smaller side lobes of the filter function $g_N(\omega, \tau)$, determined by the DD sequence. We numerically construct the noise spectral density modulated

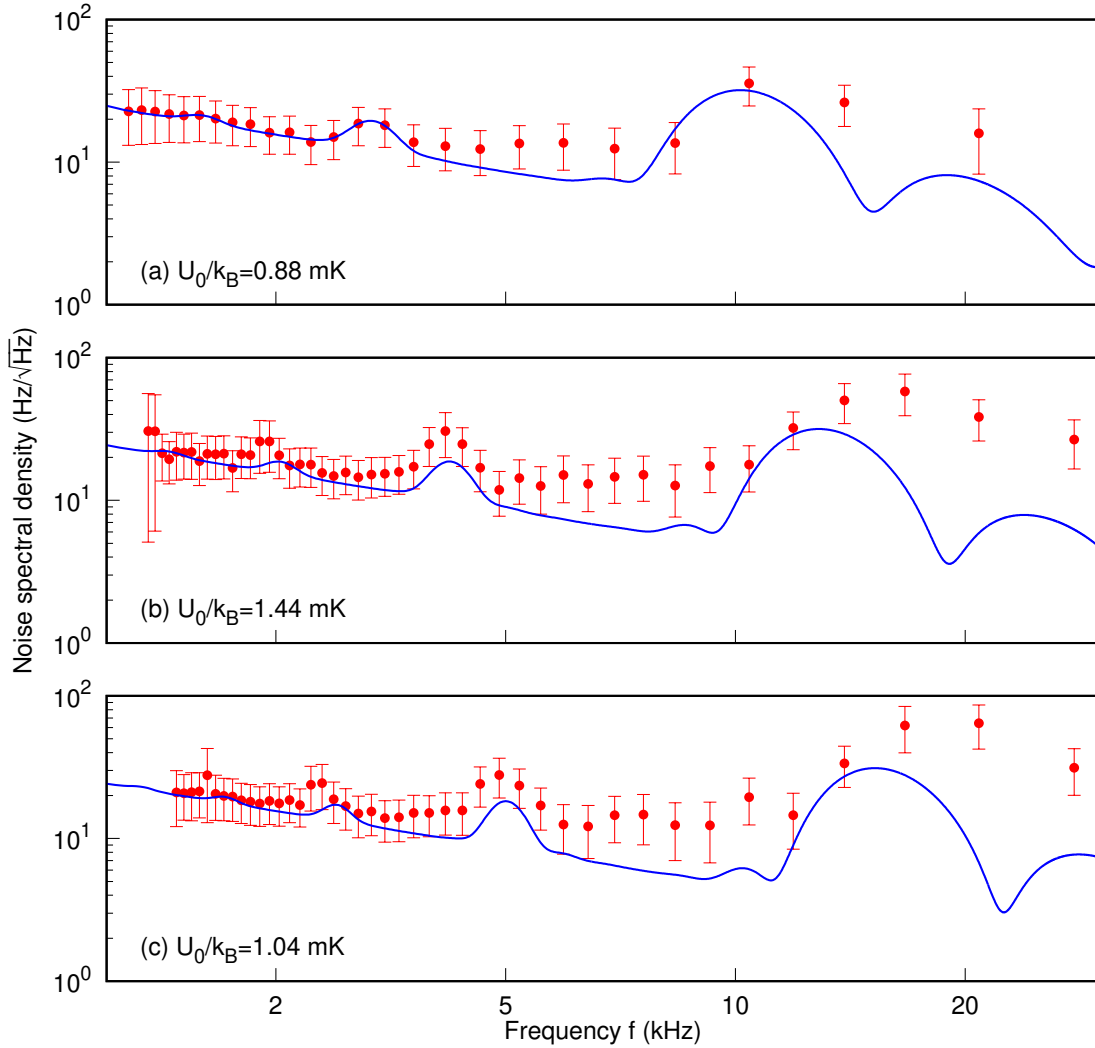


Figure 4.14: Noise spectroscopy with DD adapted from atomic magnetometry. Red circles are the noise spectral density reconstructed with experimental data. The recurring peaks are a feature of the filter function $g_N(\omega)$. Blue solid line represents the simulated outcome. Trap depth is set to be (a) 0.88 mK, (b) 1.04 mK, and (c) 1.41 mK, respectively. The trap frequencies used in simulation are 12.0, 15.2, and 18.0 kHz, respectively.

by the filter function with our heuristic noise model and find that the simulation predicts the recurring features well. By employing a narrower filter function by increasing the number of π pulses N , the trap frequency can be resolved with higher precision. Ideally, we can use this as a basis for the precision measurement of trap parameters.

In fact, the experimentally resolved spectral peaks are actually measurement bandwidth limited. Here, the measurement bandwidth refers to the spectral width of the filter function $g_N(\omega, \tau)$, which is inversely proportional to free evolution time τ . Increasing the number of π pulses (N) enhances the resolution of the noise spectral density. However, there is a trade-off for increasing noise due to the accumulation of pulse errors.

Aside from the peak features, we notice that the background noise floor does not vary with dipole beam power. This implies that the intensity fluctuation of the dipole beam is not the dominant reason for the background noise. In fact, we measure the intensity fluctuation of the dipole beam and find that it only leads to noise spectral density of $0.5 \text{ Hz}/\sqrt{\text{Hz}}$.

4.5.2 Uhrig sequence

After PDD, we also apply the UDD protocols [153] to suppress dephasing in our qubit system. In UDD, the j -th refocusing pulse locates at $t_j = \tau \sin^2 [\pi j / (2N + 2)]$. The UDD sequence has been analytically shown to provide strong suppression of phase accumulation when the noise environment contains a high-frequency component and a sharp high-frequency cutoff. Compared to the PDD protocol with the same number of π pulses (N), the filter function associated with the UDD protocol produces a wider pass band that peaks at a lower frequency, implying that the UDD protocol is more susceptible to low-frequency noise. Another characteristic of the UDD protocol is more pronounced sidelobes compared to the PDD sequence, suggesting potential performance degradation under a broadband noise spectrum.

Figure 4.15 shows the UDD coherence evolution of a single atom qubit. Again, the simulation with our heuristic noise model introduced previously qualitatively predicts the wiggles in the $|\uparrow\rangle$ population as the total free evolution time τ varies. However, the simulation falls short in predicting the magnitude of the wiggles. This

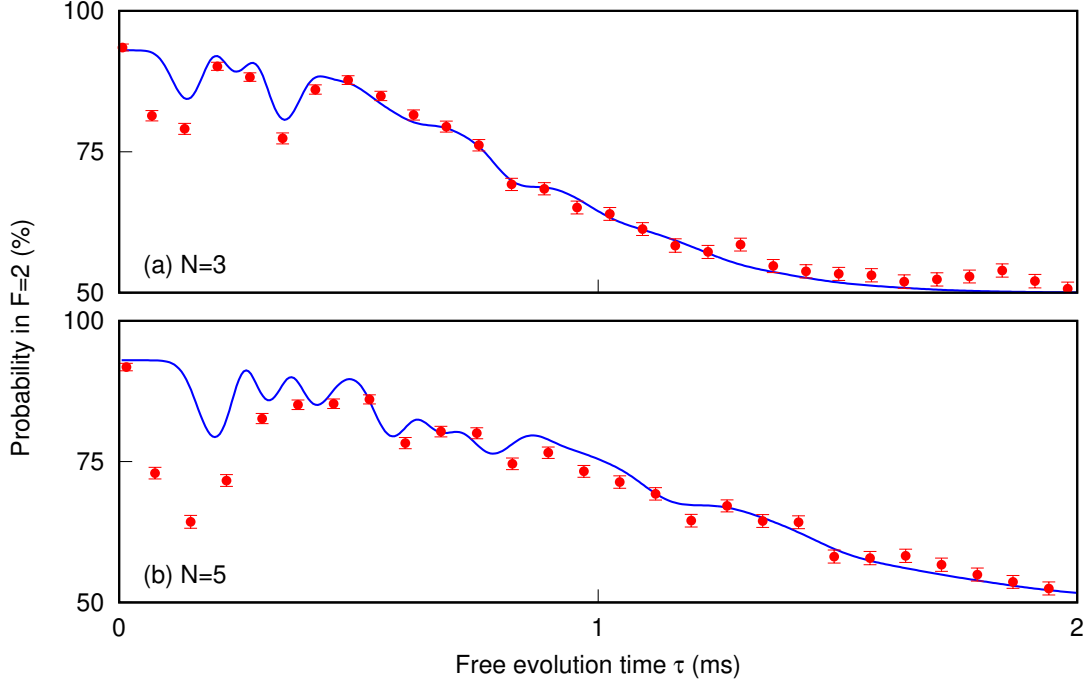


Figure 4.15: Coherence evolution under UDD for (a) $N = 3$ ($T_2 = 926 \mu\text{s}$) and (b) $N = 5$ ($T_2 = 1285 \mu\text{s}$) π pulses. Solid lines are numerical simulations using our heuristic noise model with the same parameters implemented in the previous section. Error bars represent the standard error of binomial statistics accumulated from 300 repeated sequences.

is most likely due to the simplified formulation for the filter function $g_N(\omega, \tau)$ that assumes an instantaneous π pulse.

We also look at the $1/e$ coherence time under the UDD protocol for a free evolution time τ larger than $500 \mu\text{s}$ to minimize the influence of the wiggles. We observe a coherence time of $926 \pm 23 \mu\text{s}$ and $1285 \pm 30 \mu\text{s}$ for $N=3$ and $N=5$ π pulses, respectively. Compared with the coherence time obtained using PDD with the same number of π pulses ($764 \pm 14 \mu\text{s}$ for $N=3$ and $1060 \pm 60 \mu\text{s}$ for $N=5$), we observe an improvement of 21.2% on the coherence time, consistent for both $N=3$ and $N=5$. We also notice that PDD and UDD sequences perform quite similarly because, in general, a DD sequence requires a rather distinctive noise spectrum to outperform the others.

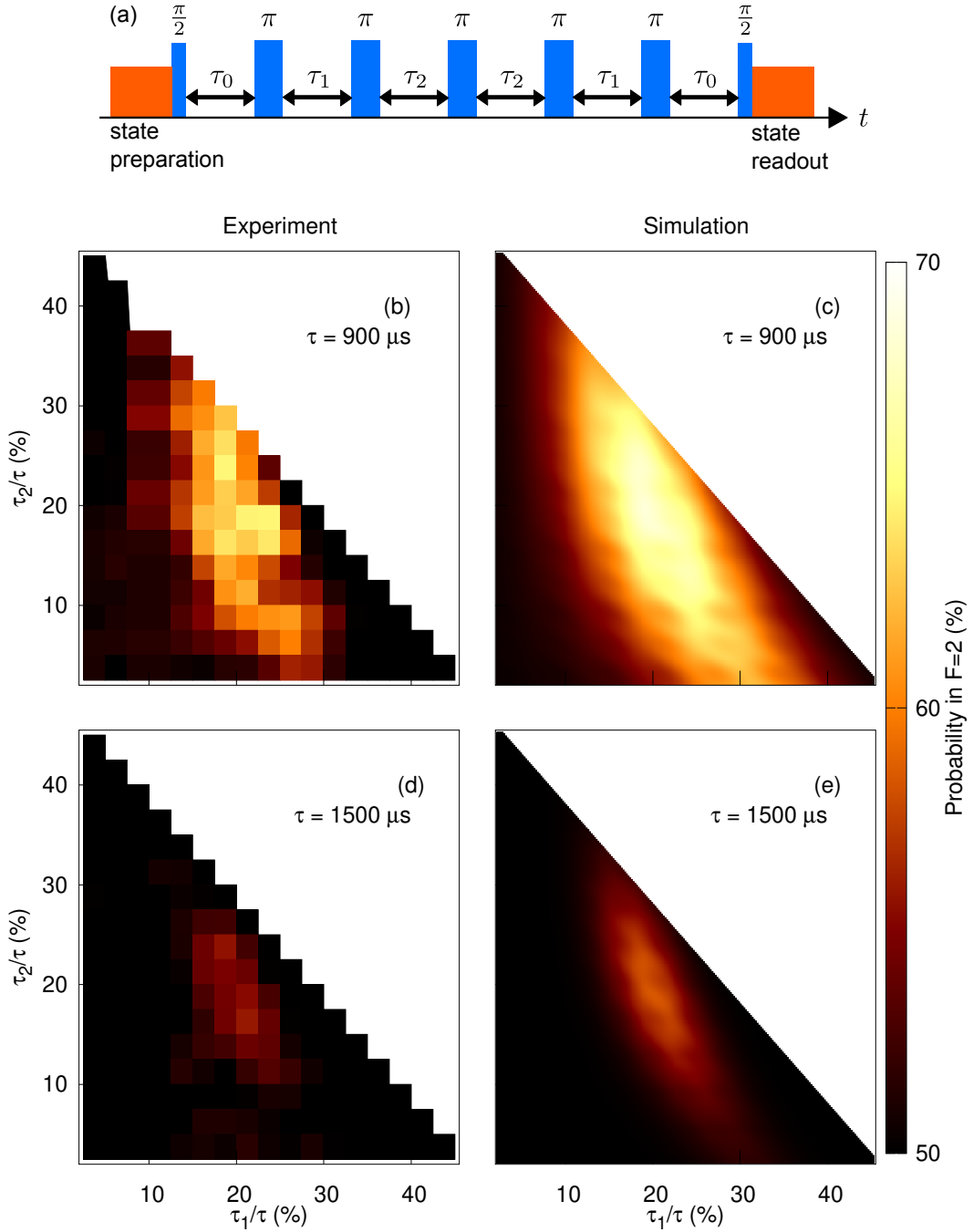


Figure 4.16: Optimization with five π pulses for a fixed free evolution time $\tau = 900 \mu\text{s}$ and $\tau = 1500 \mu\text{s}$. (a) Schematic representation of the DD sequence, satisfying $\tau_0 + \tau_1 + \tau_2 = 0.5\tau$; (b)–(d) population of $F = 2$ state at the end of refocusing. For both $\tau = 900 \mu\text{s}$ and $\tau = 1500 \mu\text{s}$, the maximum fidelity is not given by standard DD sequences such as UDD ($\tau_1/\tau = 18.3\%$, $\tau_2/\tau = 25.0\%$) or PDD ($\tau_1/\tau = 16.7\%$, $\tau_2/\tau = 16.7\%$); the maximal point locates at $\tau_1/\tau = 19.2\%$, $\tau_2/\tau = 19.6\%$ in the simulation.

Optimization to find the optimal sequence

For most applications in quantum information processing, we aim to preserve coherence maximally for a given duration. Here, we demonstrate the optimization protocol with $N=5$ π pulses. In general, this involves $N + 1 = 6$ free parameters for each interpulse period partitioned by a refocusing pulse. As shown in Fig. 4.16(a), we impose a fixed free evolution time τ and reflection symmetry as constraints to reduce the number of free parameters from 6 to 2. To better understand the effect of the noise on the qubit coherence, we numerically calculate the dynamics of the qubit state using our heuristic noise model introduced in previous sections, following Eqn. 4.11.

We find a good agreement between the observed coherence and the model for the same parameters used in the previous section. The maximum coherence is obtained with the protocol that follows $(\tau_0/\tau, \tau_1/\tau, \tau_2/\tau)=(11.2\%, 19.2\%, 19.6\%)$. Strikingly, this optimal sequence matches well with the Carr–Purcell (CP) sequence, which is widely used in the field of NMR and is constructed when the first and last precession periods are half of the duration of the interpulse period, e.g., $(\tau_0/\tau, \tau_1/\tau, \tau_2/\tau)=(10\%, 20\%, 20\%)$ [154].

4.5.3 Carr–Purcell sequence

Inspired by the results above, we apply the CP sequence to our system to prolong the coherence time T_2 . In a CP scheme, the time intervals are partitioned in such a way that the first and the last intervals are half the duration of the other intervals (see Fig. 4.17(a)).

Experimentally, we observe a coherence time of $1017 \pm 38 \mu\text{s}$ and $1274 \pm 42 \mu\text{s}$ for $N = 3$ and $N = 5$ pulses, respectively. The results are shown in Fig. 4.17(b). Compared to the coherence time obtained using the PDD protocol in Fig. 4.13, there is an improvement in T_2 of 33.1% and 20.2% for $N=3$ and $N=5$ π pulses, respectively, which agrees with the optimization results in Fig. 4.16(b). However, the improvement in coherence time halts at larger N . Particularly, the coherence time decreases after $N \geq 15$, due to the drop in signal contrast caused by the accumulation of pulse imperfections.

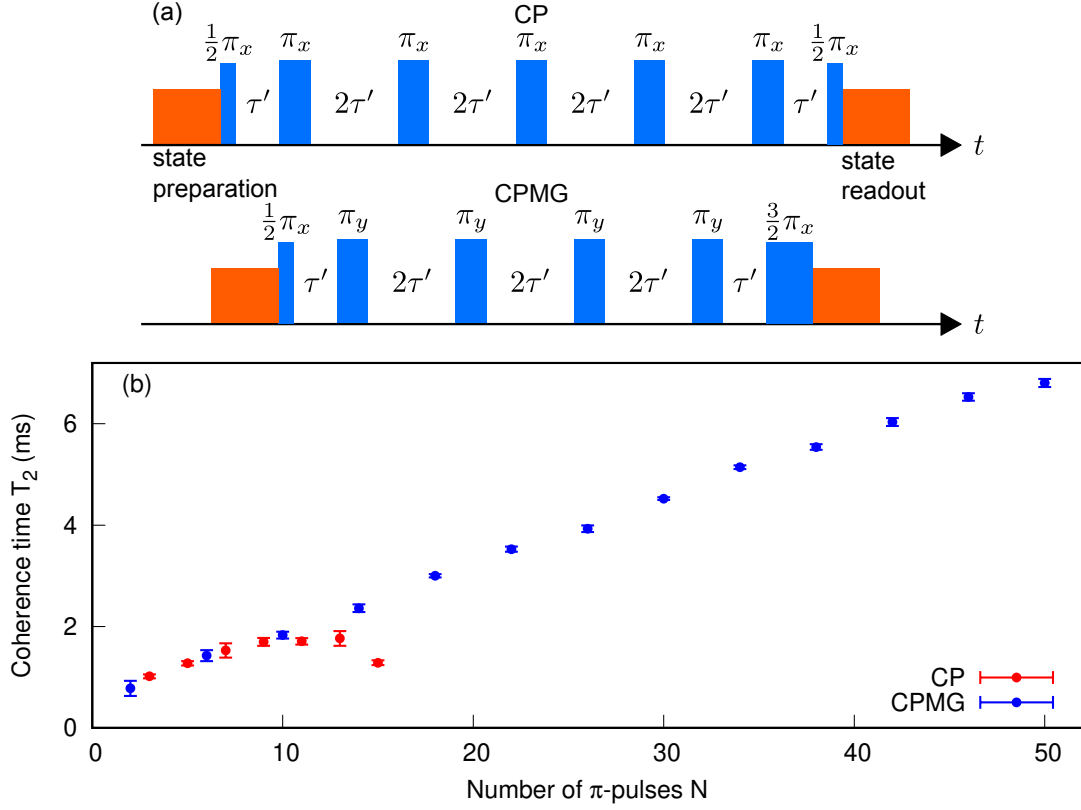


Figure 4.17: (a) Schematic representation of the CP and CPMG sequences. In both sequences, the qubit state is brought to the superposition state $(|\uparrow\rangle + i|\downarrow\rangle)/\sqrt{2}$ with a $\pi/2$ pulse. The first and the last intervals (τ') are half the duration of the other intervals ($2\tau'$), satisfying $2\tau'N = \tau$. In CP, we apply an odd number of π pulses that have the same phase as the $\pi/2$ pulse, denoted as π_x . While in CPMG, we apply an even number of π pulses that have an orthogonal phase as the $\pi/2$ pulse, denoted as π_y . Afterward, the atom is brought back to the $|\uparrow\rangle$ state by a $\pi/2$ pulse ($3\pi/2$) pulse for state measurement in a CP (CPMG) sequence, respectively. (b) Coherence time T_2 as a function of the number N of π pulses for the CP and CPMG sequence. We measure a T_2 of 6.81 ± 0.08 ms with $N = 50$ using the CPMG protocol.

4.5.4 Carr–Purcell–Meiboom–Gill sequence

In order to tackle this problem, we apply the Carr–Purcell–Meiboom–Gill (CPMG) sequence to our qubit system, which has been demonstrated to be able to mitigate pulse imperfections for the preservation of a quantum state [155]. The interpulse period for the CPMG scheme is the same as for the CP scheme, except that the refocusing microwave pulse is 90° phase shifted from the $\pi/2$ pulse, which prepares the superposition state (see Fig. 4.17(a)). This can be understood as a $\pi/2$

rotation along the x -axis in the Bloch sphere, which prepares the superposition state pointing along the y -direction, $(|\uparrow\rangle + i|\downarrow\rangle)/\sqrt{2}$. All the 90° phase shifted refocusing pulses will then be π rotation along y -axis.

We compare the improvement in coherence time under the CPMG protocol to the CP protocol in Fig. 4.17(b). For a small pulse number N , the performance of the CPMG protocol is identical to the performance of the CP protocol. However, with the CPMG sequence, we can apply up to $N = 50$ pulses with reasonably high signal contrast and therefore achieve a coherence time of 6.81 ± 0.08 ms, which is 3.7 times longer than the optimal coherence time obtained with the PDD protocol. We have also applied other variants of the CPMG protocol, such as the XY schemes [156], and we observe similar coherence performance.

4.6 Summary

We have presented a detailed experimental study of the implementation of DD in a single neutral atom qubit system, by comparing the performance among standard DD protocols, including periodic DD, Uhrig DD, CP DD, and CPMG DD. We find an improvement in the coherence time T_2 by 2 orders of magnitude from T_2^* , using the CPMG sequence. With a qubit coherence time of 6.8 ms, our system can be a potential interface platform to facilitate the high-fidelity transfer of quantum states between quantum repeater nodes separated by thousands of kilometers [114].

With the state coherence, we have characterized the noise spectrum of an optically trapped ^{87}Rb atom. By suppressing the motion-dependent dephasing, we expect to see improvements in the coherence times, which will open up new possibilities for the implementation of more robust free-space neutral atom quantum memories for future quantum repeater networks [157]. A better understanding of the qubit response to noise may also help to develop a broadband single-atom sensor that would allow imaging of magnetic fields with a spatial resolution at atomic length scales.

Chapter 5

Fano spectrum and cooling

In this chapter, we investigate free-space cooling of a single neutral ^{87}Rb atom in a mK deep far-off-resonant optical dipole trap (FORT) using electromagnetically induced transparency (EIT), where the trap frequencies are typically around tens of kHz, an order of magnitude smaller than in typical ion traps [158–160] and standing wave traps [161]. We first resolve the Fano profile via excitation spectroscopy, which is the first reported observation of such a profile from a neutral atom system. We then implement a cooling scheme by altering the configuration and detunings, reaching a final temperature of less than $6\ \mu\text{K}$.

5.1 Fano spectrum

We consider an atomic three-level Λ system with two ground states coupled to an excited state by an off-resonant light field each. When one of the driving fields (coupling field) in the system is strong, the corresponding ground to excited transition is strongly mixed. The newly formed eigenstates are comprised of two dressed states with higher energy and one weakly shifted ground state (see Fig. 5.1). Probing the scattering of the atom by scanning the frequency of the weaker field (probe field) reveals two peaks: a wide symmetric profile and, a Fano-type profile characterized by a narrow and bright asymmetric resonance sharply cut on the side by a dip in the atomic fluorescence [162]. The dip, observed when the detunings of the probe and coupling light match, is a consequence of suppression in spontaneous emission due to coherent population trapping in the dark state. Such a profile has been observed previously in spectroscopy of cold ions [163, 164].

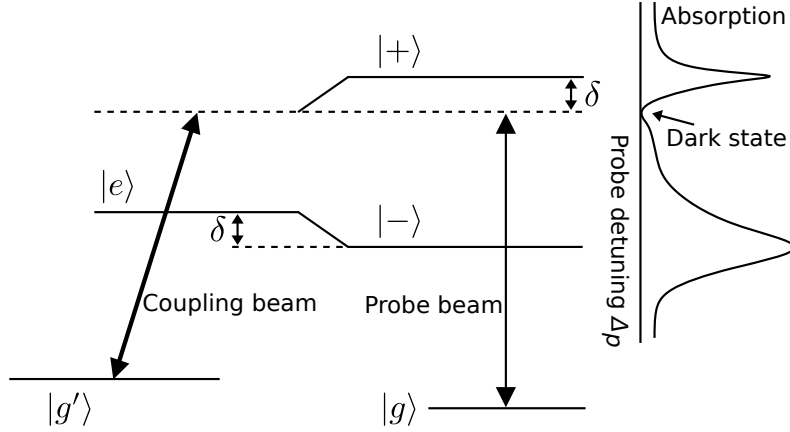


Figure 5.1: Left: A three-level Λ system interacting with a pair of coupling and probe fields. The stronger coupling field drives the $|g'\rangle \leftrightarrow |e\rangle$ transition, leading to new eigenstates ($|\pm\rangle$) with energy shifts of $\pm\delta$. The absorption of the weaker probe field that drives the $|g\rangle \leftrightarrow |e\rangle$ transition will then be modified, as indicated in the absorption curve. Right: The absorption spectrum of a weak probe beam reveals two peaks corresponding to each of the eigenstates and an asymmetric-Fano profile due to the dark state.

5.1.1 Theoretical description

The theoretical framework describing the scattering process for a three-level atom interacting with a pair of coupling and probe fields has been covered extensively in prior research [162, 163]. Here we begin with a quick introduction to establish a common notation. As shown in Fig. 5.1, we consider a Λ system formed by two ground states $|g\rangle$ and $|g'\rangle$, each coupled to an excited state $|e\rangle$ with light fields of frequency ω_p (probe) and ω_c (coupling), respectively.

Under the dipole ($\Omega = \vec{\mu} \cdot \vec{E}/\hbar$ where $\vec{\mu}$ is the atomic dipole moment) and rotating wave approximations, the interaction of a three-level atom with the probe and coupling light can be described by the following effective non-Hermitian Hamiltonian in the rotating frame of the driving field, represented in the space $\{|g'\rangle$ (set to energy 0), $|e\rangle, |g\rangle\}$ [164]:

$$\hat{H}_{\text{int}} = \hbar \begin{pmatrix} 0 & \Omega_c/2 & 0 \\ \Omega_c/2 & -\Delta_c - i\Gamma/2 & \Omega_p/2 \\ 0 & \Omega_p/2 & \Delta_p - \Delta_c \end{pmatrix}. \quad (5.1)$$

Here, Γ is the decay rate of the excited state taken to be the same to both ground states, $\Delta_p = \omega_p - \omega_{eg}$ and $\Delta_c = \omega_c - \omega_{eg'}$ are the detunings of the probe and coupling

CHAPTER 5. FANO SPECTRUM AND COOLING

light frequencies ω_p and ω_c from the respective atomic transitions, and Ω_p (Ω_c) is the Rabi frequency associated with the probe (coupling) driving field.

Eigendecomposition of \hat{H}_{int} reveals the energy shifts and linewidths for the new resonances. In the limit of a weak probe driving field ($\Omega_p \ll \Omega_c, \Delta_c$), the ground state $|g\rangle$ becomes an eigenstate with the energy eigenvalue given by $E_g/\hbar = (\Delta_c - \Delta_p)$. The other two eigenstates $|\pm\rangle$ from the subspace of $\{|g'\rangle, |e\rangle\}$ are associated with the two light-shifted resonances close to $\Delta_p \approx \Delta_c$ and $\Delta_p \approx 0$ as the probe detuning Δ_p is being varied. Their corresponding eigenvalues E_{\pm} , denoted as $E_+/\hbar = (\Delta_c + \delta) - i\Gamma_+/2$ and $E_-/\hbar = -\delta - i\Gamma_-/2$, both consist of a real part representing light shift $\pm\delta$, and an imaginary part accounting for radiative decay Γ_{\pm} . For a large detuning $\Delta_c \gg \Omega_c, \Gamma$, these terms can be approximated through a perturbative expansion to the leading orders of $1/\Delta_c$:

$$\begin{aligned}\delta &= \frac{\Omega_c^2}{4\Delta_c}, \\ \Gamma_+ &= \Gamma \frac{\Omega_c^2}{4\Delta_c^2}, \\ \Gamma_- &= \Gamma - \Gamma_+ = \Gamma \left(1 - \frac{\Omega_c^2}{4\Delta_c^2}\right).\end{aligned}\tag{5.2}$$

For increasing Ω_p , we are no longer able to decompose \hat{H}_{int} in a sum of smaller subspaces, since we cannot neglect the contribution from the coupling between $|g\rangle$ and $|e\rangle$. Previous theoretical work has looked into this problem and solved the steady solution for the three-level optical Bloch equation around $\Delta_p \approx \Delta_c$, which gives [164]

$$\begin{aligned}\delta &= \frac{\Delta_c}{4\Delta_c^2 + \Gamma^2}(\Omega_c^2 - \Omega_p^2), \\ \Gamma_+ &= \frac{\Gamma}{4\Delta_c^2 + \Gamma^2}(\Omega_c^2 + \Omega_p^2), \\ \Gamma_- &= \Gamma - \Gamma_+ = \Gamma \left(1 - \frac{\Omega_c^2 + \Omega_p^2}{4\Delta_c^2 + \Gamma^2}\right).\end{aligned}\tag{5.3}$$

Nevertheless, the narrow resonance associated with $|+\rangle$ is shown to exhibit an asymmetric Fano-shaped profile [162] and possess a spectral width Γ_+ much smaller than the natural linewidth Γ for $\Omega_c, \Omega_p \ll \Delta_c$. Adapting from the formulation in [162], this Fano profile can be represented by the transition probability $|T|^2$ from

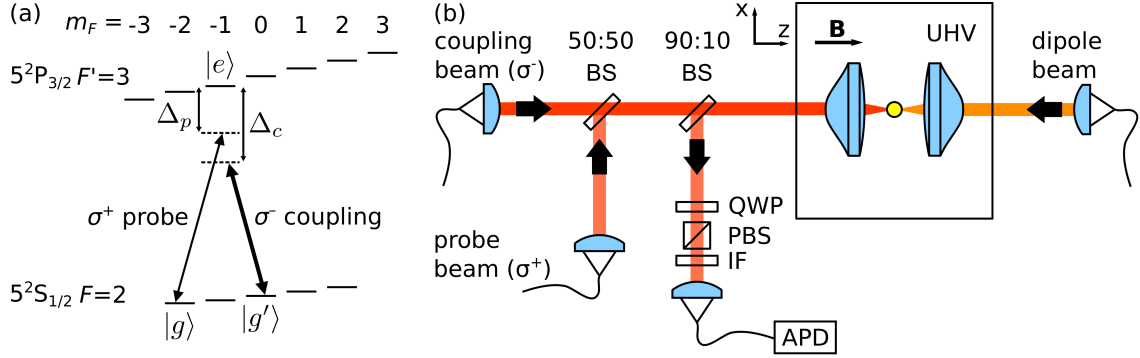


Figure 5.2: (a) Energy levels and transitions in ^{87}Rb used for observing the Fano scattering profile. (b) Optical setup for Fano spectroscopy. The backscattered atomic fluorescence is collected by the high numerical aperture lens and coupled to a single-mode fiber connected to an avalanche photodetector. BS: beamsplitter, QWP: quarter-wave plate, PBS: polarizing beamsplitter, IF: interference filter, APD: avalanche photodetector, UHV: ultra-high vacuum. B: magnetic field

state $|g\rangle$ to state $|e\rangle$, given by

$$\begin{aligned}
 |T|^2 &= \frac{64\hbar^2\Omega_p^2\Gamma^2}{4(\Delta_p + \delta)^2 + \Gamma_-^2} \frac{[2\delta/\Gamma_+ + 2(\Delta_p - \Delta_c - \delta)/\Gamma_+]^2}{1 + [2(\Delta_p - \Delta_c - \delta)/\Gamma_+]^2} \\
 &\equiv \frac{64\hbar^2\Omega_p^2\Gamma^2}{4(\Delta_p + \delta)^2 + \Gamma_-^2} \frac{(q + \epsilon)^2}{1 + \epsilon^2}, \tag{5.4}
 \end{aligned}$$

where the first fraction represents a resonance near $\Delta_p = -\delta$. The second fraction follows the form of a Fano resonance profile with the Fano parameter $q = 2\delta/\Gamma_+$ and the reduced variable $\epsilon = 2(\Delta_p - \Delta_c - \delta)/\Gamma_+$.

Historically, the Fano resonance line shape was first discussed in the context of the excitation spectra of electron scattering by Helium atoms [165]. It can be understood as the interference between two scattering processes: one that drives a discrete state resonantly, and another one within a continuum of states. In our case, the emergence of a Fano profile in fluorescence scattering is caused by the interference between the narrow $|g\rangle \rightarrow |+\rangle$ transition and the $|g\rangle \rightarrow |-\rangle$ transition, which has a much larger radiative linewidth $\Gamma_- \approx \Gamma$ and can be approximated as a continuum process.

5.1.2 Implementation

To observe the Fano spectrum from a single ^{87}Rb atom, we consider a Λ system formed by the Zeeman sublevels $|g\rangle \equiv |F = 2, m_F = -2\rangle$ and $|g'\rangle \equiv |F = 2, m_F = 0\rangle$

CHAPTER 5. FANO SPECTRUM AND COOLING

of the $5^2S_{1/2}$ $F=2$ hyperfine ground state, and $|e\rangle \equiv |F' = 3, m_{F'} = -1\rangle$ of the $5^2P_{3/2}$ $F'=3$ excited state, subject to a pair of driving fields with opposite polarizations. As indicated in Fig. 5.2(a), a stronger left circularly polarized (σ^-) coupling beam of Rabi frequency Ω_c , couples the state $|g'\rangle$ to $|e\rangle$ with a detuning Δ_c . A weaker right circularly polarized (σ^+) probe beam of Rabi frequency Ω_p and detuning Δ_p drives the $|g\rangle \leftrightarrow |e\rangle$ transition.

Figure 5.2(b) shows a simplified schematic of our experimental setup. We trap a single ^{87}Rb atom at the focus of a pair of high numerical-aperture (NA) aspheric lenses in a far-off-resonant dipole trap (FORT). The FORT is formed by a linearly polarized Gaussian beam at 851 nm (dipole beam), tightly focused by a high NA lens to a waist of $w_0 = 1.1 \mu\text{m}$. The single atom is loaded into the FORT from a MOT. The aspheric lenses with a NA of 0.75 form the key component of our experiment as they not only enable tight spatial confinement of the atom in the FORT but also allow efficient collection of fluorescence from the atom.

For driving the Λ system, the coupling and probe beams employed are generated from the same external cavity diode laser. This ensures a fixed phase relationship between the two driving fields. The light from this laser is split into two paths for the coupling and probe beams with the frequency of light independently controlled by an AOM in each path. The two beams are then overlapped in a beam splitter and sent co-propagating to the atom. This can avoid heating processes as a consequence of undesired motional coupling arising from the momentum transfer ($\Delta\vec{k} = \vec{k}_c - \vec{k}_p$, where \vec{k}_c and \vec{k}_p are the wavevector of the coupling beam and probe beam, respectively) involved in the two-photon process (more details are described in the cooling part in Chapter 5.2.1).

To prevent probe and coupling beams from entering the detection system, the atomic fluorescence is collected in the opposite direction of the probe and coupling beams using a 90:10 beam splitter, similar to the Mollow experiment described in Chapter 3.3.1. We employ a polarization filter consisting of a quarter-wave plate (QWP) and polarizing beam splitter (PBS) to selectively collect the left or right circularly polarized fluorescence scattered by the atom. This is to eliminate scatterings from the $|F = 2, m_F = -2\rangle \rightarrow |F' = 3, m_F = -3\rangle$ cycling transition induced by the strong coupling field, which can obscure the weak scatterings from the two-photon process from the Λ scheme.

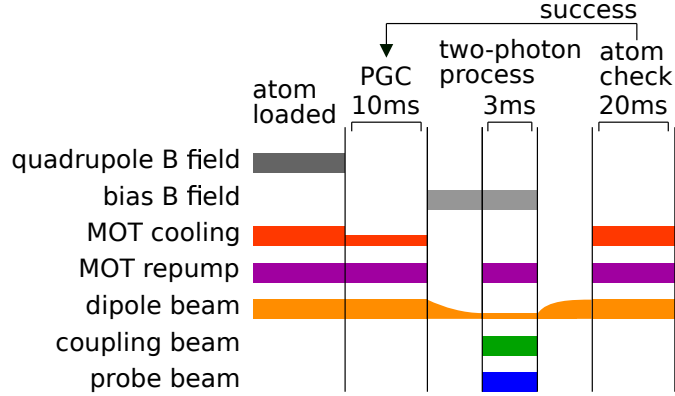


Figure 5.3: Experimental sequence for measuring the Fano scattering profile. The coupling and probe beams are applied for a duration of 3 ms, during which the atomic fluorescence is recorded using an APD.

The experimental sequence is depicted in Fig. 5.3. When a single ^{87}Rb atom is loaded into the FORT from the MOT, we perform PGC for 10 ms and apply a bias magnetic field of 14.4 G along the optical axis to remove the degeneracy of the Zeeman sublevels. Next, the single atom is illuminated with the pair of strong coupling and weak probe beams for 3 ms. During this interval, the atomic fluorescence is detected using an APD. The measurement is repeated over approximately 3000 runs for various values of Ω_p as Δ_p is scanned by $\pm 2\pi \times 6$ MHz around Δ_c while the coupling beam parameters remain fixed at $\Delta_c = -2\pi \times 80$ MHz and $\Omega_c = 1.4\Gamma$.

Figure 5.4 shows the detected fluorescence count rates projected in σ_R circular polarization, which corresponds to the $|F = 2, m_F\rangle \leftrightarrow |F' = 3, m_{F'} = m_F + 1\rangle$ transition ($|g\rangle \leftrightarrow |e\rangle$), and σ_L circular polarization, which corresponds to the $|F = 2, m_F\rangle \leftrightarrow |F' = 3, m_{F'} = m_F - 1\rangle$ transition ($|g'\rangle \leftrightarrow |e\rangle$). The blue solid curves display the fitting of a Fano line shape given in Eqn. 5.4 to the experimental spectra (red points). We notice that the fluorescence detection rates for the two circular polarizations have opposite skewness, where the orientation of the skewness depends on the sign of the detuning Δ_c . The peak associated with the σ_R light is skewed left while the peak associated with the σ_L light is skewed right.

For all probe powers, an asymmetrical Fano peak is observed with a linewidth smaller than the natural linewidth ($\Gamma = 2\pi \times 6$ MHz). As shown in Fig. 5.5, the Fano linewidths extracted from the fits increase linearly with probe intensities ($\Gamma_+/2\pi = 350 \pm 30, 410 \pm 30, 700 \pm 40, \text{ and } 1000 \pm 50$ kHz for probe saturation parameters of

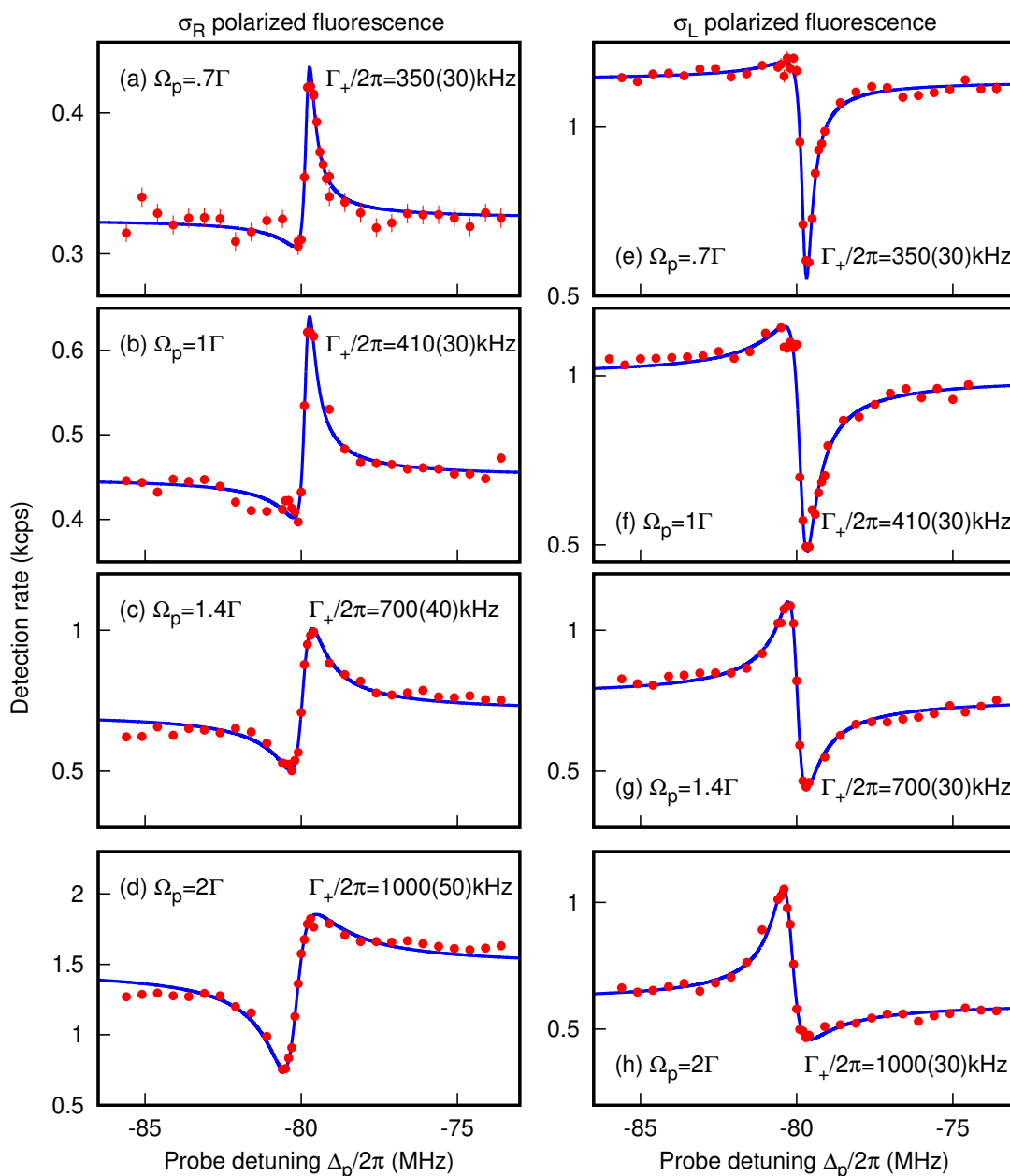


Figure 5.4: Observation of Fano scattering profiles. Red dots: Single photon scattering detected in APDs from the off-resonant two-photon process, projected into the probe polarization (left column) or the pump polarization (right column). Blue curve: Fits to Fano profiles following Eqn. 5.4. The probe beam power increases from subplot (a) to (d) (similarly, (e) to (h)) as indicated by the Rabi frequency values. All plots show a clear suppression in scattering at $\Delta_p/2\pi \approx -80$ MHz where the atom is optically pumped to the dark state. Error bars represent the standard error of the mean determined from around 2000 repeated experimental sequences.

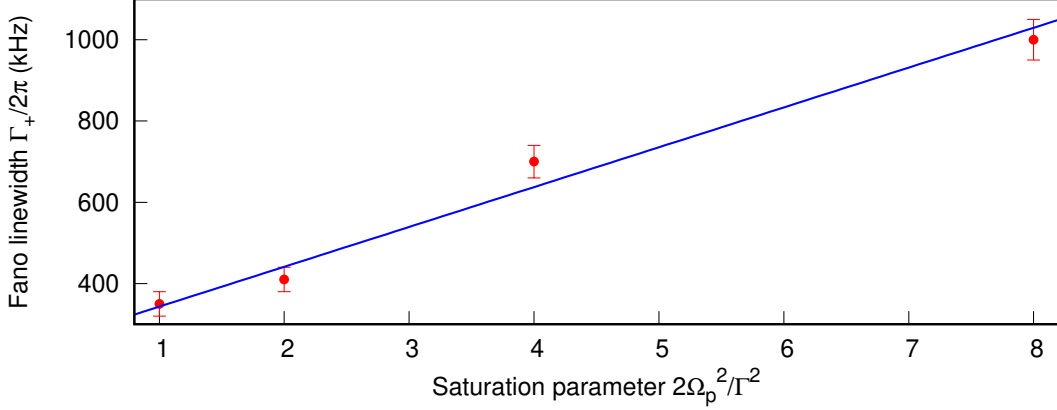


Figure 5.5: Linear increase in the Fano linewidths as a function of probe intensities. The blue solid line is a fit to a linear function. Red dots are the Fano linewidths extracted from the fits performed to the scattering profile in Fig. 5.4. Error bars represent one standard deviation obtained from least-squares fit of the individual spectra.

$2\Omega_p^2/\Gamma^2 = 1, 2, 4,$ and $8,$ respectively). Compared with the theoretical predictions calculated using the expression in Eqn. 5.3 ($\Gamma_+/2\pi \approx 83, 100, 132,$ and 201 kHz), the measured values are larger by about a factor of 4.7 ± 0.6 for all probe powers. This discrepancy here could be attributed to the presence of multiple Fano resonances resulting from other Zeeman sublevels. Specifically, there is a Λ configuration involving the states $|F = 2, m_F = -1\rangle, |F' = 3, m_{F'} = 0\rangle,$ and $|F = 2, m_F = 1\rangle,$ as well as another Λ configuration formed by the states $|F = 2, m_F = 0\rangle (|g'\rangle), |F' = 3, m_{F'} = 1\rangle,$ and $|F = 2, m_F = 2\rangle.$ As the transition matrix elements that couple between the ground and excited state are quite different for these Λ configurations, they lead to distinct shifts and linewidth in the resonance. Consequently, the scattering profiles for these three sets of Λ configurations could overlap and distort the total scattering rate, causing the apparent broadening of the Fano feature. It is possible to evaluate the contributions from the other Zeeman sublevels by solving a twelve-level optical Bloch equation that incorporates all the sublevels. This work is currently underway.

Furthermore, the dark state, or the dip in the scattering spectra, ideally should remain fixed at $\Delta_p = \Delta_c,$ independent of the driving fields. However, we observe that the minimum of the scattering is actually shifting to a larger detuning for increasing $\Omega_p.$ This is because the probe field Ω_p also drives the transition between $|g'\rangle = |F = 2, m_F = 0\rangle$ and the excited state $|F' = 3, m_{F'} = 1\rangle,$ which is not taken

into account in the three-level model. This coupling effectively imposes an additional light shift on $|g'\rangle$, leading to the shift in the scattering feature.

5.2 EIT cooling

In the previous experiment, we demonstrated that a Fano resonance can be engineered to have subnatural linewidth by choosing a suitable Ω_p and Ω_c . In fact, when the motional spread of the atomic wavepacket in an external conservative potential is taken into account, the dark state becomes sensitive to the atomic position in such a potential. This position dependence can additionally be engineered to cool down the atom [166]. Specifically, when the dark state is decoupled from the excited state at the carrier frequency but is coupled to a bright state at the red sideband (which has one phonon energy lower), it results in cooling as the atom transitions to a lower vibrational state.

If the energy difference between the dark state and a higher energy bright dressed state is made to match the vibrational mode spacing of the trap confining the atom, an atom transiently pumped into the dark state is coupled to the bright state from a lower vibrational mode. It can thus emit a phonon and transfer to the respective dressed state, cooling down in the process. This cooling technique has been implemented in platforms such as trapped ions [158–160], neutral atoms confined in standing wave traps [161], and quantum gas microscopy setups [167].

5.2.1 Theoretical model

We consider a trapped atom in a one-dimensional harmonic potential given by a trap frequency of ω_{trap} and motional eigenstate $|n\rangle$. In this case, the Fano profile associated with the sideband transitions $|n\rangle \rightarrow |n \pm 1\rangle$ will have an energy shift of $\pm \hbar\omega_{\text{trap}}$ to account for the quantized energy spacing of the harmonic oscillator. Furthermore, at the minimum of the Fano profile ($\Delta_p = \Delta_c$), the $|g, n\rangle \rightarrow |e, n\rangle$ transition is suppressed due to the formation of a dark state. With a positive detuning for Δ_c and Δ_p , along with a suitable Ω_c , we can tailor the absorption spectrum to fulfill $\delta = \Omega_{\text{trap}}$. This corresponds to having the $|g, n\rangle \rightarrow |+, n-1\rangle$ red sideband overlap with the dark state, signifying the enhancement of the red sideband transition (see Fig. 5.6).

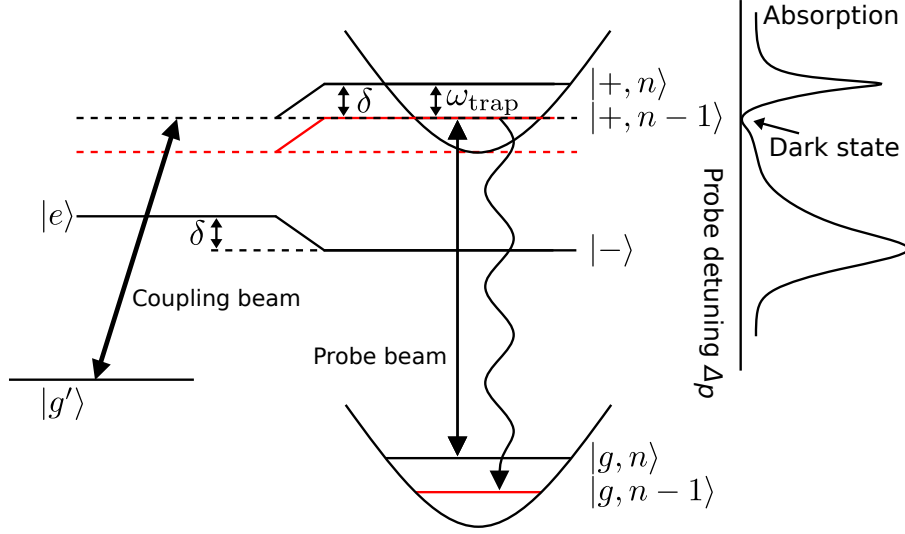


Figure 5.6: Left: EIT cooling transition in a three-level Λ system. A strong coupling beam forms new eigenstates $|+\rangle$ and $|-\rangle$ from the bare atomic ground state $|g'\rangle$ and excited state $|e\rangle$. Here, n denotes the vibrational quantum number for atomic motional state in a harmonic trap with a trap frequency of ω_{trap} . By choosing a suitable intensity for the coupling beam, the spectrum can be engineered such that the transition $|g, n\rangle \rightarrow |+, n-1\rangle$ is enhanced to achieve cooling. Right: Scattering spectrum of a weak probe beam.

Moreover, the change in the kinetic energy of the atom has to be sourced from the recoil energy of the scattered photon to facilitate a sideband transition $|n\rangle \rightarrow |n \pm 1\rangle$. The probability for this motional coupling to occur is characterized by the Lamb-Dicke parameter η , defined as $\eta = |\vec{k}_p - \vec{k}_c| \cos(\phi) a_0$, where \vec{k}_p and \vec{k}_c are the wave vectors of the probe and coupling beams, ϕ is the angle between $\vec{k}_p - \vec{k}_c$ and the motional axis, and a_0 is the position uncertainty of the particle with mass m in the ground state of the harmonic oscillator, given by $a_0 = \sqrt{\hbar/(2m\omega_{\text{trap}})}$.

Under these conditions, the dynamics of the mean vibrational number $\langle n \rangle$ can be described with a rate equation [168]:

$$\frac{d}{dt}\langle n \rangle = -(A_- - A_+)\langle n \rangle + A_+, \quad (5.5)$$

where A_- and A_+ represent the excitation probability for the red and blue sidebands:

$$A_{\pm} = \frac{\Omega_p^2}{\Gamma} \frac{\Gamma^2 \omega_{\text{trap}}^2}{\Gamma^2 \omega_{\text{trap}}^2 + 4[\Omega_c^2/4 - \omega_{\text{trap}}(\omega_{\text{trap}} \mp \Delta_c)]^2}. \quad (5.6)$$

Following Eqn. 5.5, this EIT cooling technique will have a cooling rate of $\eta^2(A_- - A_+)$, with a steady-state vibrational quantum number of $\langle n \rangle = A_+/(A_- - A_+)$.

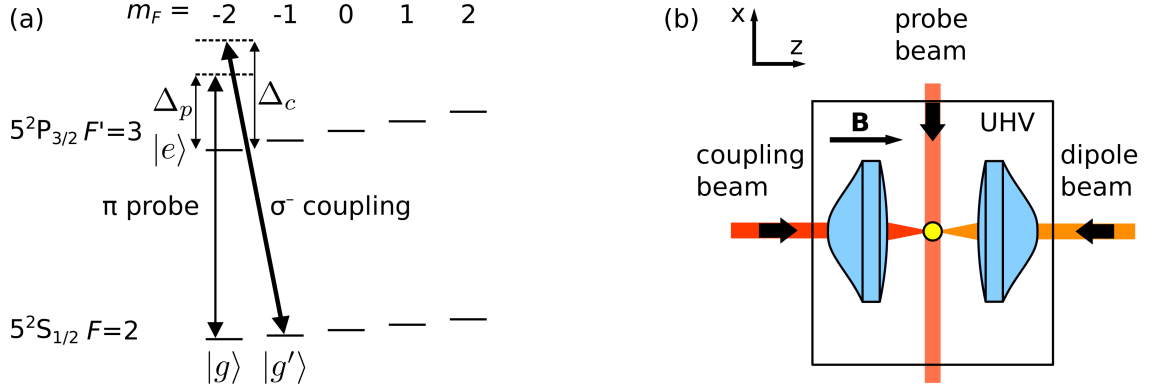


Figure 5.7: (a) Energy levels and transitions in ^{87}Rb used in the cooling experiment. (b) Experimental configuration for the off-resonant EIT cooling process. The probe beam is now set to be orthogonal to the optical axis x to allow for motional coupling.

5.2.2 Implementation

In this part, the Λ configuration is now realized with a σ^- polarised coupling beam connecting sublevel $|g'\rangle \equiv |F=2, m_F=-1\rangle$ of the $5^2\text{S}_{1/2}$ $F=2$ hyperfine ground state to sublevel $|e\rangle \equiv |F'=2, m_{F'}=-2\rangle$ of the $5^2\text{P}_{3/2}$ $F'=2$ hyperfine excited state, and a π polarised probe beam connecting sublevel $|g\rangle \equiv |F=2, m_F=-2\rangle$ of the $5^2\text{S}_{1/2}$ $F=2$ hyperfine ground state to $|e\rangle$, as illustrated in Fig. 5.7(a). Both coupling and probe are blue-detuned from their respective transitions by $\Delta_c = \Delta_p = 2\pi \times 94.5 \text{ MHz} \approx 16 \Gamma$.

In order to attain motional coupling, we require a configuration in which the momentum transferred by light to the atom is non-zero ($\Delta\vec{k} = \vec{k}_c - \vec{k}_p \neq 0$). For this, the direction of the probe beam is altered such that it is sent orthogonal to the coupling beam in a top-down direction, polarized parallel to the bias magnetic field to excite π transitions (see Fig 5.7(b)).

Our FORT traps the atom in a 3-D harmonic oscillator with radial ($\omega_{x/y}$) and axial (ω_z) trapping frequencies ($\omega_{x/y}, \omega_z$) = $2\pi \times (73 \pm 2, 10 \pm 1)$ kHz, deduced from a parametric excitation measurement (refer to Chapter 2.3.5). Accordingly, the associated Lamb-Dicke parameters (η_x, η_z), which quantify the motional coupling, are estimated to be (0.23, 0.59) for our EIT cooling beam geometry.

The experimental sequence is depicted in Fig. 5.8. Similar to the experimental sequence described in the previous part, we start with 10 ms of PGC to bring down the atomic temperature after successful loading of a single atom from the MOT,

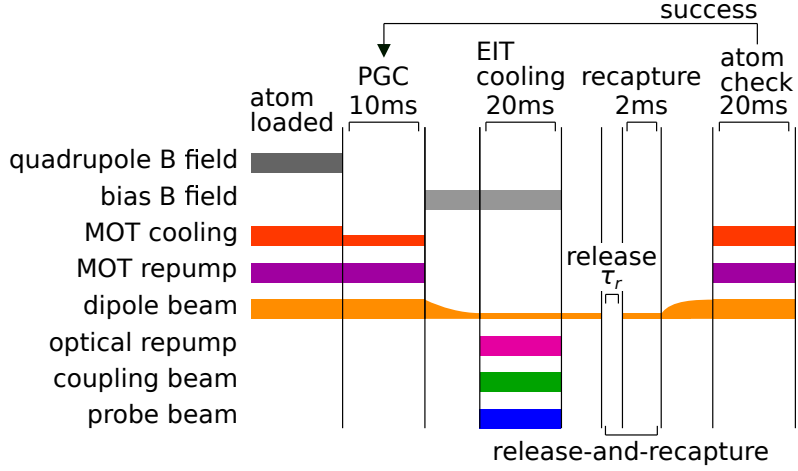


Figure 5.8: Experimental sequence for performing EIT cooling on a single ^{87}Rb atom. The coupling and probe beams are switched on for a duration of 20 ms to apply EIT cooling, followed by a release-and-recapture measurement to quantify the atomic temperature.

followed by a bias magnetic field of 1.44 mT along the FORT beam propagation direction to remove the degeneracy of the Zeeman states. We then apply EIT cooling by switching on the coupling and probe beams for 20 ms to drive the Λ system, a duration chosen arbitrarily but sufficiently long to ensure that the system reaches a steady state. During this cooling process, a weak repumper beam resonant to the D1 line at 795 nm between $5^2\text{S}_{1/2}F = 1$ and $5^2\text{P}_{1/2}F' = 2$ is also switched on to transfer the atom back into the $F = 2$ hyperfine ground state if it spontaneously decays into the $F = 1$ state.

Following that, we employ a “release and recapture” method [92] to quantify the temperature of the single atoms. During this process, the EIT cooling beams are switched off and the atom is released from the trap for an interval τ_r by switching off the FORT beam. Subsequently, the FORT is switched on to recapture the atom and we detect atomic fluorescence by switching on the MOT’s cooling and repumping beams to check the presence of the single atom. We repeat each experiment around two hundred times to obtain an estimate of the recapture probability. Finally, we infer the atomic temperature by comparing the recapture probabilities to Monte Carlo simulations of the trajectories of the single atoms [92].

In the first part of the thermometric experiment, we would like to verify the capability of the two-photon process to either cool down or heat up the single atoms.

CHAPTER 5. FANO SPECTRUM AND COOLING

We apply the EIT cooling by varying the Δ_p and Δ_c of the pair of coupling and probe beams over a range of $\pm 2\pi \times 1$ MHz while fixing Ω_c and Ω_p to $2\pi \times 5.2$ MHz and $2\pi \times 2.0$ MHz, respectively. We choose $\Omega_c = 2\pi \times 5.2$ MHz because this parameter is expected to a Fano resonance shift coinciding with the trap frequency ($\delta = \Omega_{\text{trap}}$ following Eqn. 5.2) that leads to optimal cooling. Here, we fix the release interval to $\tau_r = 30 \mu\text{s}$, empirically determined to yield the largest signal contrast for recapturing measurements from which the temperature can be inferred.

The resulting atomic temperature is shown in Fig. 5.9(a). Cooling and heating effects close to the dressed states for the two-photon process are clearly visible. In comparison, if the conventional PGC technique is used to cool the atoms, they typically show a temperature of $14.7 \mu\text{K}$, indicated by the white shading in the density plot. We observe an effective cooling phenomenon in the anti-diagonal stripe that corresponds to $\Delta_p = \Delta_c$, in agreement with the theoretical prediction. Heating occurs most dominantly around $\Delta_p = \Delta_c + 2\pi \times 250$ kHz, where the blue sideband transitions are preferable.

In the following parts, we will maintain $\Delta_c = 2\pi \times 94.5$ MHz fixed for our EIT cooling parameter. To obtain a more accurate estimation of the atomic temperature, we now deduce a temperature value based on a series of recapturing probabilities for 12 different release intervals ranging between 1 and $80 \mu\text{s}$. We vary the probe detuning Δ_p around Δ_c , as shown in Fig. 5.9(b). We observe the typical asymmetrical Fano profile, with the lowest temperature of $5.7 \pm 0.1 \mu\text{K}$ measured at $\Delta_p = \Delta_c$.

According to [166], optimal cooling is achieved when the dressed state energy shift δ caused by the coupling beam is equal to the trap frequency, $\delta = \omega_{x/y}$, as it maximizes the absorption probability on the red sideband transition. To confirm this behavior, we record the atomic temperature using the same ‘‘release and recapture’’ scheme when scanning the intensity of the coupling beam, keeping $\Delta_c = \Delta_p = 2\pi \times 94.5$ MHz and $\Omega_p = 2\pi \times 2.0$ MHz fixed. The results are depicted as a function of the saturation parameter $s = 2\Omega_c^2/\Gamma^2$ in Fig. 5.10(a). Cooling is observed within the region between $s = 0.5$ and $s = 3$, with the optimal cooling parameter obtained at $s = 1.42 \pm 0.03$ (or $\Omega_c = 2\pi \times (5.06 \pm 0.05)$ MHz). This corresponds to a dressed state energy shift of $\delta = \Omega_c^2/(4\Delta_c) \approx 2\pi \times (68 \pm 1)$ kHz, as introduced in Eqn. 5.3, which is fairly consistent with the radial trap frequency ω_x in our system.

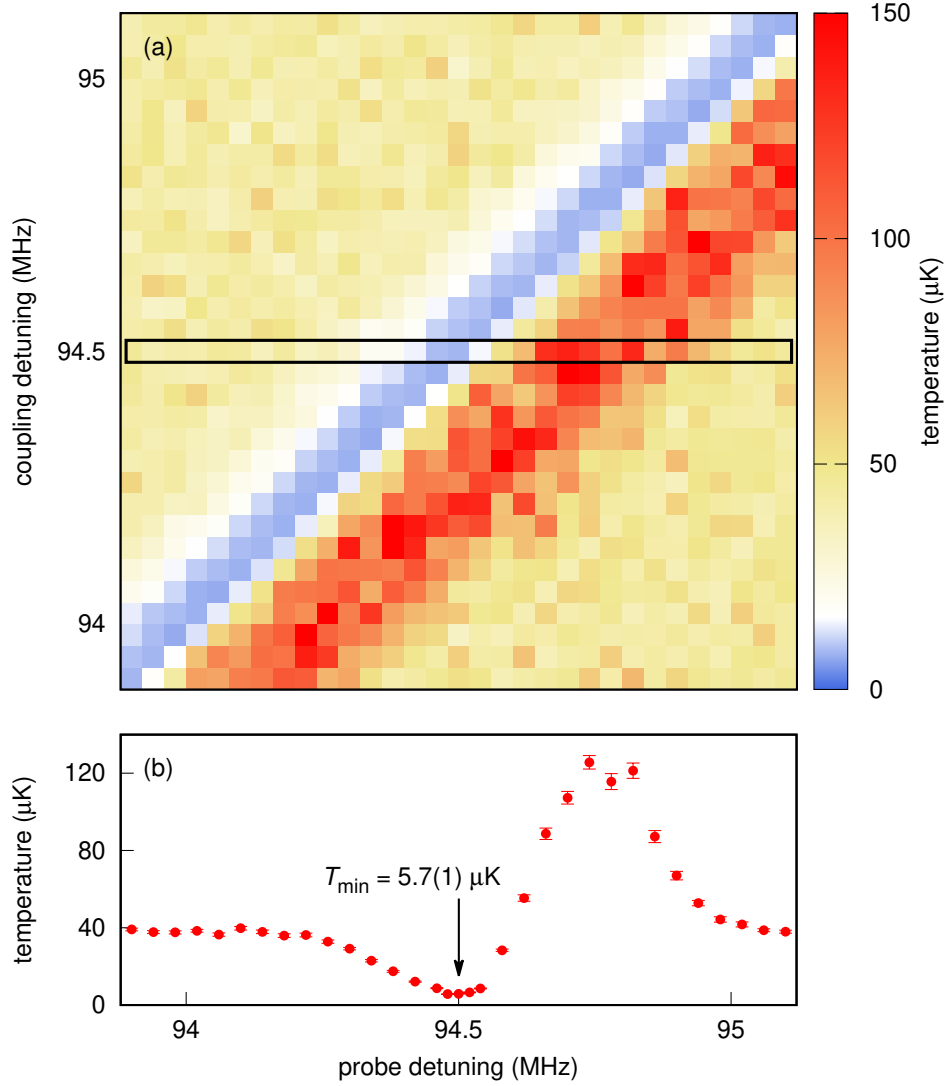


Figure 5.9: (a) Atomic temperature inferred from release-recapturing measurements after 20 ms of EIT cooling at different Δ_c and Δ_p . The anti-diagonal blue band indicates the dark state resonance which has the highest cooling efficiency. (b) Atomic temperature for $\Delta_c = 2\pi \times 94.5$ MHz shows the asymmetrical Fano profile. This Δ_c corresponds to the boxed region in (a).

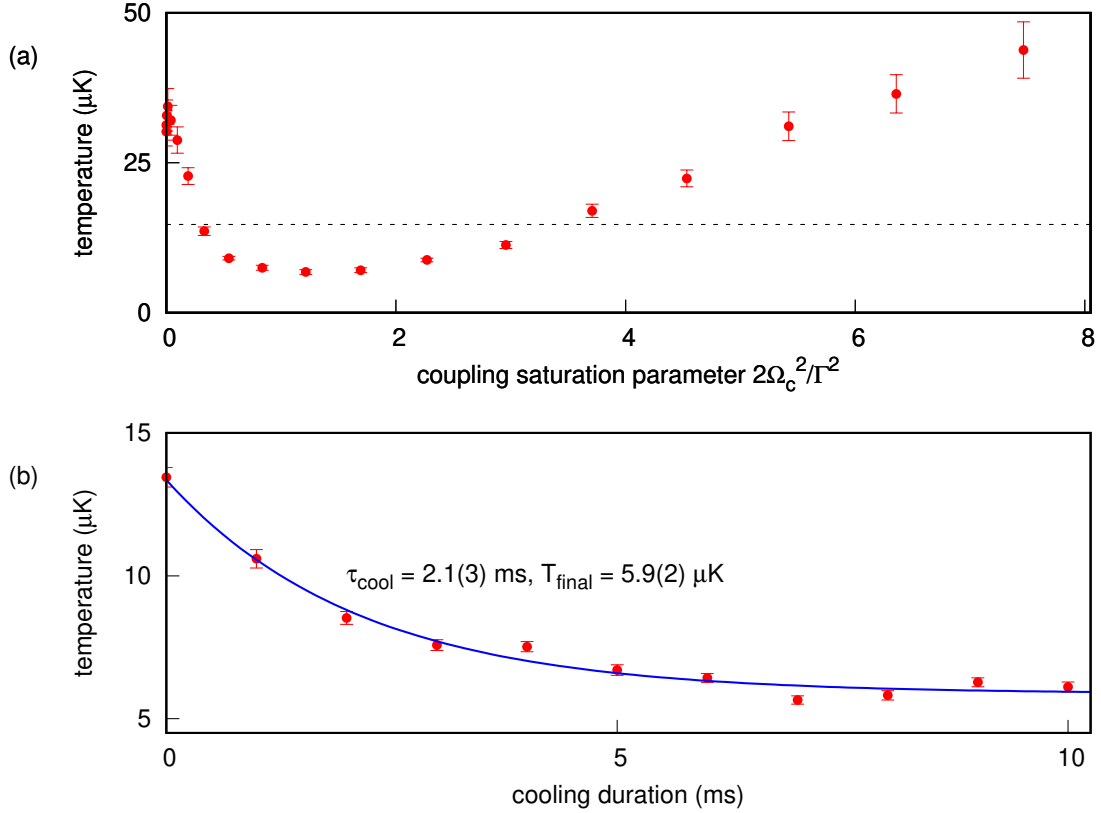


Figure 5.10: (a) Atomic temperature at $\Delta_p = \Delta_c = 2\pi \times 94.5$ MHz for varying Ω_c . We observe an effective cooling for $s = 2\Omega_c^2/\Gamma^2$ between 0.5 and 3, with the optimal cooling around $s = 1.42 \pm 0.03$. The dotted line indicates the initial atomic temperature after PGC of $14.7 \mu\text{K}$. Error bars represent the standard error of binomial statistics accumulated from around 200 repeated runs. (b) Atomic temperature measured after different cooling durations. A cooling time of 2.1 ms and final temperature of $5.9 \pm 0.2 \mu\text{K}$ are extracted from the exponential fit.

It is worth mentioning that we are only able to observe the cooling effect on the radial axis here due to the limitation of the “release-and-recapture” technique. Particularly, a Gaussian optical trap typically has smaller spatial confinement in the radial direction than in the axial direction. Consequently, it is much easier for the atom to escape the trap in the radial direction during the release interval. To gain insights into atomic motion along the axial direction, one would have to consider employing methods such as motional sideband resolving Raman spectroscopy [130, 131] or microwave sideband spectroscopy in a state-dependent trap potential [169].

We then extract the cooling rate by measuring the atomic temperature after a

CHAPTER 5. FANO SPECTRUM AND COOLING

variable time of EIT cooling, as shown in Fig. 5.10(b). Here, we apply the optimal cooling parameters ($\Delta_c = \Delta_p = 2\pi \times 94.5$ MHz, $\Omega_c = 2\pi \times 5.06$ MHz and $\Omega_p = 2\pi \times 2.0$ MHz) to the pair of coupling and probe beams. From an exponential fit to the experimental data, we deduce a $1/e$ cooling time constant of 2.1 ± 0.3 ms and a steady-state temperature of 5.9 ± 0.2 μ K. The measured cooling time constant is about 10 times longer than the theoretical value (0.2 ms) estimated from Eqn. 5.6. Additionally, the mean phonon number inferred from the measured atomic temperature is $\langle n_x \rangle = 1.18 \pm 5$, which is higher than the theoretical value of 0.002 expected for our parameters from the rate equation described in Eqn. 5.6.

These discrepancies are possibly due to unaccounted heating effects originating from scatterings of the strong coupling beam via the $|F = 2, m_F = -2\rangle \leftrightarrow |F' = 3, m_{F'} = -3\rangle$ cycling transition. Moreover, the state $|e\rangle$ we choose here in the $5^2P_{3/2}$ $F'=2$ hyperfine level has a significantly high probability (50 %) to decay into the $5^2S_{1/2}$ $F=1$ hyperfine level, which is decoupled from the pair of EIT cooling beams. Despite the use of a repumper beam to transfer the atom back to the $F = 2$ state, this process introduces a delay as well as additional heating in the cooling sequence. In comparison, the cooling rate for the EIT cooling is 1.9 times slower than the conventional PGC, which has a typical $1/e$ cooling time constant of 1.1 ± 0.1 ms [91].

5.3 Summary

In conclusion, we demonstrate cooling by electromagnetically induced transparency (EIT) for a single neutral atom confined in an optical dipole trap. We resolve the signature Fano profiles in the fluorescence excitation spectrum and also the temperature measurement. A final temperature of less than $6\ \mu\text{K}$ has been achieved with EIT cooling, a factor of two lower than the previous value obtained using the polarization gradient cooling technique.

Finally, the implementation of this relatively simple cooling scheme can potentially diversify the spectrum of techniques accessible for the enhanced manipulation of atomic motion. This technique can be attractive for manipulating motional states of ultracold atoms in optical tweezer arrays.

Chapter 6

Array of two single atoms

This chapter documents some ongoing experimental efforts to increase the number of single-atom traps by using a spatial light modulator, with the hope to achieve the controlled interaction of a few atoms, creating entanglement that can be used in quantum computation. We also discuss a few limitations related to trap distance and trap size for the formation of multiple traps. After implementing a control sequence that allows deterministic loading of the two single atoms, an intensity correlation measurement is performed for the single photon interference from the two single atoms.

6.1 From one to few atoms

In 1954, Dicke predicted that the behavior of an ensemble of emitters when interacting with a quantum mode of light is distinct from that of the individual emitters [170]. In this picture, the quantum state of an ensemble is better described by the collective states (super-radiant or sub-radiant), arising from the constructive or destructive interference of transition pathways. Generally, the discussion is constrained to an ensemble of atoms having a spatial extent smaller than the wavelength of light.

For an ensemble of atoms distributed over distances longer than the wavelength of light, previous theoretical studies have demonstrated that collective emission is strongly dependent on the geometric arrangement of the emitters [73, 171–173]. With better control over the position and motion of emitters, there are increasing experimental efforts that investigate the collective radiation in free space, including cold atomic clouds [174–176], trapped ions [177], and laterally arranged quantum

dots [178]. An ordered array of optically trapped neutral atoms could also be an interesting platform for new exploration in this direction.

6.1.1 Wavefront modulation

We trap single atoms in an array of holographic dipole traps formed by a spatial light modulator (SLM) [179, 180]. Particularly, a phase-modulating liquid-crystal SLM is employed to imprint a phase profile $\Phi(x, y)$ onto the FORT beam, which initially has a Gaussian amplitude profile $E_0(x, y)$. After the FORT beam is focused down by the aspheric lens, the intensity distribution in the focal plane is then determined by the squared modulus of the 2D Fourier transform of $E_0(x, y)e^{i\Phi(x, y)}$, which is a consequence of Fraunhofer diffraction [181].

To generate a suitable phase pattern for a trap array with arbitrary geometries, a diverse class of iterative phase retrieval algorithms has been investigated, including conjugate gradient minimization [182], mixed-region amplitude freedom [183, 184], and the Gerchberg–Saxton algorithm [185, 186] (refer to [187] for a comparison of these different techniques). However, in this thesis we mainly focus on the simplest array geometry containing only a pair of single atoms, without the need for rearranging the trap position. Therefore, we employ a simpler approach by directly taking the phase component of the inverse Fourier transform of a Dirac-delta function at $\pm d/2$ on the image plane (see Fig. 6.1(a)):

$$\begin{aligned}\Phi(\vec{r}) &= \arg \left[\mathcal{F}^{-1} \left[\delta \left(k_x - \frac{kd}{2f}, k_y \right) + \delta \left(k_x + \frac{kd}{2f}, k_y \right) \right] \right] \\ &= \arg \left[\exp \left(i \frac{d}{2f} kx \right) + \exp \left(-i \frac{d}{2f} kx \right) \right] \\ &= \begin{cases} 0, & x \in \left[(2N - \frac{1}{2}) \frac{f\lambda}{d}, (2N + \frac{1}{2}) \frac{f\lambda}{d} \right] \text{ for integer } N, \\ \pi, & x \in \left[(2N + \frac{1}{2}) \frac{f\lambda}{d}, (2N + \frac{3}{2}) \frac{f\lambda}{d} \right] \text{ for integer } N, \end{cases} \end{aligned} \quad (6.1)$$

where d is the trap spacing, k is the wave number of the dipole light, and f is the focal length of the lens, (k_x, k_y) corresponds to the angular spectrum of the input field with $(k_x, k_y) = (kx'/f, ky'/f)$ for (x', y') the coordinate on the image plane, and $\vec{r} = (x, y)$ is the coordinate on the object plane.

This phase transformation $\Phi(\vec{r})$ is effectively a square wave function with a period of $2f\lambda/d$. Notably, this phase pattern is equivalent to a diffraction grating with

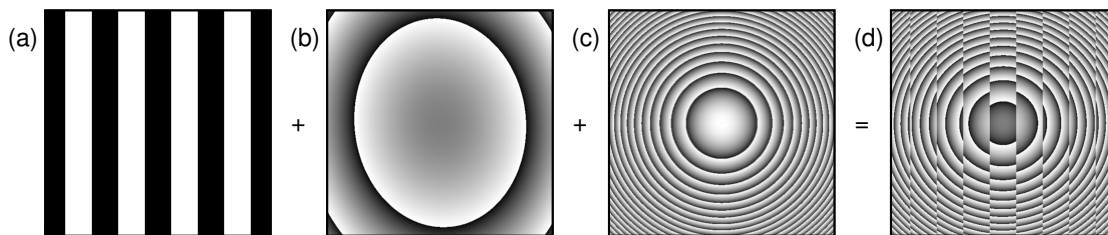


Figure 6.1: Phase patterns employed on the spatial light modulator (SLM). (a) The grating pattern following Eqn. 6.1 to create two traps. (b) The corrective phase pattern, provided by the SLM manufacturer, to address non-flatness on the surface of the SLM. (c) The Fresnel lens pattern to correct for chromatic shift, as described in Chapter 2.3.2. (d) The combined phase pattern composed of the previous three contributions.

a grating period of $2f\lambda/d$, or equivalently first-order diffraction angles of $\pm d/2f$. Due to the simplicity of this phase function, this technique can also be implemented using physical phase plates or diffraction gratings.

Ideally, the phase pattern employed above contains only the odd diffraction orders, with diffraction efficiencies of $4/\pi^2 \approx 40.5\%$, $4/(3\pi)^2 \approx 4.5\%$, and $4/(5\pi)^2 \approx 1.6\%$ for the diffraction of first, third, and fifth order, respectively. Accounting for losses on the SLM, we find that we typically need an input FORT beam power of about 20 mW for trap depth of $k_B \times 1$ mK in the two-atom configuration. Compared with the previous demonstration in [179] that requires about $5N$ mW of power for N dipole traps with the same trap depth, our system utilizes roughly twice as much optical power. This difference can be attributed to a larger focused beam profile and higher optical losses. Nevertheless, the optical power requirement still remains reasonable, even for commercial 850-nm laser diodes. In fact, we can easily increase the trap number to $N = 4$ in a square array configuration with the available optical power in the FORT beam. We restrict to the case of $N = 2$ to ensure high fluorescence collection for both the single atoms into single mode fiber and also deterministic loading of the trap array.

6.1.2 Implementation

Figure 6.2 shows the schematic for the optical setup to trap atoms in a tweezer array. The collimated FORT beam (horizontally polarized) with a beam radius of

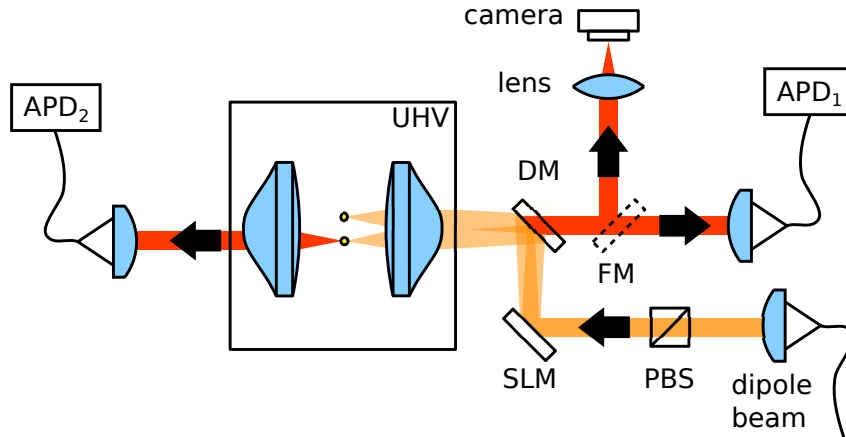


Figure 6.2: Optical setup for interfacing a pair of single atoms with light. A pair of single atoms are held by the diffracted tweezer array focused down by the high NA lens. The scattering of individual atoms is coupled into a single-mode fiber. DM: dichroic mirror, FM: flip mirror, SLM: spatial light modulator, PBS: polarizing beamsplitter, APD: avalanche photodetector, UHV: ultra-high vacuum.

2.7 mm illuminates the SLM that has an active area of $12.8 \times 12.8 \text{ mm}^2$ and a spatial resolution of 512×512 pixels. The SLM then imprints a phase pattern to form a pair of traps following Eqn. 6.1, as well as the Fresnel lens hologram to correct for the achromatic shift as discussed in Chapter 2.3.2.

Next, the modulated FORT beam is focused down by the high NA aspheric lens, after a propagation distance of about 1 m between the SLM and the aspheric lens. This relatively long propagation distance is a consequence of the optical elements in place for the collection of 780-nm atomic fluorescence. This can be detrimental for more complex trap geometries due to beam clippings and aberrations for off-axis beams focusing on the aspheric lens. While this problem is not yet a limitation for a simple two-atom trap, for future iterations we would have to consider designs such as a $4f$ optical system that conjugates the SLM plane with the aspheric lens to avoid this problem [188].

Here, we collect the scattered fluorescence from single atoms in each dipole trap into individual single-mode fibers for APD detection. Accounting for the collection mode of the collimating lens for the single-mode fiber, we expect there is less than 1% scattered light collected by the other single-mode fiber for atomic spacing $d > 1.5\lambda$. Hence, this arrangement enables the spatial resolution of the two traps by the two APDs.

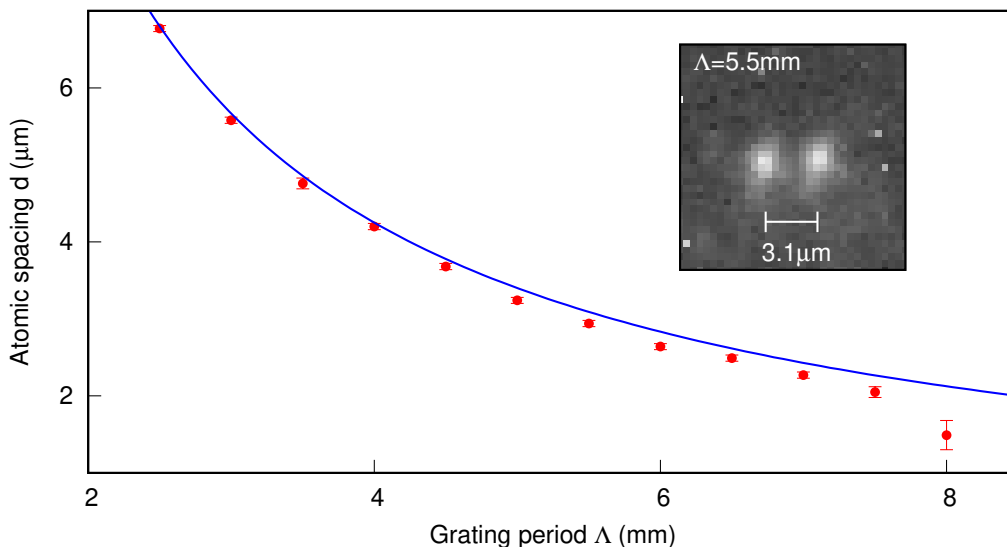


Figure 6.3: Distance between the pair of single atoms (d) as a function of wavefront modulation period (Λ). The blue solid line is the calculated trap separation following Eqn. 6.1, assuming the input field is a plane wave. The atomic spacing starts to deviate from the expected results for a modulation period longer than the FORT beam diameter $2w = 5.4$ mm. Inset: Exemplary camera image of two single atoms at $\Lambda = 5.5$ mm, integrated over 1 s. We perform a Gaussian fit to the images to extract the atomic spacing d .

Measuring atomic spacing

In this first part of the experiment, we would like to confirm that the atomic spacing d varies inversely with the SLM modulation period Λ according to Eqn. 6.1. To do this, we overlap the magneto-optical trap with the SLM-diffracted trap array, allowing the loading of single atoms. We then record fluorescence images using the single-photon imaging camera along the lens axis with an exposure time of 1 s. This exposure time is chosen to be much longer than the reciprocal of the loading rate (on the order of 100 ms) to ensure atom loadings and fluorescence scattering from both of the traps. Next, we extract the atomic spacing from the two fluorescence centroids by performing a Gaussian fit to the camera image. We repeat this at various modulation periods applied to the SLM.

Figure 6.3 shows the deduced atomic spacing as a function of imprinted grating modulation period Λ . The blue solid line represents the theoretical value for the trap spacing calculated from $d = 2f\lambda/\Lambda$. For $\Lambda \leq 5$ mm, the measured atomic spacing agrees very well with the theoretical value, with a discrepancy of less than 5%.

Notably, there is an increasing discrepancy between the theoretical values and the measured values for $\Lambda > 5$ mm, close to the beam diameter of the collimated FORT beam ($2w_{\text{in}} = 5.4$ mm). This can be understood as the FORT beam can no longer experience the “periodicity” of the diffraction grating imprinted by the SLM, limited by its finite beam size.

The electric field distribution in the image plane also offers an intuitive explanation for this observation. We can approximate the electric field in the focal plane by

$$E(x', y') = \frac{2E_0}{\pi} e^{-y'^2/w_f^2} \left(e^{-(x' - \frac{f\lambda}{\Lambda})^2/w_f^2} + e^{-(x' + \frac{f\lambda}{\Lambda})^2/w_f^2} \right), \quad (6.2)$$

where (x', y') is the coordinate on the image plane, w_f is the focal beam waist, and $2E_0/\pi$ relates to the diffraction efficiency from an initial Gaussian with a field amplitude of E_0 . For $f\lambda/\Lambda \gg w_f$, the two Gaussian profiles are approximately centered at $\pm f\lambda/\Lambda$, leading to $d = 2f\lambda/\Lambda$. On the other hand, for $f\lambda/\Lambda \lesssim w_f$, the two Gaussian profiles will interfere constructively around $x' = 0$, shifting the points of maximal intensity closer to $x' = 0$. The constructive interference arises from the choice of the phase pattern in Eqn. 6.1, with the assumption that the dipole light fields are in phase. As a result, the trap spacing d will be smaller than the expected value $f\lambda/\Lambda$ for larger Λ , in agreement with the behavior we see in Fig. 6.3.

From the expression in Eqn. 6.2, we can show that the pair of traps cannot be formed for $\Lambda \geq \sqrt{2\pi}w_{\text{in}} \approx 12$ mm due to diffraction limit. However, experimentally we are not able to observe the loading of two atoms starting from $\Lambda > 8$ mm. This is mostly because the potential barrier between the two traps is also decreasing for larger Λ . For the potential barrier smaller than the MOT temperature (typically around $100 \mu\text{K}$), the single atoms can have enough kinetic energy to escape the potential barrier, leading to the collisional blockade of both of the two dipole traps.

6.1.3 Triggering of a pair of single atoms

In a typical experimental run, we choose to operate at a modulation period Λ of 5.5 mm, corresponding to an atomic spacing of $d \approx 3.1 \mu\text{m}$ to avoid problems associated with small atomic spacing (more details are described in Chapter 6.1.4). With this parameter, we can ensure successful trapping of single atoms in both the two dipole traps by experimental sequence branching conditioned on the APD

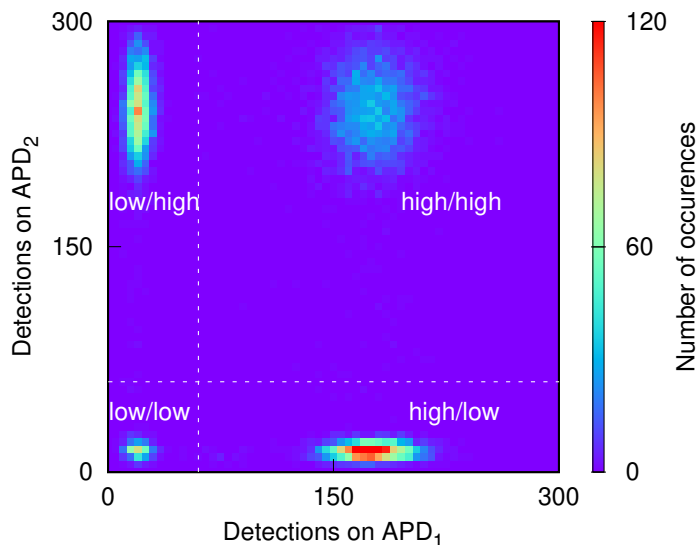


Figure 6.4: Two-dimensional histogram of detected events on APD₁ and APD₂ over 40 ms, which spatially resolve the cooling fluorescence scattered by single atoms in trap 1 and trap 2, respectively. We observe four clusters in the photodetection distribution, which corresponds to the cases where two single atoms are present in both traps (high/high), one atom in trap 1 and no atom in trap 2 (high/low), no atom in trap 1 and one atom in trap 2 (low/high), and no atom in both traps (low/low). The dotted lines indicate the triggering threshold for single atom loading events.

counts, similar to Chapter 2.3.3.

We start with forming a cold cloud of ^{87}Rb atoms using a MOT, which overlaps with the SLM-diffracted dipole trap array. Once an atom is loaded into each dipole trap of the array, the count rate on the associated single-mode fiber-coupled APD will increase from 200 s^{-1} (APD dark count rate) to 4000 s^{-1} . This fluorescence is collected by our experimental control system during a qualifying time window of 40 ms.

Figure 6.4 shows the typical two-dimensional histogram of the cooling fluorescence from the pair of single atoms, as seen on the two APDs. We observe four clusters in the photodetection distribution, which corresponds to the cases where two single atoms are present in both traps (high/high), one atom in trap 1 and no atom in trap 2 (high/low), no atom in trap 1 and one atom in trap 2 (low/high), and no atom in both traps (low/low). In the following parts, we choose a triggering threshold of 1500 s^{-1} (60 counts in 40 ms) on both two APDs to confirm the presence of the pair

of single atoms.

6.1.4 Problems with small atomic spacing

For an atomic spacing sufficiently small ($\approx \lambda$), it might become feasible to observe mechanisms related to dipole-dipole coupling between single atoms. For that reason, we started operating the trap array with the smallest atomic spacing we can achieve ($\approx 2\lambda$), employing a SLM modulation period Λ of 8 mm. Unfortunately, instead of observing the desired dipole-dipole coupling, we encountered a number of unexpected effects stemming from imperfections in atom trapping. We document here the problems that arise from operating the trap array in the regime where the atomic spacing is close to the trap beam waist.

Atom hopping

We notice that whenever we initialize the system to have exactly one single atom in each dipole trap, it is very likely to lose both single atoms after a probing sequence. This phenomenon becomes particularly pronounced when the frequency of the probe beam is set to be on-resonant with the atomic transition. We suspect that this is caused by a single atom escaping from one dipole trap to the other dipole trap during the probing process. Consequently, a light-induced collisional blockade [84] will result in two-atom loss.

To confirm this hypothesis, we run the following experimental sequence. We prepare the system to have one atom in one of the traps (trap 1), and no atom in the other trap (trap 2). Both dipole traps are set to have the same trap depth of $U_0 = k_B \times 0.88$ mK, separated by $1.5 \mu\text{m}$. After a PGC sequence, we apply a bias magnetic field to remove the Zeeman degeneracy. The atom is then optically pumped to the $F = 2, m_F = -2$ Zeeman sublevel, followed by a $600\text{-}\mu\text{s}$ nearly resonant probe beam orthogonal to the optical axis. Finally, we switch on the MOT cooling and repumper beams and record the fluorescence scattering on the fiber-coupled APDs to detect the presence of the atom in both traps.

The probability of finding an atom in either trap for varying probe detuning is shown in Fig. 6.5. For the probe frequency that is detuned far away from the atomic resonance ($\Delta_p \gg \Gamma$), the single atom remains in trap 1 after the illumination. Moreover, at resonance, we notice a decrease in the probability of the atom staying

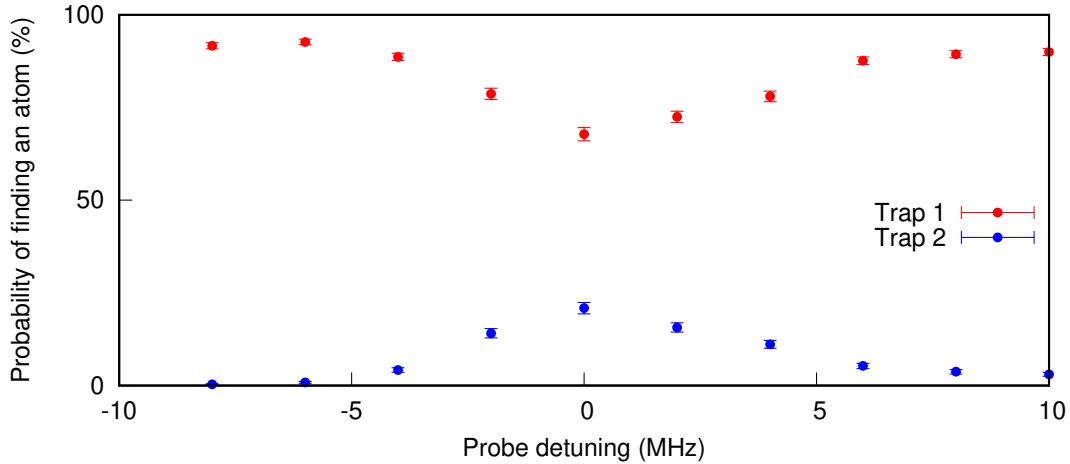


Figure 6.5: Probability of detecting a single atom in either dipole trap after illumination with a nearly resonant probe beam. We prepare a single atom in trap 1 and no atom in trap 2. The atom is then illuminated with a weak probe beam with varying detunings for $600 \mu\text{s}$. We observe that there is a high chance ($21 \pm 2\%$) for the atom to be transferred into trap 2 from trap 1 at the end of the probing process, due to recoil heating of the probe field. Error bars represent the standard error of binomial statistics accumulated from around 1200 repeated sequences.

in trap 1. Interestingly, the loss of the single atom in trap 1 is always correlated with the presence of an atom in trap 2, indicating that the atom has been transferred into trap 2 from trap 1.

The observation above can be explained by recoil heating induced by the probe beam. We consider the atom to be trapped in a symmetric double-well potential with a trap depth of U_0 and a potential barrier of ΔU . For N scattering events, the atomic temperature follows $T = T_0 + NT_r$, where T_0 is the initial atomic temperature and T_r is the recoil temperature, given by $T_r = \hbar^2 k^2 / mk_B \approx 0.36 \mu\text{K}$ for mass of ^{87}Rb atom $m = 1.45 \times 10^{-25} \text{ kg}$ and 780-nm light. Assuming a Boltzmann distribution, the probability of a single atom having energy higher than the potential barrier can be calculated from

$$\begin{aligned}
 P(E > -U_0 + \Delta U) &= \frac{e^{-U_0/k_B T}}{k_B T} \int_{-U_0 + \Delta U}^{\infty} e^{-E/k_B T} dE \\
 &= e^{-\Delta U/k_B T}.
 \end{aligned} \tag{6.3}$$

With the fluorescence scattering rate of $3 \times 10^5 \text{ s}^{-1}$ estimated from the photon detection rate on the APD, we infer that the potential barrier is approximately

$\Delta U = k_B \times (120 \pm 20) \mu\text{K}$. We anticipate that this measurement can be utilized as a technique to discern sub-wavelength features in a tightly focused optical trap.

An interesting question we can ask is how close are we to observing a quantum tunneling effect of a single atom between two traps. To explore this phenomenon, we examine the tunneling coupling $J = \langle \psi_1 | \hat{H}_{\text{sp}} | \psi_2 \rangle / \hbar$, where ψ_1 (ψ_2) is the localized state in trap 1 (2), and \hat{H}_{sp} is the single particle Hamiltonian containing kinetic and double-well potential energy terms. This concept is a standard exercise in variational methods in quantum mechanics textbooks [189, 190]. For an atom with mass m in a symmetric double well potential with a trap spacing of d and trap barrier of ΔU , the tunneling coupling J is given by

$$J \approx \frac{16}{\sqrt{\pi}} \left(\frac{2 \Delta U^3}{\hbar^2 m d^2} \right)^{\frac{1}{4}} e^{-(\sqrt{2m \Delta U} d)/(6\hbar)}. \quad (6.4)$$

Unfortunately, with the current experimental parameters ($\Delta U \approx k_B \times 120 \mu\text{K}$ and $d = 1.5 \mu\text{m}$), the tunneling coupling $J/(2\pi)$ is expected to be less than 10^{-16} Hz, indicating that the tunneling effect occurs at a small probability within the experimental timescale. To address this limitation, we would have to implement an adiabatic ramp down of the dipole beam power to achieve a trap barrier on the order of $k_B \times 1 \mu\text{K}$ for a tunneling coupling of $J/(2\pi) \approx 400$ Hz, as demonstrated in a previous study [191].

Formation of an additional dipole trap

The issue of trap hopping induced by heating, as observed in the previous part, can be circumvented by increasing the FORT beam power to elevate the potential barrier between the two dipole traps. Unexpectedly, we observe that this approach actually introduces a new problem: the formation of an additional out-of-focal-plane dipole trap.

Similar to the previous part, we operate the double well trap at a spacing of $1.5 \mu\text{m}$. However, we increase the trap depth of the individual dipole trap to $U_0 = k_B \times 2.4 \text{ mK}$, which corresponds to a potential barrier of $\Delta U = k_B \times 600 \mu\text{K}$. With this increased trap power, the trap hopping problem is significantly suppressed. As we attempt to detect the presence of the two atoms in the dipole traps based on cooling fluorescence counts, we occasionally detect an atom loading with a lower scattering rate (1500 counts/s compared to the expected 5000 counts/s). Another

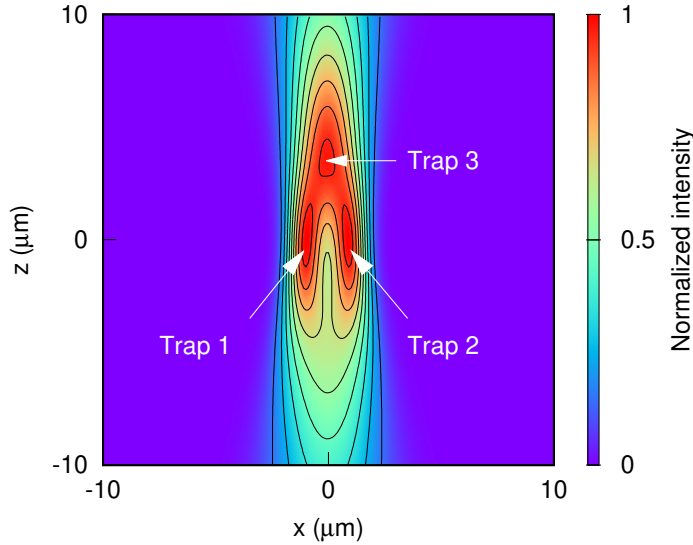


Figure 6.6: Calculated intensity profile around the focus using the trapping parameters. Contour lines represent normalized intensities ranging from 0.1 to 0.9, relative to the maximum intensity in the graph. Here, the optical axis aligns with the z direction and the x -axis refers to the radial direction orthogonal to the optical axis. The tweezer beam array interferes constructively at about $5 \mu\text{m}$ behind the focal plane, forming another local minimum in the dipole potential field.

peculiar observation is that this atom loading with a lower scattering rate appears in both the single-mode fiber-coupled APDs.

This phenomenon has troubled us for quite some time. Initially, we suspected that these atom loadings might be linked to classes of single atoms with kinetic energy higher than the potential barrier, leading to a single atom moving between the two dipole traps. However, this seems highly improbable given the atomic temperature inferred from a release-recapture measurement. Additionally, the polarization gradient cooling does not appear to have any impact on the observed behavior.

We finally have a better understanding of this issue after we investigate the atomic fluorescence along the optical axis z . To do this, we displace the imaging lens before the camera to image the atomic fluorescence from a variable object plane. We observe single atoms trapped at approximately $z = 5 \mu\text{m}$ away from the focal plane. Further examination also validates that single atoms in this additional dipole trap correlate with the atom loading event with a lower scattering rate.

We speculate that this is caused by constructive interference of the diffracted

trapping beam. To confirm this conjecture, we perform a calculation for the trapping light intensity under paraxial approximation around the focal region, as shown in Fig. 6.6. Notably, the density plot for the trapping beam intensity profile reveals that a new intensity maximum is formed about $5 \mu\text{m}$ away from the focal plane, in agreement with our observation. This local maximum can reach approximately 90% of the peak intensity observed for the pair of dipole traps.

Using ray optics, we can demonstrate that this constructively interfering spot is in fact the image of the SLM plane formed through the aspheric lens. Consequently, the position of this spot is determined by the distance between the SLM and the aspheric lens L . The most direct method to eliminate this additional spot is to shift this spot significantly away (a few Rayleigh ranges away) from the dipole trap plane by reducing L . This would require positioning the SLM very close to the vacuum chamber, which is not very feasible due to the presence of existing fluorescence collection optics. Another alternative would be to place the SLM in a $4f$ optical configuration to conjugate the SLM plane to the aspheric lens plane [188]. It is also possible to bypass this problem by implementing a more complex phase modulation calculated from a multiplane Gerberch-Saxton algorithm [192].

6.2 Towards two-atom entanglement

The experimental setup we have here closely resembles what some previous proposals suggest to create entangled atomic states [193]. We consider a pair of atoms (denoted as 1 and 2) described by a three-level system, with an upper level $|e\rangle$ connecting two long-lived ground states $|g'\rangle$ and $|g\rangle$, as presented in Fig. 6.7(a). An atom in the $|e\rangle$ upper level can decay to the $|g\rangle$ state and $|g'\rangle$ state by emitting a photon with probability p and $1 - p$, respectively. The scheme starts from preparing both the atoms in the state $|g', g'\rangle$. We then apply an excitation on the transition $|g'\rangle \rightarrow |e\rangle$, followed by a probabilistic spontaneous decay of a single photon on the $|e\rangle \rightarrow |g\rangle$ transition. The state of each atom and the photonic mode associated with the $|e\rangle \rightarrow |g\rangle$ transition can be written as

$$|\psi_j\rangle = \sqrt{1-p}|g'_j, 0\rangle + \sqrt{p}|g_j, 1\rangle, \quad (6.5)$$

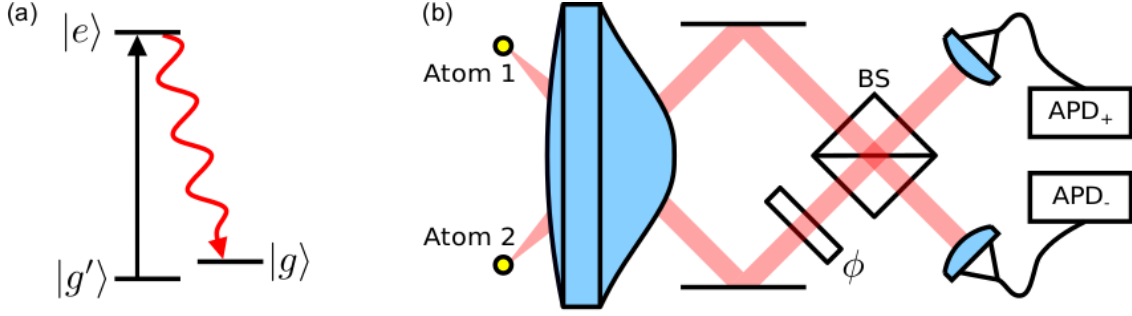


Figure 6.7: (a) Levels and transitions used for generating entanglement between two atoms by a single photon detection. (b) Schematic of the experimental setup for entanglement generation by a single photon detection. Fluorescence emitted by the two atoms is overlapped using a beamsplitter (BS) before the detection on an avalanche photodiode (APD). A phase shifter ϕ represents the relative phase acquired by the spontaneously emitted photons on their way to the beamsplitter, which sets the phase of the two-atom entangled state $(|gg'\rangle + e^{i\phi}|g'g\rangle)/\sqrt{2}$.

where $j = 1, 2$ is the index for the atom. The photon emitted from the $|e\rangle \rightarrow |g'\rangle$ transition is disregarded here by choice.

For instance, we can choose the two ground states to be Zeeman sublevels of the $5^2S_{1/2}$ hyperfine ground level of ^{87}Rb atom, $|g'\rangle = |F = 2, m_F = -2\rangle$ and $|g\rangle = |F = 2, m_F = -1\rangle$ without loss of generality. The excited state $|e\rangle$ can be chosen to be $|F' = 3, m_{F'} = -2\rangle$ of the $5^2P_{3/2}$ manifold. Consequently, we suppose the emitted photons are collected along the quantization axis, π -polarized light from the $|e\rangle \rightarrow |g'\rangle$ transition will not be collected and can be traced out.

Now if we look at the total state of the full system of two atoms and light mode, accounting for the relative phase ϕ acquired by the spontaneously emitted photons, we have

$$\begin{aligned}
 |\psi_{\text{total}}\rangle &= (\sqrt{1-p}|g'_1, 0\rangle + \sqrt{p}|g_1, 1\rangle) \otimes (\sqrt{1-p}|g'_2, 0\rangle + e^{i\phi}\sqrt{p}|g_2, 1\rangle) \\
 &= (1-p)|g'_1, g'_2, 0\rangle + \sqrt{p(1-p)}|g_1, g'_2, 1\rangle \\
 &\quad + \sqrt{p(1-p)}e^{i\phi}|g'_1, g_2, 1\rangle + pe^{i\phi}|g_1, g_2, 2\rangle.
 \end{aligned} \tag{6.6}$$

Indistinguishability of the photons from the two atoms can be achieved by overlapping their corresponding spatial modes with a beam splitter (see Fig. 6.7(b)). Consequently, by post-selecting the cases where a single photon is detected on the

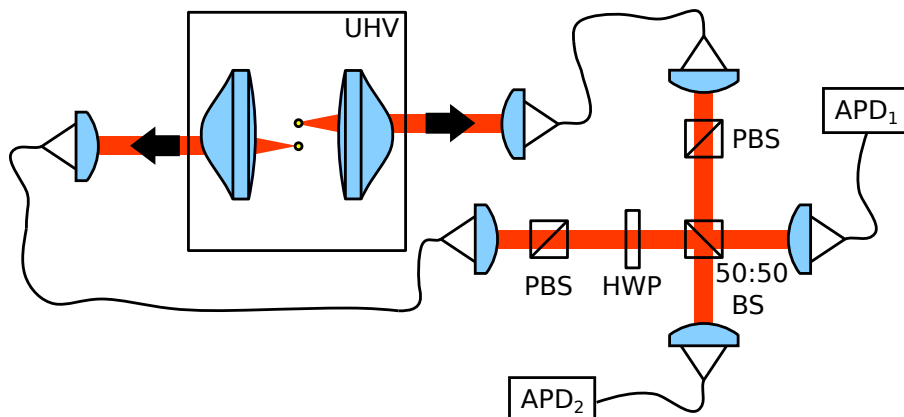


Figure 6.8: Optical setup to measure intensity correlation of single photon interference from two single atoms. A pair of single atoms are illuminated with continuous cooling light. The cooling fluorescence is collected by the high NA lenses and combined by a 50:50 beamsplitter for an intensity correlation measurement. BS: beamsplitter, HWP: half-wave plate, PBS: polarizing beamsplitter, APD: avalanche photodetector, UHV: ultra-high vacuum.

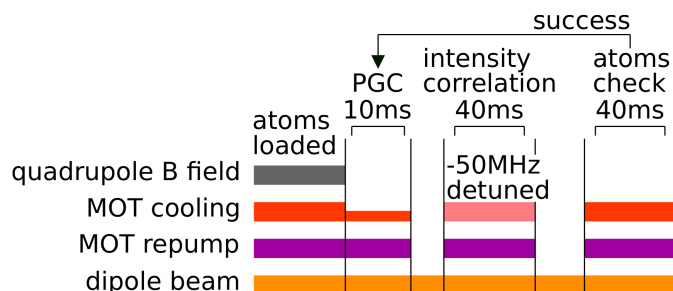


Figure 6.9: Experimental sequence for measuring the intensity correlation of single photon interference from two single atoms. The pair of single atoms is illuminated with weak cooling beams red-detuned by 50 MHz for a duration of 40 ms, during which an intensity correlation measurement is performed with the atomic fluorescence.

APDs, the two-atom state is projected onto an entangled state:

$$|\psi_{\text{total}}\rangle = \frac{1}{2} \left(|g_1, g_2'\rangle + e^{i\phi} |g_1', g_2\rangle \right). \quad (6.7)$$

Such an entanglement scheme was first demonstrated using a pair of Barium ions in [194]. We are interested in assessing the feasibility of implementing a similar scheme with a pair of optically trapped ^{87}Rb atoms.

6.2.1 Preliminary coalescence measurement

One important criterion for the entanglement scheme mentioned above, as well as many quantum processing applications, hinges on the indistinguishability of the emitted single photons. In this part, we attempt to measure the indistinguishability of the fluorescence scattered by a pair of single atoms by using the coalescence phenomenon [195]. In particular, two single photons with the same spectral, spatial, and polarization properties will bunch together when arriving simultaneously on two different input ports of a beam splitter. This in turn will manifest as a drop in the coincidence rate at the outputs of a beam splitter in a two-photon interference Hong-Ou-Mandel measurement.

Figure 6.8 shows the optical setup to measure the intensity correlation of single photon interference from two single atoms. Upon successful trapping of a pair of single atoms in the dipole trap array from the MOT, we start with 10 ms of PGC to bring down the atomic temperature. We then illuminate the pair of single atoms with the weak off-resonant (-50 MHz detuned from the $5^2S_{1/2} F = 2 \leftrightarrow 5^2P_{3/2} F' = 3$ transition) cooling beams for a duration of 40 ms. The scattered light from each single atom is then projected into horizontal polarizations (in parallel) before being combined with a 50 : 50 beam splitter. The outputs of the beam splitter are then directed to APDs for intensity correlation measurements. To ensure the distinguishability of the scattered photons from the atom pair, we repeat the measurement again after rotating the polarization of one beam path to be vertical using a half-wave plate (orthogonal polarizations). The experimental sequence is depicted in Fig. 6.9.

The results of the second-order intensity correlation measurements are shown in Fig. 6.10. Both of the two measurements are integrated over 12 hours for an average coincidence count of 90 in time bins of 1-ns width. We immediately observe an oscillatory pattern from the intensity correlations due to Rabi oscillation between the hyperfine states $5^2S_{1/2} F = 2$ and $5^2P_{3/2} F' = 3$. We infer a Rabi frequency of around $2\pi \times 55$ MHz and $2\pi \times 50$ MHz for the parallel and orthogonal polarizations, respectively. This is because we lower the cooling beam intensity from measurement (a) to (b), as we discover that the cooling beam power used in measurement (a) is not optimal. The cooling beam power is high enough to potentially cause recoil

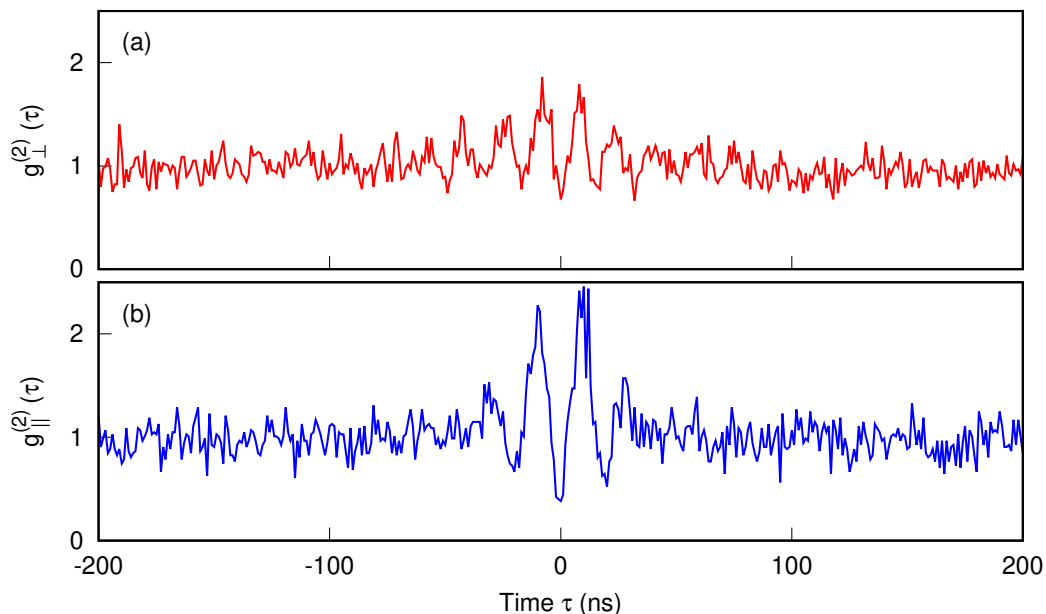


Figure 6.10: (a) Correlation of the interference for orthogonal polarizations. We observe a $g_{\perp}^{(2)}(\tau = 0) = 0.68 \pm 0.09$. (b) Correlation of the interference for parallel polarizations. A reduction in coincidences around $\tau = 0$ is observed for parallel polarizations with $g_{\parallel}^{(2)}(\tau = 0) = 0.38 \pm 0.09$.

heating and consequently lower the trap lifetime.

In theory, given that the scattering of single photons from the two atoms is independent, the expected $g_{\perp}^{(2)}(\tau = 0)$ is 0.5 (the two photons are uncorrelated). When the two photons are projected to the same polarization mode, the expected $g_{\parallel}^{(2)}(\tau = 0)$ is 0, since they should be completely indistinguishable. This allows the two-photon interference visibility to be defined as [196]

$$V = \frac{g_{\perp}^{(2)}(\tau = 0) - g_{\parallel}^{(2)}(\tau = 0)}{g_{\perp}^{(2)}(\tau = 0)}, \quad (6.8)$$

which describes the mode overlap of the single photons at the two input ports of the beam splitter.

In our measurements, the anti-bunching dip for parallel polarizations ($g_{\parallel}^{(2)}(\tau = 0) = 0.38 \pm 0.09$) is indeed lower than that for orthogonal polarizations ($g_{\perp}^{(2)}(\tau = 0) = 0.68 \pm 0.09$), indicating that photons from the two single atoms have a nonzero coalescence probability. However, the measured $g^{(2)}(\tau = 0)$ for both cases are significantly higher than the expected values.

One reason for this deviation can be attributed to the dark counts of the APDs. Dark counts are uncorrelated with other counts, so their effect can be determined from the correlation of detector signals D_i , given by $D_i = I_i + d_i$ where I_i and d_i are the fluorescence signals and the dark counts from detector i . By subtracting the effect of dark counts from the data, the resulting $g^{(2)}$ values for the fluorescence signals are obtained. This yields $g_{\parallel}^{(2)}(\tau = 0)$ as 0.24 ± 0.11 and $g_{\perp}^{(2)}(\tau = 0)$ as 0.55 ± 0.12 , which aligns more closely with the expected values. Consequently, this results in a two-photon interference visibility of $V = 0.56 \pm 0.22$.

For the parallel polarizations, the imperfect coalescence can be caused by the difference in the spectral profiles of the cooling fluorescence. Under the illumination of an off-resonant cooling light, the power spectrum of the scattered fluorescence will have a three-peak structure (refer to Chapter 3.2 for more discussions on Mollow triplet) centered at the cooling beam frequency (ω_{cool}) and roughly one detuning Δ away from the cooling beam frequency ($\omega_{\text{cool}} \pm \Delta$). Suppose that the trap depth for the two dipole traps is slightly different due to asymmetry in the focusing optics, the detunings will be different for the two single atoms, leading to a mismatch in the power spectrum. To mitigate this issue, we can choose a weak near-resonant light that can help reduce the contributions in the sidebands.

6.3 Summary

In short, we have successfully demonstrated the trapping of single atoms in a pair of holographic dipole traps. Using a computer-controlled spatial light modulator, we show the capability to control the distance between the pair of single atoms. Two challenges arising at short atomic spacings ($d = 1.5 \mu\text{m}$) are investigated, including the trap hopping induced by atomic thermal motion and the formation of an additional dipole trap along the optical axis. Finally, we perform a two-photon interference measurement on the cooling fluorescence scattered by a pair of single atoms. We confirm the observation of photon coalescence while projecting the photon polarizations from orthogonal to parallel. Particularly, the second order correlation function at zero delay $g^{(2)}(0)$ varies from 0.55 ± 0.12 to 0.24 ± 0.11 after subtracting off the uncorrelated coincidences due to dark counts. This finding indicates that the single photons scattered by the two single atoms are very much indistinguishable.

CHAPTER 6. ARRAY OF TWO SINGLE ATOMS

We expect further improvements in the spectral mode matching for light scattered by the two single atoms can further increase the two-photon interference visibility. This will be crucial for the future exploration of various two-atom entanglement schemes based on the detection of single photons, effectively enhancing the entanglement visibility.

Chapter 7

Conclusion and Outlook

A single neutral atom held in an optical dipole trap at the focus of a high numerical aperture (NA) aspheric lens is a highly robust and clean quantum platform to investigate atom-light interactions at the single photon level. First, the high NA aspheric lens collects atomic fluorescence efficiently into a single mode fiber, enabling both the detection of atom trapping and the application of rapid fluorescence-based techniques for lossless state detection. Furthermore, the high NA aspheric lens also focuses down incident light to a mode size close to the dipole transition cross-section, effectively enhancing the probability of a single photon interacting coherently with the atom. These appealing properties enable us to examine the emission characteristics of a strongly driven two-level system. We also present systematic improvements in our free-space single-atom system, addressing aspects such as qubit coherence, motional control, and the scalability of qubit numbers.

In Chapter 3, using a cycling optical transition of ^{87}Rb atom, we investigate the simplest form of optical nonlinearity: saturation of a two-level transition, which results in the emergence of sidebands in the spectral profile of atomic fluorescence. By imposing a detuning to the driving field, we further demonstrate that pairs of single photons originating from opposite fluorescence sidebands are temporally correlated. This discovery may open up novel approaches for the generation of non-classical light fields for the interface between atomic qubits and photonic quantum communication channels.

Overcoming qubit coherence limitations has been a persistent challenge in various quantum computing platforms. Using the magnetically sensitive Zeeman sublevels in the ^{87}Rb ground state manifold as our qubit states, the dephasing time for

CHAPTER 7. CONCLUSION AND OUTLOOK

a superposition state was initially measured to be around $40\ \mu\text{s}$. Through the implementation of a suitable decoupling protocol, we successfully extended this coherence time to about $7\ \text{ms}$ (Chapter 4). This prolonged coherence time is particularly crucial for applications involving atom-photon entanglement, as it preserves the relative phase of the entangled state while the photon is transmitted over long distances.

Going from a two-level system to a three-level Λ system, the introduction of an additional energy level and dipole transition grants us greater flexibility in manipulating a single atom. We study the excitation spectrum of a single atom interacting with a pair of pump and probe beams, illustrating the phenomenon of Fano interference (Chapter 5). By exploiting the aforementioned scattering mechanism to selectively drive the red motional sideband transition, we successfully achieve cooling of atomic temperature to less than $6\ \mu\text{K}$. This work holds significance for the longstanding goal [130, 131] of attaining complete control over the position and motion of an optically trapped neutral atom.

Next, we proceed to implement the deterministic trapping of single atoms in a holographic dipole trap array in Chapter 6. We show the precise control of the trap array spacing by varying the wavefront modulation period. To conclude, a two-photon interference measurement is performed on the cooling fluorescence emitted by a pair of single atoms, demonstrating the phenomenon of photon coalescence.

With the techniques outlined in this thesis, this marks an ideal starting point to delve into the realization of practical quantum information protocols. Ongoing efforts in our research group are directed toward creating entanglement between a single atom and a single photon. The scheme is as follows [25]: a single atom is excited to an excited state with a short optical pulse, followed by a spontaneous decay to multiple ground states. This process leads to the formation of an entangled state between the polarization of the emitted photon and the ground state sublevels of the atom. Currently, the generation of the excitation pulse with a temporal width smaller than $20\ \text{ns}$ (full-width half maximum) is ready for implementation. Measurements are underway to confirm that the excitation probability is close to unity (π -pulse).

Compared to the recent work reported in [27] showcasing a single photon detection efficiency of 7.5×10^{-3} with an APD after an excitation attempt, we anticipate a

CHAPTER 7. CONCLUSION AND OUTLOOK

fourfold improvement for our collection system, reaching a detection efficiency of 2.8×10^{-2} . In the same work, the entanglement distribution was limited to 20 km caused by decoherence of the atomic state. This issue can be overcome with a decoupling protocol, making transmission loss the sole constraint for long-distance entanglement distribution.

Regarding the cooling of atomic motion using the Fano interference effect, the pair of probe and coupling beams implemented in our system currently address only two dimensions of the atomic motion. We foresee a further reduction in atomic temperature by employing additional probe beams with wave vectors encompassing all three directions, potentially reaching the motional ground state.

Another challenge is that the conventional release-recapture technique is only weakly dependent on the longitudinal motion. Exploring new methods such as motional sideband resolving Raman spectroscopy [130, 131] or microwave sideband spectroscopy in a state-dependent trap potential [169] would be necessary to deduce the mean vibrational number associated with the atomic motion along the optical axis.

Combined with the holographic dipole trap array system, the ground state cooling technique opens up new pathways to investigate non-classical properties related to the atomic motional state. This includes phenomena like the two-atom Hong-Ou-Mandel interference due to the indistinguishability of single atoms in all except for their positional degree of freedom [191]. An improved motional control also motivates the implementation of motional sideband-based two-qubit protocols, such as the Mølmer-Sørensen gate [197], on an array of neutral atoms for quantum computing applications.

Another idea is to align more closely with the recent trends in neutral atom quantum computing platforms. By employing the holographic dipole trap array with a higher FORT beam power, we can scale up the number of qubits in our system, approaching the capabilities of state-of-the-art systems with hundreds of qubits [198]. The major challenge lies in effectively implementing the rearrangement of atoms and fast qubit operations, particularly two-qubit gates based on Rydberg excitation while preserving qubit coherence [199].

Bibliography

- [1] J. P. Dowling and G. J. Milburn, “Quantum technology: the second quantum revolution”, *Philos. Trans. R. Soc. A* **361**, 1655–1674 (2003).
- [2] R. P. Feynman, “Simulating physics with computers”, *Int. J. Theor. Phys* **21**, 467–488 (1982).
- [3] P. W. Shor, “Polynomial-time algorithms for prime factorization and discrete logarithms on a quantum computer”, *SIAM J. Comput.* **26**, 1484–1509 (1997).
- [4] E. Martin-Lopez, A. Laing, T. Lawson, R. Alvarez, X.-Q. Zhou, and J. L. O’Brien, “Experimental realization of shor’s quantum factoring algorithm using qubit recycling”, *Nat. Photonics* **6**, 773–776 (2012).
- [5] C. Gidney and M. Ekerå, “How to factor 2048 bit rsa integers in 8 hours using 20 million noisy qubits”, *Quantum* **5**, 433 (2021).
- [6] D. S. Wild, D. Sels, H. Pichler, C. Zanoci, and M. D. Lukin, “Quantum sampling algorithms for near-term devices”, *Phys. Rev. Lett.* **127**, 100504 (2021).
- [7] H.-S. Zhong, H. Wang, Y.-H. Deng, M.-C. Chen, L.-C. Peng, Y.-H. Luo, J. Qin, D. Wu, X. Ding, Y. Hu, P. Hu, X.-Y. Yang, W.-J. Zhang, H. Li, Y. Li, X. Jiang, L. Gan, G. Yang, L. You, Z. Wang, L. Li, N.-L. Liu, C.-Y. Lu, and J.-W. Pan, “Quantum computational advantage using photons”, *Science* **370**, 1460–1463 (2020).
- [8] H. S. Zhong, Y. H. Deng, J. Qin, H. Wang, M. C. Chen, L. C. Peng, Y. H. Luo, D. Wu, S. Q. Gong, H. Su, Y. Hu, P. Hu, X. Y. Yang, W. J. Zhang, H. Li, Y. Li, X. Jiang, L. Gan, G. Yang, L. You, Z. Wang, L. Li, N. L. Liu, J. J. Renema, C. Y. Lu, and J. W. Pan, “Phase-programmable gaussian boson sampling using stimulated squeezed light”, *Phys. Rev. Lett.* **127**, 180502 (2021).

BIBLIOGRAPHY

- [9] L. S. Madsen, F. Laudenbach, M. F. Askarani, F. Rortais, T. Vincent, J. F. Bulmer, F. M. Miatto, L. Neuhaus, L. G. Helt, M. J. Collins, A. E. Lita, T. Gerrits, S. W. Nam, V. D. Vaidya, M. Menotti, I. Dhand, Z. Vernon, N. Quesada, and J. Lavoie, “Quantum computational advantage with a programmable photonic processor”, *Nature* **606**, 75–81 (2022).
- [10] F. Arute, K. Arya, R. Babbush, D. Bacon, J. C. Bardin, R. Barends, R. Biswas, S. Boixo, F. G. Brandao, D. A. Buell, B. Burkett, Y. Chen, Z. Chen, B. Chiaro, R. Collins, W. Courtney, A. Dunsworth, E. Farhi, B. Foxen, A. Fowler, C. Gidney, M. Giustina, R. Graff, K. Guerin, S. Habegger, M. P. Harrigan, M. J. Hartmann, A. Ho, M. Hoffmann, T. Huang, T. S. Humble, S. V. Isakov, E. Jeffrey, Z. Jiang, D. Kafri, K. Kechedzhi, J. Kelly, P. V. Klimov, S. Knysh, A. Korotkov, F. Kostritsa, D. Landhuis, M. Lindmark, E. Lucero, D. Lyakh, S. Mandrà, J. R. McClean, M. McEwen, A. Megrant, X. Mi, K. Michielsen, M. Mohseni, J. Mutus, O. Naaman, M. Neeley, C. Neill, M. Y. Niu, E. Ostby, A. Petukhov, J. C. Platt, C. Quintana, E. G. Rieffel, P. Roushan, N. C. Rubin, D. Sank, K. J. Satzinger, V. Smelyanskiy, K. J. Sung, M. D. Trevithick, A. Vainsencher, B. Villalonga, T. White, Z. J. Yao, P. Yeh, A. Zalcman, H. Neven, and J. M. Martinis, “Quantum supremacy using a programmable superconducting processor”, *Nature* **574**, 505–510 (2019).
- [11] Y. Wu, W.-S. Bao, S. Cao, F. Chen, M.-C. Chen, X. Chen, T.-H. Chung, H. Deng, Y. Du, D. Fan, M. Gong, C. Guo, C. Guo, S. Guo, L. Han, L. Hong, H.-L. Huang, Y.-H. Huo, L. Li, N. Li, S. Li, Y. Li, F. Liang, C. Lin, J. Lin, H. Qian, D. Qiao, H. Rong, H. Su, L. Sun, L. Wang, S. Wang, D. Wu, Y. Xu, K. Yan, W. Yang, Y. Yang, Y. Ye, J. Yin, C. Ying, J. Yu, C. Zha, C. Zhang, H. Zhang, K. Zhang, Y. Zhang, H. Zhao, Y. Zhao, L. Zhou, Q. Zhu, C.-Y. Lu, C.-Z. Peng, X. Zhu, and J.-W. Pan, “Strong quantum computational advantage using a superconducting quantum processor”, *Phys. Rev. Lett.* **127**, 180501 (2021).
- [12] H. J. Kimble, “The quantum internet”, *Nature* **453**, 1023–1030 (2008).
- [13] D. M. Zajac, A. J. Sigillito, M. Russ, F. Borjans, J. M. Taylor, G. Burkard, and J. R. Petta, “Resonantly driven cnot gate for electron spins”, *Science* **359**, 439–442 (2018).

BIBLIOGRAPHY

- [14] W. Huang, C. Yang, K. Chan, T. Tanttu, B. Hensen, R. Leon, M. Fogarty, J. Hwang, F. Hudson, K. M. Itoh, A. Morello, A. Laucht, and A. S. Dzurak, “Fidelity benchmarks for two-qubit gates in silicon”, *Nature* **569**, 532–536 (2019).
- [15] L. Childress, M. Gurudev Dutt, J. Taylor, A. Zibrov, F. Jelezko, J. Wrachtrup, P. Hemmer, and M. Lukin, “Coherent dynamics of coupled electron and nuclear spin qubits in diamond”, *Science* **314**, 281–285 (2006).
- [16] X. Rong, J. Geng, F. Shi, Y. Liu, K. Xu, W. Ma, F. Kong, Z. Jiang, Y. Wu, and J. Du, “Experimental fault-tolerant universal quantum gates with solid-state spins under ambient conditions”, *Nat. Commun.* **6**, 8748 (2015).
- [17] V. Schäfer, C. Ballance, K. Thirumalai, L. Stephenson, T. Ballance, A. Steane, and D. Lucas, “Fast quantum logic gates with trapped-ion qubits”, *Nature* **555**, 75–78 (2018).
- [18] J. M. Pino, J. M. Dreiling, C. Figgatt, J. P. Gaebler, S. A. Moses, M. Allman, C. Baldwin, M. Foss-Feig, D. Hayes, K. Mayer, C. Ryan-Anderson, and B. Neyenhuis, “Demonstration of the trapped-ion quantum ccd computer architecture”, *Nature* **592**, 209–213 (2021).
- [19] H. Levine, A. Keesling, A. Omran, H. Bernien, S. Schwartz, A. S. Zibrov, M. Endres, M. Greiner, V. Vuletić, and M. D. Lukin, “High-fidelity control and entanglement of rydberg-atom qubits”, *Phys. Rev. Lett.* **121**, 123603 (2018).
- [20] P. Jurcevic, A. Javadi-Abhari, L. S. Bishop, I. Lauer, D. F. Bogorin, M. Brink, L. Capelluto, O. Günlük, T. Itoko, N. Kanazawa, A. Kandala, G. A. Keefe, K. Krsulich, W. Landers, E. P. Lewandowski, D. T. McClure, G. Nannicini, A. Narasgond, H. M. Nayfeh, E. Pritchett, M. B. Rothwell, S. Srinivasan, N. Sundaresan, C. Wang, K. X. Wei, C. J. Wood, J.-B. Yau, E. J. Zhang, O. E. Dial, J. M. Chow, and J. M. Gambetta, “Demonstration of quantum volume 64 on a superconducting quantum computing system”, *Quantum Sci. Technol.* **6**, 025020 (2021).

BIBLIOGRAPHY

- [21] X. Wang, X. Jiao, B. Wang, Y. Liu, X. P. Xie, M. Y. Zheng, Q. Zhang, and J. W. Pan, “Quantum frequency conversion and single-photon detection with lithium niobate nanophotonic chips”, *npj Quantum Inf.* **9**, 38 (2023).
- [22] R. Ikuta, T. Kobayashi, T. Kawakami, S. Miki, M. Yabuno, T. Yamashita, H. Terai, M. Koashi, T. Mukai, T. Yamamoto, and N. Imoto, “Polarization insensitive frequency conversion for an atom-photon entanglement distribution via a telecom network”, *Nat. Commun.* **9**, 1997 (2018).
- [23] L. Li, Y. O. Dudin, and A. Kuzmich, “Entanglement between light and an optical atomic excitation”, *Nature* **498**, 466–469 (2013).
- [24] C. Laplane, P. Jobez, J. Etesse, N. Gisin, and M. Afzelius, “Multimode and long-lived quantum correlations between photons and spins in a crystal”, *Phys. Rev. Lett.* **118**, 210501 (2017).
- [25] J. Volz, M. Weber, D. Schlenk, W. Rosenfeld, J. Vrana, K. Saucke, C. Kurtsiefer, and H. Weinfurter, “Observation of entanglement of a single photon with a trapped atom”, *Phys. Rev. Lett.* **96**, 030404 (2006).
- [26] T. Wilk, S. C. Webster, A. Kuhn, and G. Rempe, “Single-atom single-photon quantum interface”, *Science* **317**, 488–490 (2007).
- [27] T. van Leent, M. Bock, R. Garthoff, K. Redeker, W. Zhang, T. Bauer, W. Rosenfeld, C. Becher, and H. Weinfurter, “Long-distance distribution of atom-photon entanglement at telecom wavelength”, *Phys. Rev. Lett.* **124**, 010510 (2020).
- [28] B. B. Blinov, D. L. Moehring, L. M. Duan, and C. Monroe, “Observation of entanglement between a single trapped atom and a single photon”, *Nature* **428**, 153–157 (2004).
- [29] E. Togan, Y. Chu, A. S. Trifonov, L. Jiang, J. Maze, L. Childress, M. G. Dutt, A. S. Sørensen, P. R. Hemmer, A. S. Zibrov, and M. D. Lukin, “Quantum entanglement between an optical photon and a solid-state spin qubit”, *Nature* **466**, 730–734 (2010).
- [30] W. Gao, P. Fallahi, E. Togan, J. Miguel-Sánchez, and A. Imamoglu, “Observation of entanglement between a quantum dot spin and a single photon”, *Nature* **491**, 426–430 (2012).

BIBLIOGRAPHY

- [31] B. M. Terhal, “Quantum error correction for quantum memories”, *Rev. Mod. Phys.* **87**, 307–346 (2015).
- [32] G. M. Palma, K.-A. Suominen, and A. Ekert, “Quantum computers and dissipation”, *Proc. R. Soc. Lond. A* **452**, 567–584 (1996).
- [33] L.-M. Duan and G.-C. Guo, “Preserving coherence in quantum computation by pairing quantum bits”, *Phys. Rev. Lett.* **79**, 1953–1956 (1997).
- [34] L. Viola and S. Lloyd, “Dynamical suppression of decoherence in two-state quantum systems”, *Phys. Rev. A* **58**, 2733–2744 (1998).
- [35] L. Viola, E. Knill, and S. Lloyd, *Phys. Rev. Lett.* **82**, 2417–2421 (1999).
- [36] N. Kalb, A. A. Reiserer, P. C. Humphreys, J. J. W. Bakermans, S. J. Kamberling, N. H. Nickerson, S. C. Benjamin, D. J. Twitchen, M. Markham, and R. Hanson, “Entanglement distillation between solid-state quantum network nodes”, *Science* **356**, 928–932 (2017).
- [37] M. Arcari, I. Söllner, A. Javadi, S. Lindskov Hansen, S. Mahmoodian, J. Liu, H. Thyrestrup, E. H. Lee, J. D. Song, S. Stobbe, and P. Lodahl, “Near-unity coupling efficiency of a quantum emitter to a photonic crystal waveguide”, *Phys. Rev. Lett.* **113**, 093603 (2014).
- [38] M. K. Bhaskar, D. D. Sukachev, A. Sipahigil, R. E. Evans, M. J. Burek, C. T. Nguyen, L. J. Rogers, P. Siyushev, M. H. Metsch, H. Park, F. Jelezko, M. Lončar, and M. D. Lukin, “Quantum nonlinear optics with a germanium-vacancy color center in a nanoscale diamond waveguide”, *Phys. Rev. Lett.* **118**, 223603 (2017).
- [39] H. Thyrestrup, G. Kiršanskė, H. Le Jeannic, T. Pregnolato, L. Zhai, L. Raahauge, L. Midolo, N. Rotenberg, A. Javadi, R. Schott, A. D. Wieck, A. Ludwig, M. C. Löbl, I. Söllner, R. J. Warburton, and P. Lodahl, “Quantum optics with near-lifetime-limited quantum-dot transitions in a nanophotonic waveguide”, *Nano Lett.* **18**, 1801–1806 (2018).
- [40] S. Kato and T. Aoki, “Strong coupling between a trapped single atom and an all-fiber cavity”, *Phys. Rev. Lett.* **115**, 093603 (2015).

BIBLIOGRAPHY

- [41] K. P. Nayak, J. Wang, and J. Keloth, “Real-time observation of single atoms trapped and interfaced to a nanofiber cavity”, *Phys. Rev. Lett.* **123**, 213602 (2019).
- [42] T. Aoki, B. Dayan, E. Wilcut, W. P. Bowen, A. S. Parkins, T. J. Kippenberg, K. J. Vahala, and H. J. Kimble, “Observation of strong coupling between one atom and a monolithic microresonator”, *Nature* **443**, 671–674 (2006).
- [43] E. Will, L. Masters, A. Rauschenbeutel, M. Scheucher, and J. Volz, “Coupling a single trapped atom to a whispering-gallery-mode microresonator”, *Phys. Rev. Lett.* **126**, 233602 (2021).
- [44] I. M. Bassett, “Limit to concentration by focusing”, *J. Mod. Opt.* **33**, 279–286 (1986).
- [45] S. A. Aljunid, M. K. Tey, B. Chng, T. Liew, G. Maslennikov, V. Scarani, and C. Kurtsiefer, “Phase shift of a weak coherent beam induced by a single atom”, *Phys. Rev. Lett.* **103**, 153601 (2009).
- [46] B. Dayan, A. S. Parkins, T. Aoki, E. P. Ostby, K. J. Vahala, and H. J. Kimble, “A photon turnstile dynamically regulated by one atom”, *Science* **319**, 1062–1065 (2008).
- [47] D. E. Chang, V. Vuletić, and M. D. Lukin, “Quantum nonlinear optics - photon by photon”, *Nat. Photonics* **8**, 685–694 (2014).
- [48] Y.-S. Chin, M. Steiner, and C. Kurtsiefer, “Nonlinear photon-atom coupling with 4pi microscopy”, *Nat. Commun.* **8**, 1200 (2017).
- [49] H. Zheng, D. J. Gauthier, and H. U. Baranger, “Waveguide qed: many-body bound-state effects in coherent and fock-state scattering from a two-level system”, *Phys. Rev. A* **82**, 063816 (2010).
- [50] A. N. Vamivakas, M. Atatüre, J. Dreiser, S. Yilmaz, A. Badolato, A. K. Swan, B. B. Goldberg, A. Imamoğlu, and M. Ünlü, “Strong extinction of a far-field laser beam by a single quantum dot”, *Nano Lett.* **7**, 2892–2896 (2007).
- [51] I. Gerhardt, G. Wrigge, P. Bushev, G. Zumofen, M. Agio, R. Pfab, and V. Sandoghdar, “Strong extinction of a laser beam by a single molecule”, *Phys. Rev. Lett.* **98**, 033601 (2007).

BIBLIOGRAPHY

- [52] G. Wrigge, I. Gerhardt, J. Hwang, G. Zumofen, and V. Sandoghdar, “Efficient coupling of photons to a single molecule and the observation of its resonance fluorescence”, *Nat. Phys.* **4**, 60–66 (2008).
- [53] M. Pototschnig, Y. Chassagneux, J. Hwang, G. Zumofen, A. Renn, and V. Sandoghdar, “Controlling the phase of a light beam with a single molecule”, *Phys. Rev. Lett.* **107**, 063001 (2011).
- [54] N. Piro, F. Rohde, C. Schuck, M. Almendros, J. Huwer, J. Ghosh, A. Haase, M. Hennrich, F. Dubin, and J. Eschner, “Heralded single-photon absorption by a single atom”, *Nat. Phys.* **7**, 17–20 (2011).
- [55] A. Maser, B. Gmeiner, T. Utikal, S. Götzinger, and V. Sandoghdar, “Few-photon coherent nonlinear optics with a single molecule”, *Nat. Photonics* **10**, 450–453 (2016).
- [56] T. H. Tran, P. Siyushev, J. Wrachtrup, and I. Gerhardt, “Extinction of light and coherent scattering by a single nitrogen-vacancy center in diamond”, *Phys. Rev. A* **95**, 053831 (2017).
- [57] M. K. Tey, Z. Chen, S. A. Aljunid, B. Chng, F. Huber, G. Maslennikov, and C. Kurtsiefer, “Strong interaction between light and a single trapped atom without the need for a cavity”, *Nat. Phys.* **4**, 924–927 (2008).
- [58] E. W. Streed, B. G. Norton, A. Jechow, T. J. Weinhold, and D. Kielpinski, “Imaging of trapped ions with a microfabricated optic for quantum information processing”, *Phys. Rev. Lett.* **106**, 010502 (2011).
- [59] T.-W. Hsu, W. Zhu, T. Thiele, M. O. Brown, S. B. Papp, A. Agrawal, and C. A. Regal, “Single-atom trapping in a metasurface-lens optical tweezer”, *PRX Quantum* **3**, 030316 (2022).
- [60] M. Fischer, M. Bader, R. Maiwald, A. Golla, M. Sondermann, and G. Leuchs, “Efficient saturation of an ion in free space”, *Appl. Phys. B* **117**, 797–801 (2014).
- [61] L. Alber, M. Fischer, M. Bader, K. Mantel, M. Sondermann, and G. Leuchs, “Focusing characteristics of a 4π parabolic mirror light-matter interface”, *J. Eur. Opt. Soc.-Rapid Publ.* **13**, 14 (2017).

BIBLIOGRAPHY

- [62] M. Fischer, B. Srivathsan, L. Alber, M. Weber, M. Sondermann, and G. Leuchs, “Shifting the phase of a coherent beam with a $^{174}\text{Yb}^+$ ion: influence of the scattering cross section”, *Appl. Phys. B* **123**, 48 (2017).
- [63] D. J. Wineland, W. M. Itano, and J. Bergquist, “Absorption spectroscopy at the limit: detection of a single atom”, *Opt. Lett.* **12**, 389–391 (1987).
- [64] M. Steiner, Y.-S. Chin, and C. Kurtsiefer, “Transmission spectroscopy of a single atom in the presence of tensor light shifts”, *New J. Phys.* **21**, 023012 (2019).
- [65] H. P. Yuen and M. Ozawa, “Ultimate information carrying limit of quantum systems”, *Phys. Rev. Lett.* **70**, 363–366 (1993).
- [66] C. M. Caves and P. D. Drummond, “Quantum limits on bosonic communication rates”, *Rev. Mod. Phys.* **66**, 481–537 (1994).
- [67] C. M. Caves, K. S. Thorne, R. W. P. Drever, V. D. Sandberg, and M. Zimmermann, “On the measurement of a weak classical force coupled to a quantum-mechanical oscillator. i. issues of principle”, *Rev. Mod. Phys.* **52**, 341–392 (1980).
- [68] C. M. Caves, “Quantum-mechanical noise in an interferometer”, *Phys. Rev. D* **23**, 1693–1708 (1981).
- [69] B. R. Mollow, “Power spectrum of light scattered by two-level systems”, *Phys. Rev.* **188**, 1969–1975 (1969).
- [70] C. A. Schrama, G. Nienhuis, H. A. Dijkerman, C. Steijsiger, and H. G. M. Heideman, “Intensity correlations between the components of the resonance fluorescence triplet”, *Phys. Rev. A* **45**, 8045–8055 (1992).
- [71] Y.-S. Chin, M. Steiner, and C. Kurtsiefer, “Quantifying the role of thermal motion in free-space light-atom interaction”, *Phys. Rev. A* **95**, 043809 (2017).
- [72] G. Morigi, J. Eschner, and C. H. Keitel, “Ground state laser cooling using electromagnetically induced transparency”, *Phys. Rev. Lett.* **85**, 4458–4461 (2000).
- [73] S. J. Masson and A. Asenjo-Garcia, “Universality of dicke superradiance in arrays of quantum emitters”, *Nat. Commun.* **13**, 2285 (2022).

BIBLIOGRAPHY

- [74] Y.-S. Chin, “Light-atom coupling with 4pi microscopy”, Available online at <https://scholarbank.nus.edu.sg/handle/10635/146931>, PhD dissertation (May 2018).
- [75] T. Arpornthip, C. A. Sackett, and K. J. Hughes, “Vacuum-pressure measurement using a magneto-optical trap”, *Phys. Rev. A* **85**, 033420 (2012).
- [76] E. L. Raab, M. Prentiss, A. Cable, S. Chu, and D. E. Pritchard, “Trapping of neutral sodium atoms with radiation pressure”, *Phys. Rev. Lett.* **59**, 2631–2634 (1987).
- [77] R. Grimm, M. Weidemüller, and Y. B. Ovchinnikov, “Optical dipole traps for neutral atoms”, *Adv. At. Mol. Opt. Phys.* **42**, 95–170 (2000).
- [78] K. C. Neuman and S. M. Block, “Optical trapping”, *Rev. Sci. Instrum.* **75**, 2787–2809 (2004).
- [79] J. J. Sakurai and E. D. Commins, “Modern quantum mechanics (3rd ed.)” (Cambridge University Press, 1995) Chap. 5.7.
- [80] S. M. Tan, “A computational toolbox for quantum and atomic optics”, *J. Opt. B: Quantum Semiclass. Opt.* **1**, 424–432 (1999).
- [81] J. Johansson, P. Nation, and F. Nori, “Qutip: an open-source python framework for the dynamics of open quantum systems”, *Comput. Phys. Commun.* **183**, 1760–1772 (2012).
- [82] B. L. Ng, Available online at <https://scholarbank.nus.edu.sg/handle/10635/246242>, PhD dissertation (Aug. 2023).
- [83] I. H. Deutsch and P. S. Jessen, “Quantum control and measurement of atomic spins in polarization spectroscopy”, *Opt. Commun.* **283**, 681–694 (2010).
- [84] N. Schlosser, G. Reymond, and P. Grangier, “Collisional blockade in microscopic optical dipole traps”, *Phys. Rev. Lett.* **89**, 023005 (2002).
- [85] Y. H. Fung and M. F. Andersen, “Efficient collisional blockade loading of a single atom into a tight microtrap”, *New J. Phys.* **17**, 073011 (2015).
- [86] C. Maurer, A. Jesacher, S. Fürhapter, S. Bernet, and M. Ritsch-Marte, “Tailoring of arbitrary optical vector beams”, *New J. Phys.* **9**, 78 (2007).

BIBLIOGRAPHY

- [87] A. N. Utama, C. H. Chow, C. H. Nguyen, and C. Kurtsiefer, “Coupling light to higher order transverse modes of a near-concentric optical cavity”, *Opt. Express* **29**, 8130–8141 (2021).
- [88] F. M. Arscott, “Periodic differential equations: an introduction to mathieu, lamé, and allied functions”, (Elsevier, 1964) Chap. 1.
- [89] L. Landau and E. Lifshitz, “Mechanics: volume 1”, (Elsevier, 1982) Chap. 5.
- [90] J. Dalibard and C. Cohen-Tannoudji, “Laser cooling below the doppler limit by polarization gradients: simple theoretical models”, *J. Opt. Soc. Am. B* **6**, 2023–2045 (1989).
- [91] Y.-S. Chin, M. Steiner, and C. Kurtsiefer, “Polarization gradient cooling of single atoms in optical dipole traps”, *Phys. Rev. A* **96**, 033406 (2017).
- [92] C. Tuchendler, A. M. Lance, A. Browaeys, Y. R. P. Sortais, and P. Grangier, “Energy distribution and cooling of a single atom in an optical tweezer”, *Phys. Rev. A* **78**, 033425 (2008).
- [93] J. Bochmann, M. Mücke, C. Guhl, S. Ritter, G. Rempe, and D. L. Moehring, “Lossless state detection of single neutral atoms”, *Phys. Rev. Lett.* **104**, 203601 (2010).
- [94] W. Happer, “Optical pumping”, *Rev. Mod. Phys.* **44**, 169–249 (1972).
- [95] J. D. Wong-Campos, K. G. Johnson, B. Neyenhuis, J. Mizrahi, and C. Monroe, “High-resolution adaptive imaging of a single atom”, *Nat. Photonics* **10**, 606–610 (2016).
- [96] L. Ortiz-Gutiérrez, R. C. Teixeira, A. Eloy, D. F. da Silva, R. Kaiser, R. Bachelard, and M. Fouché, “Mollow triplet in cold atoms”, *New J. Phys.* **21**, 093019 (2019).
- [97] Y. Stalgies, I. Siemers, B. Appasamy, T. Altevogt, and P. E. Toschek, “The spectrum of single-atom resonance fluorescence”, *EPL* **35**, 259–264 (1996).
- [98] J. D. Sterk, L. Luo, T. A. Manning, P. Maunz, and C. Monroe, “Photon collection from a trapped ion-cavity system”, *Phys. Rev. A* **85**, 062308 (2012).
- [99] A. N. Vamivakas, Y. Zhao, C.-Y. Lu, and M. Atatüre, “Spin-resolved quantum-dot resonance fluorescence”, *Nat. Phys.* **5**, 198–202 (2009).

BIBLIOGRAPHY

- [100] E. B. Flagg, A. Muller, J. W. Robertson, S. Founta, D. G. Deppe, M. Xiao, W. Ma, G. J. Salamo, and C. K. Shih, “Resonantly driven coherent oscillations in a solid-state quantum emitter”, *Nat. Phys.* **5**, 203–207 (2009).
- [101] S. Ates, S. M. Ulrich, S. Reitzenstein, A. Löffler, A. Forchel, and P. Michler, “Post-selected indistinguishable photons from the resonance fluorescence of a single quantum dot in a microcavity”, *Phys. Rev. Lett.* **103**, 167402 (2009).
- [102] A. Ulhaq, S. Weiler, S. M. Ulrich, R. Roßbach, M. Jetter, and P. Michler, “Cascaded single-photon emission from the mollow triplet sidebands of a quantum dot”, *Nat. Photonics* **6**, 238–242 (2012).
- [103] K. Konthasinghe, J. Walker, M. Peiris, C. K. Shih, Y. Yu, M. F. Li, J. F. He, L. J. Wang, H. Q. Ni, Z. C. Niu, and A. Muller, “Coherent versus incoherent light scattering from a quantum dot”, *Phys. Rev. B* **85**, 235315 (2012).
- [104] O. Astafiev, A. M. Zagoskin, A. A. Abdumalikov, Y. A. Pashkin, T. Yamamoto, K. Inomata, Y. Nakamura, and J. S. Tsai, “Resonance fluorescence of a single artificial atom”, *Science* **327**, 840–843 (2010).
- [105] A. F. van Loo, A. Fedorov, K. Lalumière, B. C. Sanders, A. Blais, and A. Wallraff, “Photon-mediated interactions between distant artificial atoms”, *Science* **342**, 1494–1496 (2013).
- [106] D. M. Toyli, A. W. Eddins, S. Boutin, S. Puri, D. Hover, V. Bolkhovsky, W. D. Oliver, A. Blais, and I. Siddiqi, “Resonance fluorescence from an artificial atom in squeezed vacuum”, *Phys. Rev. X* **6**, 031004 (2016).
- [107] C. Cohen-Tannoudji, J. Dupont-Roc, and G. Grynberg, “Atom-photon interactions: basic processes and applications”, (John Wiley & Sons, Inc., 1998) Chap. 6.
- [108] L. Mandel and E. Wolf, “Optical coherence and quantum optics”, (Cambridge University Press, 1995) Chap. 15.
- [109] C. Cohen-Tannoudji and S. Reynaud, “Dressed-atom description of resonance fluorescence and absorption spectra of a multi-level atom in an intense laser beam”, *J. Phys. B: Atom. Mol. Phys.* **10**, 345–363 (1977).
- [110] D. J. Griffiths, “Introduction to electrodynamics”, (Cambridge University Press, 2017) Chap. 11.

BIBLIOGRAPHY

- [111] R. Loudon, “The quantum theory of light”, (Oxford University Press, 2000) Chap. 8.
- [112] A. Aspect, G. Roger, S. Reynaud, J. Dalibard, and C. Cohen-Tannoudji, “Time correlations between the two sidebands of the resonance fluorescence triplet”, *Phys. Rev. Lett.* **45**, 617–620 (1980).
- [113] G. Nienhuis, “Spectral correlations in resonance fluorescence”, *Phys. Rev. A* **47**, 510–518 (1993).
- [114] L. Childress, J. M. Taylor, A. S. Sørensen, and M. D. Lukin, “Fault-tolerant quantum communication based on solid-state photon emitters”, *Phys. Rev. Lett.* **96**, 070504 (2006).
- [115] S. J. van Enk, J. I. Cirac, and P. Zoller, “Photonic channels for quantum communication”, *Science* **279**, 205–208 (1998).
- [116] L.-M. Duan, M. D. Lukin, J. I. Cirac, and P. Zoller, “Long-distance quantum communication with atomic ensembles and linear optics”, *Nature* **414**, 413–418 (2001).
- [117] N. H. Lindner and T. Rudolph, “Proposal for pulsed on-demand sources of photonic cluster state strings”, *Phys. Rev. Lett.* **103**, 113602 (2009).
- [118] J. P. Lee, B. Villa, A. J. Bennett, R. M. Stevenson, D. J. P. Ellis, I. Farrer, D. A. Ritchie, and A. J. Shields, “A quantum dot as a source of time-bin entangled multi-photon states”, *Quantum Sci. Technol.* **4**, 025011 (2019).
- [119] D. Bouwmeester, J.-W. Pan, M. Daniell, H. Weinfurter, and A. Zeilinger, “Observation of three-photon greenberger-horne-zeilinger entanglement”, *Phys. Rev. Lett.* **82**, 1345–1349 (1999).
- [120] P. A. Böhi, “Coherent manipulation of ultracold atoms with microwave near-fields”, Available online at <https://www.mpg.mpg.de/5720882/MPQ333.pdf>, PhD dissertation (Oct. 2010).
- [121] S. Kuhr, W. Alt, D. Schrader, I. Dotsenko, Y. Miroshnychenko, A. Rauschenbeutel, and D. Meschede, “Analysis of dephasing mechanisms in a standing-wave dipole trap”, *Phys. Rev. A* **72**, 023406 (2005).

BIBLIOGRAPHY

- [122] J. H. Bodey, R. Stockill, E. V. Denning, D. A. Gangloff, G. Éthier-Majcher, D. M. Jackson, E. Clarke, M. Hugues, C. L. Gall, and M. Atatüre, “Optical spin locking of a solid-state qubit”, *npj Quantum Inf.* **5**, 95 (2019).
- [123] T. C. Farrar and E. D. Becker, “Pulse and fourier transform nmr: introduction to theory and methods”, (Academic Press, Inc., 1971) Chap. 1.
- [124] W. Rosenfeld, J. Volz, M. Weber, and H. Weinfurter, “Coherence of a qubit stored in zeeman levels of a single optically trapped atom”, *Phys. Rev. A* **84**, 022343 (2011).
- [125] C. Cohen-Tannoudji and J. Dupont-Roc, “Experimental study of zeeman light shifts in weak magnetic fields”, *Phys. Rev. A* **5**, 968–984 (1972).
- [126] M. Takamoto, F.-L. Hong, R. Higashi, and H. Katori, “An optical lattice clock”, *Nature* **435**, 321–324 (2005).
- [127] M. H. Schleier-Smith, I. D. Leroux, and V. Vuletić, “States of an ensemble of two-level atoms with reduced quantum uncertainty”, *Phys. Rev. Lett.* **104**, 073604 (2010).
- [128] R. Chicireanu, K. D. Nelson, S. Olmschenk, N. Lundblad, A. Derevianko, and J. V. Porto, “Differential light-shift cancellation in a magnetic-field-insensitive transition of ^{87}Rb ”, *Phys. Rev. Lett.* **106**, 063002 (2011).
- [129] B. Richards and E. Wolf, “Electromagnetic diffraction in optical systems, ii. structure of the image field in an aplanatic system”, *Proc. R. Soc. Lond. A* **253**, 358–379 (1959).
- [130] A. M. Kaufman, B. J. Lester, and C. A. Regal, “Cooling a single atom in an optical tweezer to its quantum ground state”, *Phys. Rev. X* **2**, 041014 (2012).
- [131] J. D. Thompson, T. G. Tiecke, A. S. Zibrov, V. Vuletić, and M. D. Lukin, “Coherence and raman sideband cooling of a single atom in an optical tweezer”, *Phys. Rev. Lett.* **110**, 133001 (2013).
- [132] M. K. Tey, G. Maslennikov, T. C. H. Liew, S. A. Aljunid, F. Huber, B. Chng, Z. Chen, V. Scarani, and C. Kurtsiefer, “Interfacing light and single atoms with a lens”, *New J. Phys.* **11**, 043011 (2009).

BIBLIOGRAPHY

- [133] U. Hohenester, “Nano and quantum optics: an introduction to basic principles and theory”, (Springer Nature Switzerland AG, 2020) Chap. 3.
- [134] S. J. van Enk and H. J. Kimble, “Strongly focused light beams interacting with single atoms in free space”, *Phys. Rev. A* **63**, 023809 (2001).
- [135] E. L. Hahn, “Spin echoes”, *Phys. Rev.* **80**, 580–594 (1950).
- [136] L. M. K. Vandersypen and I. L. Chuang, “Nmr techniques for quantum control and computation”, *Rev. Mod. Phys.* **76**, 1037–1069 (2005).
- [137] D. D. Yavuz, P. B. Kulatunga, E. Urban, T. A. Johnson, N. Proite, T. Henage, T. G. Walker, and M. Saffman, “Fast ground state manipulation of neutral atoms in microscopic optical traps”, *Phys. Rev. Lett.* **96**, 063001 (2006).
- [138] M. P. A. Jones, J. Beugnon, A. Gaëtan, J. Zhang, G. Messin, A. Browaeys, and P. Grangier, “Fast quantum state control of a single trapped neutral atom”, *Phys. Rev. A* **75**, 040301 (2007).
- [139] Y. Ovchinnikov and G. Marra, “Accurate rubidium atomic fountain frequency standard”, *Metrologia* **48**, 87–100 (2011).
- [140] J. Yang, X. He, R. Guo, P. Xu, K. Wang, C. Sheng, M. Liu, J. Wang, A. Derevianko, and M. Zhan, “Coherence preservation of a single neutral atom qubit transferred between magic-intensity optical traps”, *Phys. Rev. Lett.* **117**, 123201 (2016).
- [141] M. Körber, O. Morin, S. Langenfeld, A. Neuzner, S. Ritter, and G. Rempe, “Decoherence-protected memory for a single-photon qubit”, *Nat. Photonics* **12**, 18–21 (2018).
- [142] M. J. Biercuk, A. C. Doherty, and H. Uys, “Dynamical decoupling sequence construction as a filter-design problem”, *J. Phys. B: At. Mol. Opt. Phys.* **44**, 154002 (2011).
- [143] J. Bylander, S. Gustavsson, F. Yan, F. Yoshihara, K. Harrabi, G. Fitch, D. G. Cory, Y. Nakamura, J.-S. Tsai, and W. D. Oliver, “Noise spectroscopy through dynamical decoupling with a superconducting flux qubit”, *Nat. Phys.* **7**, 565–570 (2011).

BIBLIOGRAPHY

- [144] G. Afek, J. Coslovsky, A. Mil, and N. Davidson, “Revival of raman coherence of trapped atoms”, *Phys. Rev. A* **96**, 043831 (2017).
- [145] S. B. Markussen, J. Appel, C. Østfeldt, J.-B. S. Béguin, E. S. Polzik, and J. H. Müller, “Measurement and simulation of atomic motion in nanoscale optical trapping potentials”, *Appl. Phys. B* **126**, 73 (2020).
- [146] C. A. Ryan, J. S. Hodges, and D. G. Cory, “Robust decoupling techniques to extend quantum coherence in diamond”, *Phys. Rev. Lett.* **105**, 200402 (2010).
- [147] D. D. Sukachev, A. Sipahigil, C. T. Nguyen, M. K. Bhaskar, R. E. Evans, F. Jelezko, and M. D. Lukin, “Silicon-vacancy spin qubit in diamond: a quantum memory exceeding 10 ms with single-shot state readout”, *Phys. Rev. Lett.* **119**, 223602 (2017).
- [148] D. J. Szwer, S. C. Webster, A. M. Steane, and D. M. Lucas, “Keeping a single qubit alive by experimental dynamic decoupling”, *J. Phys. B: At. Mol. Opt. Phys.* **44**, 025501 (2011).
- [149] M. A. Ali Ahmed, G. A. Álvarez, and D. Suter, “Robustness of dynamical decoupling sequences”, *Phys. Rev. A* **87**, 042309 (2013).
- [150] M. Hirose, C. D. Aiello, and P. Cappellaro, “Continuous dynamical decoupling magnetometry”, *Phys. Rev. A* **86**, 062320 (2012).
- [151] I. Baumgart, J.-M. Cai, A. Retzker, M. B. Plenio, and C. Wunderlich, “Ultra-sensitive magnetometer using a single atom”, *Phys. Rev. Lett.* **116**, 240801 (2016).
- [152] S. Hernández-Gómez, F. Poggiali, P. Cappellaro, and N. Fabbri, “Noise spectroscopy of a quantum-classical environment with a diamond qubit”, *Phys. Rev. B* **98**, 214307 (2018).
- [153] G. S. Uhrig, “Keeping a quantum bit alive by optimized π -pulse sequences”, *Phys. Rev. Lett.* **98**, 100504 (2007).
- [154] C. P. Slichter, “Principles of magnetic resonance”, (Springer-Verlag, 1978) Chap. 8.

BIBLIOGRAPHY

- [155] S. Meiboom and D. Gill, “Modified spin-echo method for measuring nuclear relaxation times”, *Rev. Sci. Instrum.* **29**, 688–691 (1958).
- [156] T. Gullion, D. B. Baker, and M. S. Conradi, “New, compensated carr-purcell sequences”, *J. Magn. Reson.* **89**, 479–484 (1990).
- [157] M. Razavi, M. Piani, and N. Lütkenhaus, “Quantum repeaters with imperfect memories: cost and scalability”, *Phys. Rev. A* **80**, 032301 (2009).
- [158] C. F. Roos, D. Leibfried, A. Mundt, F. Schmidt-Kaler, J. Eschner, and R. Blatt, “Experimental demonstration of ground state laser cooling with electromagnetically induced transparency”, *Phys. Rev. Lett.* **85**, 5547–5550 (2000).
- [159] R. Lechner, C. Maier, C. Hempel, P. Jurcevic, B. P. Lanyon, T. Monz, M. Brownnutt, R. Blatt, and C. F. Roos, “Electromagnetically-induced-transparency ground-state cooling of long ion strings”, *Phys. Rev. A* **93**, 053401 (2016).
- [160] L. Feng, W. L. Tan, A. De, A. Menon, A. Chu, G. Pagano, and C. Monroe, “Efficient ground-state cooling of large trapped-ion chains with an electromagnetically-induced-transparency tripod scheme”, *Phys. Rev. Lett.* **125**, 053001 (2020).
- [161] T. Kampschulte, W. Alt, S. Manz, M. Martinez-Dorantes, R. Reimann, S. Yoon, D. Meschede, M. Bienert, and G. Morigi, “Electromagnetically-induced-transparency control of single-atom motion in an optical cavity”, *Phys. Rev. A* **89**, 033404 (2014).
- [162] B. Lounis and C. Cohen-Tannoudji, “Coherent population trapping and fano profiles”, *J. Phys. II* **2**, 579–592 (1992).
- [163] G. Janik, W. Nagourney, and H. Dehmelt, “Doppler-free optical spectroscopy on the ba^+ mono-ion oscillator”, *J. Opt. Soc. Am. B* **2**, 1251 (1985).
- [164] Y. Stalgies, I. Siemers, B. Appasamy, and P. E. Toschek, “Light shift and fano resonances in a single cold ion”, *J. Opt. Soc. Am. B* **15**, 2505 (1998).
- [165] U. Fano, “Effects of configuration interaction on intensities and phase shifts”, *Phys. Rev.* **124**, 1866–1878 (1961).

BIBLIOGRAPHY

- [166] G. Morigi, “Cooling atomic motion with quantum interference”, *Phys. Rev. A* **67**, 033402 (2003).
- [167] E. Haller, J. Hudson, A. Kelly, D. A. Cotta, B. Peaudecerf, G. D. Bruce, and S. Kuhr, “Single-atom imaging of fermions in a quantum-gas microscope”, *Nat. Phys.* **11**, 738–742 (2015).
- [168] G. Morigi, J. Eschner, and C. H. Keitel, “Ground state laser cooling using electromagnetically induced transparency”, *Phys. Rev. Lett.* **85**, 4458–4461 (2000).
- [169] L. Förster, M. Karski, J.-M. Choi, A. Steffen, W. Alt, D. Meschede, A. Widera, E. Montano, J. H. Lee, W. Rakreungdet, and P. S. Jessen, “Microwave control of atomic motion in optical lattices”, *Phys. Rev. Lett.* **103**, 233001 (2009).
- [170] R. H. Dicke, “Coherence in spontaneous radiation processes”, *Phys. Rev.* **93**, 99–110 (1954).
- [171] J. P. Clemens, L. Horvath, B. C. Sanders, and H. J. Carmichael, “Collective spontaneous emission from a line of atoms”, *Phys. Rev. A* **68**, 023809 (2003).
- [172] M. O. Scully, E. S. Fry, C. H. R. Ooi, and K. Wódkiewicz, “Directed spontaneous emission from an extended ensemble of N atoms: timing is everything”, *Phys. Rev. Lett.* **96**, 010501 (2006).
- [173] S. J. Masson, I. Ferrier-Barbut, L. A. Orozco, A. Browaeys, and A. Asenjo-Garcia, “Many-body signatures of collective decay in atomic chains”, *Phys. Rev. Lett.* **125**, 263601 (2020).
- [174] S. J. Roof, K. J. Kemp, M. D. Havey, and I. M. Sokolov, “Observation of single-photon superradiance and the cooperative lamb shift in an extended sample of cold atoms”, *Phys. Rev. Lett.* **117**, 073003 (2016).
- [175] G. Ferioli, A. Glicenstein, F. Robicheaux, R. T. Sutherland, A. Browaeys, and I. Ferrier-Barbut, “Laser-driven superradiant ensembles of two-level atoms near dicke regime”, *Phys. Rev. Lett.* **127**, 243602 (2021).
- [176] D. C. Gold, P. Huft, C. Young, A. Safari, T. G. Walker, M. Saffman, and D. D. Yavuz, “Spatial coherence of light in collective spontaneous emission”, *PRX Quantum* **3**, 010338 (2022).

BIBLIOGRAPHY

- [177] S. Wolf, S. Richter, J. von Zanthier, and F. Schmidt-Kaler, “Light of two atoms in free space: bunching or antibunching?”, *Phys. Rev. Lett.* **124**, 063603 (2020).
- [178] M. Scheibner, T. Schmidt, L. Worschech, A. Forchel, G. Bacher, T. Passow, and D. Hommel, “Superradiance of quantum dots”, *Nat. Phys.* **3**, 106–110 (2007).
- [179] F. Nogrette, H. Labuhn, S. Ravets, D. Barredo, L. Béguin, A. Vernier, T. Lahaye, and A. Browaeys, “Single-atom trapping in holographic 2d arrays of microtraps with arbitrary geometries”, *Phys. Rev. X* **4**, 021034 (2014).
- [180] H. Kim, W. Lee, H.-g. Lee, H. Jo, Y. Song, and J. Ahn, “In situ single-atom array synthesis using dynamic holographic optical tweezers”, *Nat. Commun.* **7**, 13317 (2016).
- [181] M. Born and E. Wolf, “Principles of optics: electromagnetic theory of propagation, interference and diffraction of light (7th ed.)” (Cambridge University Press, 1999) Chap. 6.
- [182] T. Harte, G. D. Bruce, J. Keeling, and D. Cassetari, “Conjugate gradient minimisation approach to generating holographic traps for ultracold atoms”, *Opt. Express* **22**, 26548 (2014).
- [183] M. Pasienski and B. DeMarco, “A high-accuracy algorithm for designing arbitrary holographic atom traps”, *Opt. Express* **16**, 2176 (2008).
- [184] A. L. Gaunt and Z. Hadzibabic, “Robust digital holography for ultracold atom trapping”, *Sci. Rep.* **2**, 721 (2012).
- [185] R. W. Gerchberg and W. O. Saxton, “A practical algorithm for the determination of phase from image and diffraction plane pictures”, *Optik* **35**, 237–246 (1972).
- [186] R. D. Leonardo, F. Ianni, and G. Ruocco, “Computer generation of optimal holograms for optical trap arrays”, *Opt. Express* **15**, 1913 (2007).
- [187] N. Holland, D. Stuart, O. Barter, and A. Kuhn, “Benchmarking modern algorithms to holographically create optical tweezers for laser-cooled atoms”, *J. Mod. Opt.* **65**, 2133–2141 (2018).

BIBLIOGRAPHY

- [188] B. E. A. Saleh and M. C. Teich, “Fundamentals of photonics”, (John Wiley & Sons, Inc., 1991) Chap. 4.4.
- [189] H. J. Müller-Kirsten, “Introduction to quantum mechanics: schrödinger equation and path integral”, (World Scientific, 2012) Chap. 18.
- [190] D. J. Griffiths, “Introduction to quantum mechanics”, (Cambridge University Press, 2017) Chap. 9.
- [191] A. M. Kaufman, B. J. Lester, C. M. Reynolds, M. L. Wall, M. Foss-Feig, K. R. A. Hazzard, A. M. Rey, and C. A. Regal, “Two-particle quantum interference in tunnel-coupled optical tweezers”, *Science* **345**, 306–309 (2014).
- [192] P. Zhou, Y. Li, S. Liu, and Y. Su, “Dynamic compensatory gerchberg–saxton algorithm for multiple-plane reconstruction in holographic displays”, *Opt. Express* **27**, 8958 (2019).
- [193] C. Cabrillo, J. I. Cirac, P. García-Fernández, and P. Zoller, “Creation of entangled states of distant atoms by interference”, *Phys. Rev. A* **59**, 1025–1033 (1999).
- [194] L. Slodička, G. Hétet, N. Röck, P. Schindler, M. Hennrich, and R. Blatt, “Atom-atom entanglement by single-photon detection”, *Phys. Rev. Lett.* **110**, 083603 (2013).
- [195] C. K. Hong, Z. Y. Ou, and L. Mandel, “Measurement of subpicosecond time intervals between two photons by interference”, *Phys. Rev. Lett.* **59**, 2044–2046 (1987).
- [196] R. B. Patel, A. J. Bennett, K. Cooper, P. Atkinson, C. A. Nicoll, D. A. Ritchie, and A. J. Shields, “Postselective two-photon interference from a continuous nonclassical stream of photons emitted by a quantum dot”, *Phys. Rev. Lett.* **100**, 207405 (2008).
- [197] A. Sørensen and K. Mølmer, “Quantum computation with ions in thermal motion”, *Phys. Rev. Lett.* **82**, 1971–1974 (1999).
- [198] S. Ebadi, T. T. Wang, H. Levine, A. Keesling, G. Semeghini, A. Omran, D. Bluvstein, R. Samajdar, H. Pichler, W. W. Ho, S. Choi, S. Sachdev, M. Greiner, V. Vuletić, and M. D. Lukin, “Quantum phases of matter on a 256-atom programmable quantum simulator”, *Nature* **595**, 227–232 (2021).

BIBLIOGRAPHY

- [199] K. Wintersperger, F. Dommert, T. Ehmer, A. Hoursanov, J. Klepsch, W. Maurer, G. Reuber, T. Strohm, M. Yin, and S. Lubner, “Neutral atom quantum computing hardware: performance and end-user perspective”, *EPJ Quantum Technol.* **10**, 32 (2023).

Publications during Ph.D. Study

- [1] C. H. Chow, B. L. Ng, and C. Kurtsiefer, “Coherence of a dynamically decoupled single neutral atom”, *J. Opt. Soc. Am. B* **38**, 621–629 (2021).
- [2] A. N. Utama, C. H. Chow, C. H. Nguyen, and C. Kurtsiefer, “Coupling light to higher order transverse modes of a near-concentric optical cavity”, *Opt. Express* **29**, 8130–8141 (2021).
- [3] L. Shen, C. H. Chow, J. Y. X. Peh, X. J. Yeo, P. K. Tan, and C. Kurtsiefer, “Distributing polarization-entangled photon pairs with high rate over long distances through standard telecommunication fiber”, *Phys. Rev. Appl.* **18**, 044075 (2022).
- [4] B. L. Ng, C. H. Chow, and C. Kurtsiefer, “Observation of the mollow triplet from an optically confined single atom”, *Phys. Rev. A* **106**, 063719 (2022).
- [5] C. H. Chow, B. L. Ng, V. Prakash, and C. Kurtsiefer, “Fano resonance in excitation spectroscopy and cooling of an optically trapped single atom”, arXiv:2312.06438, accepted in *Phys. Rev. Research* (2024).